

Syracuse University

SURFACE at Syracuse University

Dissertations - ALL

SURFACE at Syracuse University

Winter 12-22-2021

Adsorption of organic Iodides on Reduced Silver Functionalized Silica Aerogel

Siqi Tang

Syracuse University

Follow this and additional works at: <https://surface.syr.edu/etd>



Part of the [Chemical Engineering Commons](#)

Recommended Citation

Tang, Siqi, "Adsorption of organic Iodides on Reduced Silver Functionalized Silica Aerogel" (2021).

Dissertations - ALL. 1539.

<https://surface.syr.edu/etd/1539>

This Dissertation is brought to you for free and open access by the SURFACE at Syracuse University at SURFACE at Syracuse University. It has been accepted for inclusion in Dissertations - ALL by an authorized administrator of SURFACE at Syracuse University. For more information, please contact surface@syr.edu.

Abstract

In the nuclear waste reprocessing, radioactive iodine is released in both organic and inorganic forms into off-gas streams. Due to its properties of long half-life and accumulation in human bodies, the radioactive iodine is required to be removed by the Environmental Protection Agency (EPA) and Nuclear Regulatory Commission (NRC). In this presented work, the removal of organic iodides is studied particularly.

Unlike that of inorganic iodine, the organic iodides were not well studied because of the low concentrations and the corresponding technical difficulties. Most of the studies on the organic iodides are semi-quantified, focusing on the performances of the adsorption columns of certain combinations of conditions and the quantified single-layer adsorptions were rarely reported. To provide the information and results supporting the adsorption columns design, single layer continuous-flow organic iodides adsorptions using silver-containing adsorbents were performed. The solid adsorption method was developed in replacement of the liquid scrubbing strategy for its low operational cost and simplicity of design. The most commonly used adsorbents include reduced silver exchanged mordenite (Ag^0Z) and silver nitrate impregnated alumina (AgA), and they have been applied in multiple waste reprocessing plants around the world. In the 2010s, a novel silver-containing material, reduced silver functionalized silica aerogel ($\text{Ag}^0\text{-Aerogel}$), was developed at the Pacific Northwest National Laboratory (PNNL), and has been considered as an outstanding material for its high silver content and adsorption rate.

The efficiencies of the three materials were evaluated and the $\text{Ag}^0\text{-Aerogel}$ was identified to be

the optimum adsorbent among Ag⁰-Aerogel, Ag⁰Z and AgA. Therefore, the CH₃I adsorptions on Ag⁰-Aerogel were performed at various concentrations and temperatures. The data were analyzed using multiple models and the parameters were determined. The results indicated that the CH₃I adsorption on Ag⁰-Aerogel is a surface reaction at the specified conditions and the adsorption rate increases with the adsorption temperature.

Additionally, adsorptions of other iodoalkanes (C₃H₇I, C₆H₁₃I, C₈H₁₇I and C₁₂H₂₅I) were performed and the corresponding dependencies on temperatures, concentrations and the length of carbon chain were determined. The C₆H₁₃I and C₁₂H₂₅I adsorptions are likely to be zero-order adsorptions and the temperature dependencies may vary at different conditions. Moreover, the adsorption rates of C₃H₇I and C₈H₁₇I are higher than expected, accordingly, further studies are suggested.

Using the parameters determined, the column adsorption modeling of organic iodides was conducted and the modeling results were comparable to the literature works. The model was also applied to predict the breakthrough of the column, and the outcomes indicate that a column of at least 15-20 cm is required to remove the organic iodides of up to approximately 100 ppbv. Based on the results of organic iodides adsorptions and the modeling works, the potential research objectives were recommended and the properties of the next generation materials and adsorption systems were also suggested.

**Adsorption of Organic Iodides on Reduced Silver Functionalized
Silica Aerogel**

by

Siqi Tang

B.S., Syracuse University, 2018

Dissertation

Submitted in partial fulfillment of the requirements for the degree of

Doctor of Philosophy in Chemical Engineering

Syracuse University

December 2021

Copyright © Siqi Tang 2021

All Rights Reserved

Acknowledgement

I would like to address my most sincere thanks to my advisor, Professor Lawrence L. Tavlarides, for your guidance through my graduate education experience. I would have not been able to finish all my studies without your encouragement and support. Your knowledge, patience and kindness helped me and will continue in my career.

I am deeply grateful to my parents, Wenzhao Tang and Zhiyun Liu. Thank you for supporting me with your endless love and providing me so many diversities in my life. I became a better person under your care.

I would like to thank Professor Philip Rice, Professor Costas Tsouris and Professor Sotira Yiacomou for joining the weekly group meetings and the monthly conference calls. Your enlightened advice helps me to summarize and proceed my studies.

My best friends, Chen Wang, Yuxi Dai and Zining Liu, I deeply thank you for your companions in these years. I wish we can meet again soon.

Special thanks are addressed to my current and former lab colleagues, Dr. Yue Nan, Dr. Jiuxu Liu and Mr. Seungrag Choi. I first enter the lab in 2017 as an undergrad, you taught me step-by-step how to operate the instruments, how to do the physical analyses and how to analyze the data.

I would like to thank Professor Jesse Bond for inspiring me with the algorithm used in calculating the modeling error. Additionally, I'm grateful to the students in Prof. Bond's lab, Robson Schuarca for teaching me how to perform the nitrogen adsorption test and lending me the liquid nitrogen for it; and Bowei Liu, Xin Gao and Xinlei Huang for discussing the reaction

kinetics, mechanism and fluid mechanics with me.

Thanks to Professor Viktor Cybulskis, for the valuable advice in selecting the physical analyses to be performed and to the students in his Lab, Jingzhi Liu, Wenlin He and Hansheng Li for assisting me in performing the XRD analyses.

I thank all the defense committee members including Professor Jesse Bond, Professor Joseph Chaiken, Professor Ruth Chen, Professor Viktor Cybulskis, Professor Ian Hosein, Professor Radhakrishna Sureshkumar and Professor Lawrence Tavlarides for your time joining my defense.

Thanks to my friends He Feng and Ruixian Han for providing their valuable advice about SEM, XPS and NMR analyses.

I'm also grateful to my friends in the New York Chinese Opera Society (NYCOS) and 'LiYuanShiJia-MaFu' including Bin Ma, Jialu Guo, Tianyu Shao, Shu Li, Xin Zhao, Zhixiang Ma, and others, for their friendship and valuable advice in job searching.

Finally, I would like to thank the Department of Biomedical and Chemical Engineering, Syracuse University, for providing the excellent research environments and the U.S. Department of Energy, Office of Nuclear Energy, for the financial assistance on the project of this work (Project ID: 18-15596).

Table of Contents

Acknowledgement	V
List of Figures	XI
List of Tables.....	XVI
Notation.....	XVIII
Abbreviations.....	XXIII
Chapter 1. Introduction	1
Chapter 2. Literature Review	11
2.1 Calculating the ^{129}I Concentration Limit	11
2.2 Adsorptions on Ag^0Z	12
2.3 Adsorptions on Ag^0 -Aerogel.....	13
2.4 Alternative Materials.....	14
2.5 Adsorbent Aging	15
Chapter 3. Experimental	18
3.1 Experimental Setup.....	18
3.2 Organic Iodides.....	23
3.3 Materials	29
3.4 Experimental Conditions	31
3.5 Analytical Techniques.....	33
3.5.1 SEM-EDX.....	33

3.5.2 XPS	33
3.5.3 Nitrogen Titration.....	34
3.6 Modeling.....	34
3.6.1 Shrinking Core Model.....	34
3.6.2 Volume Reaction Model.....	37
3.6.3 Linear Driving Force Model	38
3.6.4 Pore Diffusion Model	41
3.6.5 Fick's Law.....	43
3.7 Difficulties in Organic Iodides Adsorption on Ag ⁰ -Aerogel.....	43
Chapter 4. Material Comparison: Ag ⁰ -Aerogel, Ag ⁰ Z and AgA.....	46
4.1 AgA Manufacturing	46
4.2 Adsorption Kinetics and Modeling Results	47
4.3 Physical Analyses Results.....	49
4.4 Aging Resistance.....	51
4.5 Conclusions.....	51
Chapter 5. CH ₃ I Adsorption on Ag ⁰ -Aerogel: Concentration Dependence	53
5.1 Introduction.....	53
5.2 Adsorption Kinetics	54
5.3 Considering the Aging Effect.....	56
5.4 Model Fitting Results and Model Comparison.....	62

5.5 N th Order Shrinking Core Model	68
5.6 N th Order SCM Examination and Application	70
5.7 Rate-Controlling Step	73
5.8 Potential Reaction Mechanism	78
5.9 Conclusions.....	82
Chapter 6. CH ₃ I Adsorption on Ag ⁰ -Aerogel: Temperature Dependence.....	85
6.1 Introduction.....	85
6.2 Procedure Description.....	86
6.3 Adsorption Kinetics	87
6.4 Water Equilibrium in Drying Process	90
6.5 Nitrogen Adsorption Analyses	93
6.6 Pore Distribution and Silver Site Availability.....	97
6.7 Arrhenius Relationship and Eyring Equation	98
6.8 XPS and SEM-EDX Analyses	102
6.9 Surface Composition.....	108
6.10 Explanation for the Additional Mass Uptake.....	113
6.11 Conclusions and Recommendations	114
Chapter 7. Adsorption of Other Iodoalkanes	116
7.1 Introduction.....	116
7.2 Adsorption Kinetics	116

7.3 Shrinking Core Model Fitting.....	119
7.3.1 Estimating the Gas Film Diffusivity and Pore Diffusivity	119
7.3.2 Model Fitting Results.....	120
7.4 Concentration Dependence	124
7.5 Temperature Dependence.....	126
7.6 Carbon Chain Length Dependence	127
7.7 Conclusions and Recommendations	130
Chapter 8. Column Adsorption Modeling.....	132
8.1 Shrinking Core Model Incorporated Column Adsorption Modeling.....	132
8.2 40 ppbv CH ₃ I Column Adsorption, Literature Comparison	133
8.3 Modeling Results, Column Breakthrough	136
8.4 Column Length and Breakthrough.....	138
8.5 Simulations of C ₁₂ H ₂₅ I Column Adsorption	139
8.6 Recommendations and Conclusions	142
Chapter 9. Recommendations for Future Studies and Industrial Applications.....	143
9.1 Sulfur in Ag ⁰ -Aerogel and the Relationship to Aging and Reaction Mechanism.....	143
9.2 Long-Chain Iodoalkanes and Products	144
9.3 Suggestions for Next-Generation Materials and Adsorption systems	145
References.....	147
Vita.....	171

List of Figures

Figure 1-1. A typical nuclear waste treatment system.	3
Figure 3-1. Schematic diagram of the continuous flow organic iodides adsorption system. 19	
Figure 3-2. Photographs of the continuous flow adsorption system. (a-1) Adsorption column, (a-2) Ag ⁰ -Aerogel on the tray, (a-3) Furnace, (b) Dynacalibrator, (c) Microbalance head, (d) Microbalance controller and temperature controller, (e) Mass flow controller.	20
Figure 3-3. The schematic diagram of the Dynacalibrator Model 450 (in flow mode).	21
Figure 3-4. Molecule structures of CH ₃ I, C ₃ H ₇ I, C ₆ H ₁₃ I, C ₈ H ₁₇ I and C ₁₂ H ₂₅ I.	24
Figure 3-5. The 104 ppbv CH ₃ I permeation tube.	25
Figure 3-6. Photographs of Ag ⁰ -Aerogel, Ag ⁰ Z and AgA.	29
Figure 3-7. I ₂ adsorption kinetics of Ag ⁰ -Aerogel, Ag ⁰ Z and AgA.	31
Figure 3-8. Comparison of the shrinking core, volume reaction and linear driving force models (Curves only represent trends).	40
Figure 4-1. Adsorption kinetics of 104 (a) and 1044 (b) ppbv CH ₃ I adsorptions on Ag ⁰ -Aerogel, Ag ⁰ Z and AgA at 150 °C (No significant mass uptake on AgA observed at 104 ppbv).	48
Figure 5-1. Uptake curves of 104, 245, 1044 and 9584 ppbv CH ₃ I adsorptions on Ag ⁰ -Aerogel for up to 288 hours.	55
Figure 5-2. Model fitting results using SCM, VRM, LDFM and PDMI of the 245 and 9584	

ppbv CH ₃ I adsorption on Ag ⁰ -Aerogel with fixed $q_e = 37$ wt% and the aging effect- incorporated, time-dependent $q_e(t)$	58
Figure 5-3. The adsorption kinetics and model fitting results of 104, 245, 1044 and 9584 ppbv CH ₃ I adsorption on Ag ⁰ -Aerogel.	64
Figure 5-4. Shrinking core process observed in CH ₃ I adsorption on Ag ⁰ -Aerogel, two cut halves of a partially reacted pellet.	67
Figure 5-5. Reaction order plot, $\ln(C_b)$ vs. $\ln(k_s C_b)$	69
Figure 5-6. 104 ppbv CH ₃ I on Ag ⁰ -Aerogel, SCM prediction using n th order SCM and 1 st order SCM with <i>average</i> k_s	71
Figure 5-7. 104, 245, 1044 and 9584 ppbv CH ₃ I adsorption behavior prediction using n th order SCM.	72
Figure 5-8. Resistance contributions of pore diffusion and reaction terms for CH ₃ I-Ag ⁰ - Aerogel adsorption at 104, 245, 1044 and 9584 ppbv.	74
Figure 5-9. Real-time contribution of reaction term and pore diffusion term in CH ₃ I-Ag ⁰ - Aerogel adsorption at 104 ppbv (percentage represents reaction contribution).	76
Figure 5-10. The proposed reaction pathway between CH ₃ I and Ag in Ag ⁰ -Aerogel.	78
Figure 6-1. The CH ₃ I adsorption curves of 104 ppbv (a) and 1044 ppbv (b) at 100, 150 and 200 °C.	89
Figure 6-2. The 3-D fitting results of the Fick's law.	91
Figure 6-3 The 3-D fitting results of the SCM.	92

Figure 6-4. The adsorption curve and the modeling results of the water adsorption process (Fick's Law and PDMI are overlapped).....	92
Figure 6-5. The surface area and pore volume of micropores, macropores and total pores measured using nitrogen titration method at different drying conditions.	95
Figure 6-6. The BJH (a) and DFT (b) pore distribution plots of 350 °C degassed sample and room condition equilibrium (RC.EQ).....	98
Figure 6-7. The Arrhenius plot of 104 and 1044 ppbv CH ₃ I adsorptions on Ag ⁰ -Aerogel at 100, 150 and 200 °C.....	99
Figure 6-8. An example of the Eyring equation, how $\Delta G/R$ changes the dependency of k to T (curves have been rescaled and repositioned to clarify the tendencies).	101
Figure 6-9. Regional scans of Ag (a), I (b) XPS spectra of 104 ppbv CH ₃ I adsorbed Ag ⁰ - Aerogel and Ag (c), I(d) of 1044 ppbv CH ₃ I adsorbed Ag ⁰ -Aerogel, with fresh, 350 °C degassed, CH ₃ I fully loaded at 150 °C and I ₂ fully loaded Ag ⁰ -Aerogel at 150 °C as references.	103
Figure 6-10. The SEM images including SED, BEC, Ag mapping and I mapping of various Ag ⁰ -Aerogels: (a) fresh, (b) 104 ppbv/150 °C CH ₃ I partially loaded, (c) 1044 ppbv/150 °C CH ₃ I partially loaded, (d) 9585 ppbv/150 °C CH ₃ I fully loaded and (e) 50 ppmv /150 °C I ₂ fully loaded.	107
Figure 6-11. The regional scans of Ag(a), I(b) and the curve fits of the 104 ppbv/ 200 °C CH ₃ I adsorbed Ag ⁰ -Aerogel.....	110

Figure 7-1. The adsorption kinetics at 100, 150 and 200 °C, (a) C₃H₇I-96 ppbv, (b) C₈H₁₇I-60 ppbv, (c) C₆H₁₃I-101 ppbv, (d) C₆H₁₃I-733 ppbv, (e) C₁₂H₂₅I-113 ppbv, (f) C₁₂H₂₅I-606 ppbv. (T1 and T2 represent different experimental trials)118

Figure 7-2. The C₈H₁₇I-60 ppbv-T1 adsorption kinetics and the fitting results of the three methods. 123

Figure 7-3. A general reaction pathway between iodoalkanes and Ag. 125

Figure 7-4. The Arrhenius plots of (a) C₆H₁₃I-733 ppbv adsorption, and (b) C₁₂H₂₅I-113 ppbv adsorption..... 126

Figure 7-5. The adsorption kinetics of CH₃I-104 ppbv, C₃H₇I-96 ppbv, C₆H₁₃I-101 ppbv, C₈H₁₇I-60 ppbv, and C₁₂H₂₅I-113 ppbv at 150 °C. (T1 and T2 represent different experimental trials) 128

Figure 8-1. Fitting results of the 40 ppbv CH₃I column adsorption on Ag⁰-Aerogel in 120 days. (a) CH₃I concentration in the column by time, (b) mass uptake of Ag⁰-Aerogel in the column by time, (c), the core shrinkage r_c/R_a by time, (d) outlet concentration and the decontamination factor (DF), (e) mass uptake at the middle of section 1 ($z = 0.1$ cm), (f) mass uptake at Day 120 by distance. 135

Figure 8-2. Estimation of the breakthrough for the 40 ppbv CH₃I column adsorption on Ag⁰-Aerogel. (a) CH₃I concentration in the column by time, (b) mass uptake of Ag⁰-Aerogel in the column by time, (c), the core shrinkage r_c/R_a by time, (d) outlet concentration and the decontamination factor (DF), (e) mass uptake at the middle of

section 1 ($z = 0.1$ cm), (f) mass uptake at Day 10000 by distance.	137
Figure 8-3. Estimating the effectiveness of 40 ppbv CH_3I removal using columns with different lengths (From the top to the bottom, the column lengths increase accordingly).	138
Figure 8-4. (a) $\text{C}_{12}\text{H}_{25}\text{I}$ concentration in the column by time (113 ppbv), (b) mass uptake of Ag^0 -Aerogel in the column (113 ppbv), (c) $\text{C}_{12}\text{H}_{25}\text{I}$ concentration in the column (606 ppbv), (d) mass uptake of Ag^0 -Aerogel in the column by time (606 ppbv), (e) $\text{C}_{12}\text{H}_{25}\text{I}$ outlet concentration and the decontamination factor (DF) of two adsorption columns, (f) the mass uptake at $Z=0.1$ cm of two adsorption columns. (Column lengths are 15 and 90 cm for 113 and 606 ppbv respectively).....	140
Figure 8-5. (a) The mass transfer zone of two columns at $t=0.1$ day, (b) the penetration of $\text{C}_{12}\text{H}_{25}\text{I}$ into two columns at the end of adsorptions.	141
Figure 9-1. The schematic diagram of the chemical structure of Ag^0 -Aerogel.	143

List of Tables

Table 3-1. Specifications of the permeation tubes, concentrations calculated for 500 sccm flow rate.	28
Table 3-2. Properties of Ag ⁰ -Aerogel, Ag ⁰ Z and AgA.	30
Table 4-1. Composition of AgA measured by XPS and SEM-EDX.	47
Table 4-2. The model fitting parameters and results for 104 and 1044 ppbv CH ₃ I adsorption on Ag ⁰ -Aerogel, Ag ⁰ Z and AgA.	49
Table 4-3. The Ag and I compositions of Ag ⁰ -Aerogel, Ag ⁰ Z and AgA measured by XPS and SEM-EDX.	50
Table 5-1. The parameters determined using SCM, VRM, LDFM and PDMI with fixed q_e and aging-incorporated q_e	59
Table 5-2. The parameters determined for 104, 245, 1044 and 9584 ppbv CH ₃ I adsorption on Ag ⁰ -Aerogel.	65
Table 5-3. Parameters and results of determining reaction order.	69
Table 6-1. Parameters and results of the SCM.	88
Table 6-2. The Ag and I concentrations measured by SEM-EDX and XPS (I compositions have been calibrated as additional mass).	112
Table 7-1. The estimated k_f 's and D_p 's for the organic iodides adsorptions at 100, 150 and 200 °C.	120
Table 7-2. The shrinking core model parameters determined for C ₃ H ₇ I, C ₆ H ₁₃ I, C ₈ H ₁₇ I and	

C₁₂H₂₅I adsorptions on Ag⁰-Aerogel at 100, 150 and 200°C. (T1 and T2 represent different experimental trials)..... 122

Table 7-3. The parameters and model fitting results of CH₃I-104 ppbv, C₃H₇I-96 ppbv, C₆H₁₃I-101 ppbv, C₈H₁₇I-60 ppbv, and C₁₂H₂₅I-113 ppbv at 150 °C. (T1 and T2 represent different experimental trials)..... 129

Notation

A	Specific surface area, cm^2/g
b	Stoichiometric coefficient of Ag in Ag-organic iodides reaction
B_{12}	Geometry coefficient in Eq. 3-16
C	General concentrations, units specified in the context
\bar{C}	Dimensionless concentration
C_{Ag}	Silver concentration, mol/cm^3
C_b	Bulk adsorbate concentration, mol/cm^3
C_s	Adsorbed phase concentration on the pore surface, mol/cm^2
D^*	Diffusivity of C_2H_6 through the reacted layer, cm^2/s
D_a	Macropore diffusivity, cm^2/s
D_a'	Effective macropore diffusivity, cm^2/s
D_{AB}	Binary diffusion coefficient, cm^2/s
D_i	Micropore diffusivity, cm^2/s
D_i'	Effective micropore diffusivity, cm^2/s
D_p	Pore diffusivity, cm^2/s
H	Henry's law constant of adsorption
h	Planck's constant
K_L	Langmuir surface adsorption equilibrium constant

k	General reaction rate, units specified in the context
k_b	Boltzmann's constant
k_f	Gas film mass transfer coefficient, cm/s
k_{LDF}	Linear driving force mass transfer coefficient, s ⁻¹
k_s	1 st order reaction rate constant, cm/s
k_s^*	N th order reaction rate constant, (cm/s)·(mol/cm ³) ¹⁻ⁿ
k_s^0	Pre-exponential factor, cm/s
k_v	Rate constant for volume reaction, cm ³ /mol·s
L	Thickness of the reacted layer
m	Number of micropores per unit volume of macropore
M_{AB}	Average molecular weight of species A and B
n	Reaction order
\bar{n}	Summation index
N	Number of datapoints
N_A	Avogadro number, mol ⁻¹
P	Pressure, bar
<i>pseudo</i> k_s	N th -order-compensated reaction rate constant, cm/s
q	Average sorbate concentration in adsorbent, mol/g
$q(r,t)$	Sorbate concentration at radius r at time t , mol/g

q_e	Saturation sorbate concentration in adsorbent, mol/g
R	Gas constant, unit specified in the context
R_a	Radius of the pellet, cm
\bar{R}_a	Radius of macropore, cm
\bar{R}_i	Radius of micropore, cm
Re	Reynolds number
r	General reaction rate, unit specified in the context
r_c	Radius of the unreacted core, cm
S	Pore surface area, cm ²
Sc	Schmidt number
Sh	Sherwood number
t	Time, sec
T	Temperature, °C or K
$t_{1/2}$	Isotope half-life, sec
t_{sat}	Saturation time, sec
u	Gas velocity, cm/s
V	Volume of the pellet, cm ³
W_1	Geometry coefficient in Eq. 3-16
W_2	Geometry coefficient in Eq. 3-16

z	Distance from the column inlet, cm
α	Parameter defined in Eq. 3-26
β	Parameter defined in Eq. 3-27
ΔE	Activation energy, kJ/mol
ΔG	Gibbs free energy of activation, kJ/mol
ε_a	Macropore porosity
ε_b	Bulk porosity of the adsorption column
ε_i	Micropore porosity
ε_p	Porosity of the pellet
ζ	Geometry coefficient in Eq. 3-16
θ	Dimensionless time
λ	Rate constant of decay, s ⁻¹
v	Atomic diffusion volume, cm ³
ρ_p	Pellet Density, g/cm ³
τ_1	Gas film diffusion term in the shrinking core model, sec
τ_2	Pore diffusion term in the shrinking core model, sec
τ_3	Reaction term in the shrinking core model, sec
τ_3^*	N th order reaction term in the shrinking core model, sec
Φ	The term defined in Eq. 5-34

ϕ

Thiele modulus

Abbreviations

AARD	Average absolute relative deviation, %
Ag ⁰	Elemental silver
Ag ⁰ -Aerogel	Reduced silver functionalized silica aerogel
Ag ⁰ Z	Reduced silver exchanged mordenite
AgA	Silver nitrate impregnated alumina
AgX	Silver exchanged faujasite
BE	Binding Energy, eV
BEC	Backscattered electron composition
BET	Brunauer-Emmett-Teller method
BJH	Barrett-Joyner-Halenda method
Bq	Becquerel, 1Bq = 1 atom decayed per second
CFR	US Code of Federal Regulations
DF	Decontamination factor
DFT	Density Function Theory
DOG	Dissolver off-gas
EPA	U.S. Environment Protection Agency
FR	Flow rate, sccm
g/tIHM	Gram per metric ton of initial heavy metal

GA	Graphene aerogel
GWd/tIHM	Gigawatt-days per metric ton of initial heavy metal
LDFM	Linear driving force model
MOF	Metal organic frameworks
MW	Molecular weight, g/mol
NAA	Neutron activation analysis
NRC	U.S. Nuclear Regulatory Commission
PDM	Pore diffusion model
PDMI	Micropore diffusion model
ppbv	Part per billion by volume
ppmv	Part per million by volume
PR	Permeation Rate, ng/min
PUREX	Plutonium uranium reduction extraction
SCM	Shrinking core model
SED	Secondary electron detector
SEM	Scanning electron microscopy
SEM-EDX	Scanning electron microscopy with energy dispersive x-ray analysis
VOG	Vessel off-gas
VRM	Volume reaction model

WOG	Waste system off-gas
XAS	X-ray absorption spectroscopy
XPS	X-ray photoelectron spectroscopy
XRD	X-ray diffraction

Chapter 1. Introduction

In the early 20th century, a new era was initiated when one of the most well-known equations $E = mc^2$ was proposed by Einstein. This theory relates the mass and energy and provides a solid foundation to the nuclear energy. During the nuclear fission of uranium-235 (^{235}U), a neutron hits the nucleus of ^{235}U and the nucleus splits into multiple smaller nuclei. In this process, the summation of mass decreases and energy is released.

The nuclear fission was firstly discovered in the late 1930s by Hahn and Strassmann; they observed the change of elements when bombarding the nuclei with neutrons.¹ Once the scientists noticed that energy is released in the nuclear fission, the nuclear energy started to be used as weapons. In the early 1940s, the Manhattan Project was initiated and it brought an end to World War II.^{2,3} Soon after the war, the first nuclear power plant EBR-1 was built in Idaho by Argonne National Laboratory.⁴ At first, the plant can only power four lightbulbs, and in the 21st century, the power increased dramatically to over 1 GW.⁵ In 2020, more than 4 trillion kilowatt-hours were generated in the United States by the 95 nuclear power reactors, which contribute approximately 20% of all electricity.^{6,7}

Nuclear power is considered as clean energy for its low emission rate of air pollutants.⁸⁻¹⁰

However, multiple radioactive isotopes, including krypton (^{85}Kr), strontium (^{90}Sr), xenon

Permission granted by John Wiley and Sons to use the text of published articles in this presented work.

Tang S, Choi S, Nan Y, Tavlarides LL. Adsorption of Methyl Iodide on Reduced Silver-Functionalized Silica Aerogel: Kinetics and Modeling. *AIChE Journal*. 2020:e17137.

(^{133}Xe), iodine (^{129}I and ^{131}I), Cesium (^{134}Cs and ^{137}Cs), and others, are produced in the uranium fission.¹¹⁻¹³ In this presented work, the adsorption of iodine will be evaluated.

When the life cycle of nuclear fuel is terminated, a treatment process is required for the recycling of uranium and proper storage of the nuclear waste. The schematic diagram of a typical waste treatment system is shown in Figure 1-1.¹³⁻¹⁵ The spent nuclear fuel rods are disassembled and dissolved using concentrated nitric acid (HNO_3); a portion of tritium (T) is removed with gas phase radioactive isotopes (T, C, I, Kr, Xe, etc.) being released into the dissolver off-gas (DOG).¹⁴ After the dissolution, the solution undergoes the plutonium uranium reduction extraction (PUREX) process. The uranium and plutonium are extracted and concentrated using organic solvents, which can be further reused as nuclear fuel with additional treatments. In the aqueous separation process, some radioactive isotopes react with the organic solvents and the products such as radioactive organic iodides are released to the vessel off-gas (VOG). After the extraction, uranium and plutonium are recycled and the remaining components are solidified and stored; in this process, some remaining gas phase isotopes are released to the waste system off-gas (WOG).

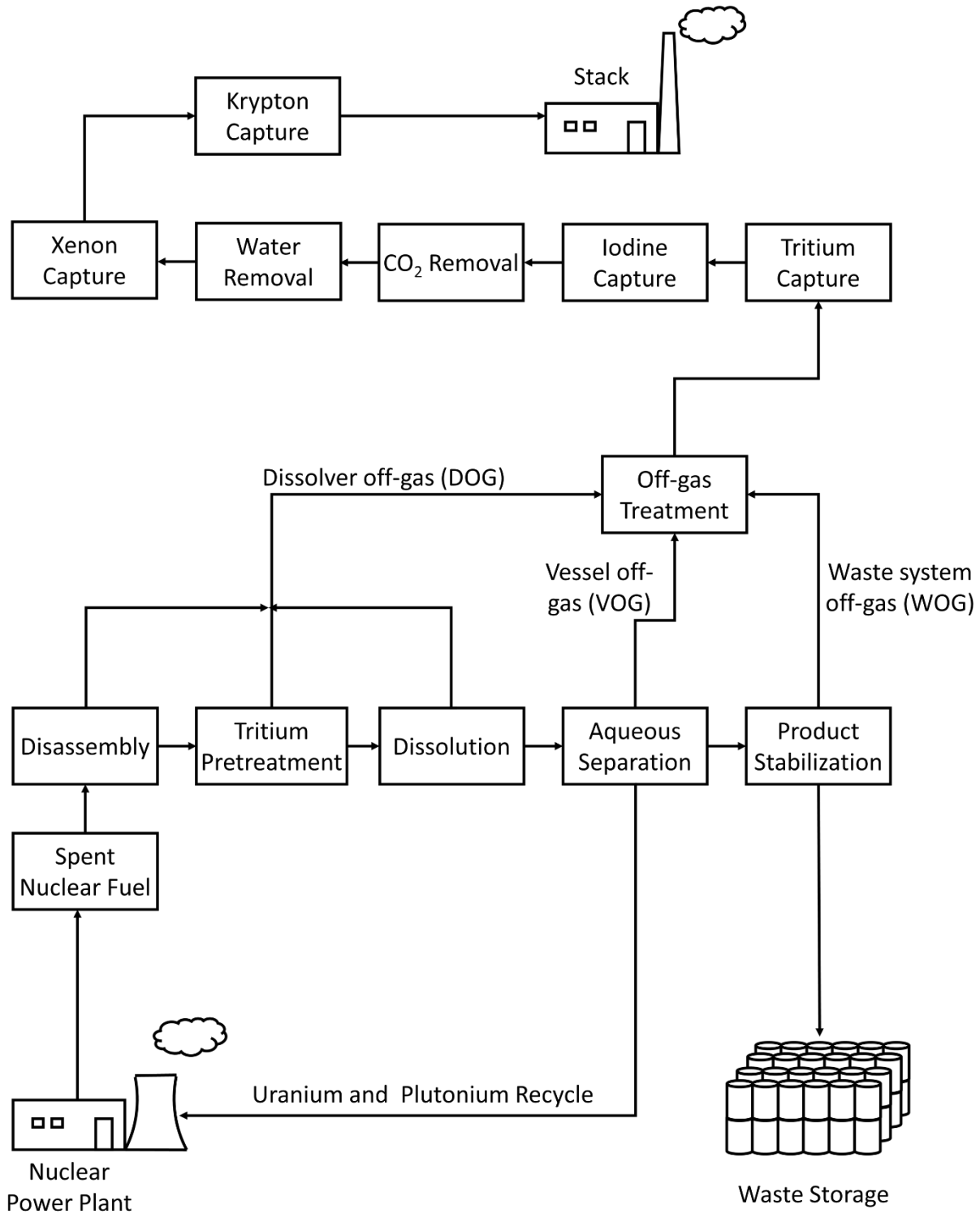


Figure 1-1. A typical nuclear waste treatment system.

The off-gas streams contain T, C, I, Kr and Xe, for which multiple capture systems are required to remove the isotopes. After isotopes are removed, the off-gas streams are emitted to the atmosphere with the concentration regulated by the U.S. Code of Federal Regulations (CFR) Title 10 Part 20 and Title 40 Part 190 issued by U.S. Environment Protection Agency (EPA) and Nuclear Regulatory Commission (NRC).^{16,17}

Radioactive iodine is the species studied in the presented work. In the environment, iodine is mostly in the non-radioactive ^{127}I form; and trace amount ($^{129}\text{I}/^{127}\text{I} = 10^{-7} - 10^{-11}$) in radioactive ^{129}I as the result of human activities.¹⁸⁻²³ The ^{129}I is the product of the ^{235}U fission with a half-life of 1.6×10^7 years and a production ratio of $0.706 \pm 0.032\%$ per ^{235}U fission.²⁴ Another radioactive iodine generated in the nuclear fission is ^{131}I ; it obtains a higher production ratio of $2.878 \pm 0.032\%$ per ^{235}U fission but a much shorter half-life of 8.1 days.²⁵ With a half-life in days, ^{131}I is highly radioactive and dangerous in nuclear accidents but typically not considered in the iodine removal and storage process of the nuclear waste treatment.

However, since the ^{129}I obtains one of the longest half-lives among the products of uranium fission, the long-term environmental and health effects must be considered. Due to human activities especially the nuclear fuel reprocessing, ^{129}I can be detected almost everywhere, from the Norwegian Sea in Europe to the Atacama Desert in Chile,^{26,27} both in soil and water,^{28,29} and even the north pole.^{30,31} As a micronutrient, iodine accumulates easily in the human body, especially in the thyroid.³²⁻³⁵ Therefore, the removal of iodine from nuclear waste is crucial for the purpose of environmental protection and human health.

Based on previous studies, Jubin and Strachan³⁶ estimated the iodine concentrations in the off-gas streams. For a typical light water reactor with the burnup (the heat extracted in unit time per unit mass of nuclear fuel source) of 60 GWd/tIHM (Gigawatt-days per metric ton of initial heavy metal), after 5 years of cooling, the mass of iodine is approximately 350 g/tIHM (gram per metric ton of initial heavy metal). The iodine is released into the off-gas streams during the reprocessing, for DOG and VOG, the concentrations of radioactive iodine are approximately 5-10 ppmv (part per million by volume) and 20-30 ppbv (part per billion by volume), respectively. VOG is released during the uranium and plutonium extraction process. In this process, organic solvents are used and radioactive iodine reacts with the solvent to form organic iodides. The composition of the organic iodides existing in VOG could vary from methyl iodide (CH₃I) to iodododecane (C₁₂H₂₅I), and the prior studies have identified CH₃I and C₁₂H₂₅I to be the most representative of those organic iodides.³⁷⁻⁴² Since the chemical properties of isotopes are relatively similar,⁴³ the non-radioactive ¹²⁷I are used in the experiments conducted to avoid potential harm and additional personal protection procedure. Moreover, the VOG also carries multiple contaminants generated during the reprocessing including NO, NO₂ and H₂O. These components poison the solid adsorbents and decrease the iodine adsorption capacities by oxidizing the metal (e.g., Ag in silver containing materials) in the materials, which will be discussed in **Section 2.5**.

Regulated by the EPA and NRC, the radioactivity limits of iodine in the released air and water are 4×10^{-11} and 2×10^{-7} Ci/m³ or 1.5 and 7400 Bq/m³ (1Bq = 1 atom decayed per second),

respectively.^{16,17} To satisfy the regulation, two major methods, liquid scrubbing and solid adsorption are used.

Generally, the liquid scrubbing method is removing the pollutant by contacting the polluted gas with scrubbing liquid and the pollutant is captured in the liquid through chemical reactions and dissolutions. For iodine removal, multiple scrubbing liquids were used including acids⁴⁴ (e.g. HNO₃), alkalis⁴⁵ (e.g. NaOH, KOH), Mercurex^{46,47} (a mercury-containing acidic liquid), Iodox^{48,49} (a corrosive hyperazeotropic HNO₃-containing liquid) and electrolysis in Co³⁺-HNO₃ solution.⁵⁰ The liquid scrubbing method is being replaced by the solid adsorption method for its disadvantages such as being inefficient at low iodine concentration, requiring corrosion-resistant material for the liquid scrubber, requiring special protection over toxic solutions and requiring additional concentrating or solidifying processes.^{11,51,52}

To overcome these disadvantages, the solid adsorption method was developed. The off-gas flows through the adsorption column containing solid adsorbent and the pollutants are captured, which reduces the operational cost and difficulties significantly. The adsorbents developed include carbon-based adsorbents such as graphene and graphene-based material,⁵³⁻⁵⁶ activated carbon,^{57,58} and chalcogel;⁵⁹⁻⁶² silver-containing adsorbents such as reduced silver functionalized silica aerogel (Ag⁰-Aerogel),⁶³⁻⁶⁵ reduced silver exchanged mordenite (Ag⁰Z),⁶⁶⁻⁶⁸ silver nitrate impregnated alumina (AgA),^{69,70} and silver exchanged faujasite (AgX);⁷¹⁻⁷⁴ other metal-containing inorganic materials such as lead-exchanged mordenite and faujasite,⁷⁵ bismuth-decorated carbon nanofiber,⁷⁶ Bi-Bi₂O₃-TiO₂-C system,⁷⁷ and bismuth mordenite;⁷⁸ and metal

organic frameworks.⁷⁹⁻⁸²

Among these materials, the silver-containing adsorbent is one of the most matured and widely-used materials. The Ag⁰Z and AgA were developed in the 20th century for iodine removal and have been used in the US, France and Japan.⁸³ Their iodine loading capacities are 10-15 wt% and the abilities of regeneration (adsorb and desorb iodine for multiple times) have been demonstrated. However, with the elemental form of Ag exposed, both of the materials are affected significantly by the NO_x in the off-gas streams, which is usually called the ‘aging effect’.^{84,85} The capacity loss in one month exposing to NO₂ may be up to 80-90% of original capacities.

Therefore, a novel silver-containing adsorbent, reduced silver functionalized silica aerogel (Ag⁰-Aerogel) was developed by Matyáš et al. in Pacific Northwest National Laboratory.⁶⁴ Using commercial silica aerogel, they first attached a layer of propylthiol by treating with 3-mercaptopropyltrimethoxysilane (3-MPTMS) in supercritical CO₂ solvent and further installed a layer of Ag⁺ ions on the propylthiol layer by processing with AgNO₃ solutions. After the treatments, the material was reduced at 165 °C for 2h using H₂/Ar mixture to generate silver nanoparticles on the surface.⁶⁴ Approximately 40 wt%, the iodine adsorption capacity of Ag⁰-Aerogel is higher than those of Ag⁰Z and AgA, and the aging resistance is also higher. With the special structure, Ag⁰-Aerogel maintains more than 70% of its capacity when being aged in static NO₂ for 1 month.⁸⁶

The silver containing materials have been researched in national laboratories for decades. Most

of the studies were semi-quantified and application-oriented, focusing on the performance of the adsorption column over time. For example, in experiments performed by Bruffey et al.⁸⁷ the CH₃I was mixed with moist air and passed through an approximately 12 cm-long adsorption system containing Ag⁰-Aerogel. After the experiments, the Ag⁰-Aerogel was collected for neutron activation analysis (NAA) to determine the iodine contents at different depths in the column. With the iodine concentrations measured, the curve of bed length vs. iodine concentrations was generated to determine the penetration depth (furthest depth the CH₃I reached in the column) and conclude the efficiency of column adsorption. A parameter commonly used to describe the effectiveness of the column is the decontamination factor (DF), which is defined as the inlet iodine concentration over outlet concentration. For the 40 ppbv CH₃I adsorption with H₂O present, the DF of a 12 cm Ag⁰-Aerogel adsorption system is estimated to be no less than 382. Similar column experiments of iodine adsorption and dry air/moist air/NO_x aging of Ag⁰Z, AgA were also performed and the results determined mostly focused on describing the effectiveness of columns with certain lengths.^{37,88-91}

As supplementary to the column adsorption experiments, the single layer adsorptions are helpful for understanding the adsorption kinetics, determining the reaction mechanism and providing parameters for column design. The single-layer CH₃I adsorptions on Ag⁰Z were discussed in detail by Jubin⁹² in 1994, in his study, multiple combinations of parameters including pellet size, adsorbate concentration, gas velocity, temperature and water concentration were tested. The methods used and conclusions made provide solid foundations for the follow-up studies.

However, limited by the instruments in the 1990s, some of the kinetics measured and the parameters determined are not ideal, which have been optimized by Nan¹⁵ in 2017.

Nan performed the I₂ and H₂O adsorption on Ag⁰Z. In his study, he identified the optimum adsorption conditions and explained the reaction/aging mechanism between I₂ and Ag⁰Z and H₂O and Ag⁰Z, which enlightened the aging studies done by Choi et al.⁹³ and the work to be presented here.

In this work, the efficiencies of three silver containing materials, Ag⁰-Aerogel, Ag⁰Z and AgA for removing organic iodides in VOG were compared and the results indicated that the Ag⁰-Aerogel is the optimum one for its highest adsorption efficiency and aging resistance.

To further understand the adsorption behaviors on Ag⁰-Aerogel, the single layer organic iodides (including CH₃I, C₃H₇I, C₆H₁₃I, C₈H₁₇I and C₁₂H₂₅I) adsorptions at various concentrations and temperatures were conducted using high precision continuous flow adsorption systems. To analyze the adsorption data collected, multiple kinetic models were applied and compared. The parameters determined were not consistent. To explain such inconsistency, one of the models was optimized and a reaction mechanism was proposed to further explain the optimized model.

Moreover, since the criteria in determining the efficiency of adsorption are different between the I₂ adsorption in ppmv level and organic iodides adsorption in ppbv level, the temperature dependencies of the adsorption were also examined. An abnormally high CH₃I adsorption rate was observed at 200 °C, and to explain this unusual behavior, multiple physical analyses were performed.

Additionally, since the VOG does not only contains CH_3I but also many organic iodides with longer alkyl groups, the adsorptions of other organic iodides were also performed at various temperatures and concentrations. The $\text{C}_6\text{H}_{13}\text{I}$ and $\text{C}_{12}\text{H}_{25}\text{I}$ adsorptions appeared to be zero-order process and the $\text{C}_3\text{H}_7\text{I}$ and $\text{C}_8\text{H}_{17}\text{I}$ obtains much higher adsorption rate than other organic iodides do. To simulate the column adsorptions, the shrinking core model was incorporated into the column adsorption model and the modeling results are comparable with literature studies. The model was further used to estimate the column breakthrough and the behaviors of $\text{C}_{12}\text{H}_{25}\text{I}$ adsorptions.

Chapter 2. Literature Review

2.1 Calculating the ^{129}I Concentration Limit

The limit of radioactivities of ^{129}I in the air and water released are 1.5 and 7400 Bq/m³, respectively, regulated by the EPA and NRC.^{16,17} To convert these values to concentrations, Eq. 2-1 can be applied,¹³

$$\frac{dC_{^{129}\text{I}}}{dt} = \lambda C_{^{129}\text{I}} \quad 2-1$$

where $C_{^{129}\text{I}}$ is the concentration of ^{129}I in air or water (mol/m³) and the rate constant of decay, λ (s⁻¹) is given by,¹³

$$\lambda = \frac{\ln 2}{t_{1/2}} \quad 2-2$$

where $t_{1/2}$ is the half-life of the isotope. To calculate the radioactivities, Eq. 2-1 can be written as,

$$\text{radioactivity} = \frac{\ln 2}{t_{1/2}} N_A C_{^{129}\text{I}} \quad 2-3$$

where the N_A is the Avogadro number (6.022×10^{23} mol⁻¹). Therefore, with $t_{1/2} = 1.6 \times 10^7$ years, the limit concentrations of ^{129}I in the treated gas and water are 1.8×10^{-9} and 8.9×10^{-6} mol of I atom/m³. The concentration in air can also be written as 0.0406 ppbv for organic iodides or 0.0203 ppbv for I₂.

The iodine concentration in VOG was estimated to be 20-30 ppbv by Jubin and Strachan,³⁶ using this concentration range, the decontamination factor (DF) is approximately 500-750, which is comparable with the value achieved by Bruffey et al.⁸⁷ in the Ag⁰-Aerogel column adsorption.

2.2 Adsorptions on Ag⁰Z

The I₂ and CH₃I adsorptions on Ag⁰Z have been studied for decades. The experiments performed can be roughly sorted as column or single layer adsorptions of I₂ or CH₃I, with or without contaminants (H₂O, NO, NO₂) presented.

Multiple comprehensive studies of Ag⁰Z in iodine removal were made by Jubin and colleagues in the 80s and 90s.^{66,67,92,94} In their studies, they examined the CH₃I adsorption on single layer Ag⁰Z with multiple combinations of temperature, size of the pellet, CH₃I concentration, flow rate, etc. It is observed that the shrinking core model can describe the process well at low iodine uptakes. Moreover, they calculated the temperature difference between the pellet and the bulk air, and further concluded that the temperature difference in the system can be neglected.

Another single layer adsorption study was performed by Nan et al.^{15,95} They examined and proposed the optimal condition for the reduction of Ag⁰Z, adsorption temperature and flow rates. The reaction pathway of I₂ on Ag⁰Z was proposed to be the chemical reaction between I₂ and Ag forming AgI, and the overall adsorptions follow the shrinking core process.

Column adsorptions of I₂ and CH₃I on Ag⁰Z were studied in the national laboratories. Bruffey et al.³⁷ performed column adsorptions of the CH₃I on Ag⁰Z. In the experiments, a system consisting of three columns was designed. The first column is a thin bed with a depth of 0.35 cm, used for measuring the adsorption rate. The second column (11.5 cm) is the main bed used for determining the mass transfer through the column and calculating the decontamination factors (DF) by time. The third column is another thin bed of 0.75 cm; it was removed and replaced

periodically, intended to detect breakthrough of the second column. With 40 ppbv CH₃I concentration, the average uptake rate was approximately 2.8×10^{-4} wt%/h. In 100 days, no iodine uptake was measured in the column 3, indicating the breakthrough did not occur in column 2 and the estimated DF was greater than 190.

To simulate the actual off-gas condition, the I₂ and CH₃I co-adsorption on Ag⁰Z with H₂O, NO, NO₂ presented were performed by Soelberg et al.^{90,96,97} The adsorption column they used consisted of 4 sections, with lengths of approximately 1, 4, 5 and 10 cm respectively. The concentration of I₂ ranged from 2 to 50 ppmv, the concentration of CH₃I was from 0 to 50 ppmv, the concentrations of NO and NO₂ ranged from 1000 to 10000 ppmv, and the H₂O concentrations were approximately 4 vol%. The outlet gases from sections were sampled and the concentrations of I₂ and CH₃I were measured using gas chromatography (GC). Depending on the concentrations of the components, the breakthrough of section 3 happened as the shortest of 40 hours and the DF of the full-length adsorption column remained greater than 10000 up to 200-300 hours.

2.3 Adsorptions on Ag⁰-Aerogel

The Ag⁰-Aerogel was developed by Matyáš et al. in 2011 and the procedure has been discussed in **Chapter 1**.⁶⁴ Numerous tests of I₂ and CH₃I column adsorptions on Ag⁰-Aerogel were performed in national laboratories. Using the similar method of Ag⁰Z adsorptions, Bruffey et al.^{87,98,99} measured the 40 ppbv CH₃I average adsorption rate on Ag⁰-Aerogel of approximately 6.9×10^{-4} wt%/h, which is 2.5 times of that of Ag⁰Z. Additionally, in an 84 days column

adsorption, they observed a 16% increase of the Ag⁰-Aerogel bulk density and 11% decrease of the Ag⁰-Aerogel packing height in the column as the results of pellet cracking.

Jubin et al.¹⁰⁰ compared the CH₃I and I₂ column adsorption on Ag⁰-Aerogel and observed that the penetration depth of I₂ is approximately 35% less than that of CH₃I. More specifically, 85%-99.8% of I₂ was captured in the first 2 cm of the column whereas the numbers are 77-92.8% for CH₃I. Such observation indicates that I₂ was adsorbed more rapidly than CH₃I was.

The VOG condition simulation adsorptions on Ag⁰-Aerogel with same set-ups were performed by Soelberg et al.^{91,97,101} At similar inlet stream conditions, I₂ concentration = ~35 ppmv, NO concentration = 10000 ppmv, NO₂ concentration = 10000 ppmv, H₂O concentration = 1.5%, temperature = 150 °C and total flow rate = 1685 sccm, the Ag⁰-Aerogel column performed better than Ag⁰Z column did. The breakthrough time of Ag⁰-Aerogel section 3 is 40 hours whereas that of Ag⁰Z is 30 hours. Therefore, they concluded that the Ag⁰-Aerogel appears to be a very effective and efficient adsorbent.

2.4 Alternative Materials

In recent years, multiple novel materials for iodine removal were developed such as graphene-based materials, bismuth-containing materials and metal organic frameworks (MOF). The iodine adsorptions on graphene aerogel (GA) were examined by Liu et al.⁵⁵ and Scott et al.⁵³ Depending on the pretreatment methods, the iodine adsorption capacities of the materials at room temperature may reach up to 80 wt%, much higher than the traditional Ag-containing materials.

According to the authors,^{53,55} the iodide is physisorbed on the GA and the iodine can be regenerated by immersing the iodine-loaded GA in ethanol solution. After the regenerations, the GA maintains its full capacity in at least three recycles.

The bismuth-containing materials were studied by Zou et al⁷⁷, Han et al⁵⁴. and Chee et al.⁷⁶ The iodine adsorption capacities of bismuth-containing materials are approximately 60 wt% and the operational temperature is 200 °C. The iodine is chemisorbed on the materials through the reaction,



The adsorbed iodide can be regenerated by heating the materials to 400-500 °C, whereas the recycled capacities of the adsorbents were not declared.

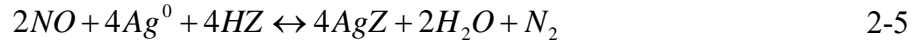
Multiple metal organic frameworks (MOF) with different structures and components were developed.^{79,80,102-104} Their iodine loading capacities vary from 40 wt% to 600 wt%. At 70-80°C, the iodine interacts and binds with the atoms in the MOF and therefore being captured. Reported by He et al.,⁸⁰ the regeneration temperature is 170 °C, and the MOF maintains 70-80% of its full capacity after regeneration.

2.5 Adsorbent Aging

In the off-gas environment simulations conducted (described in **Section 2.2 and 2.3**), the effects of H₂O, NO and NO₂ were observed, and the effect of dry air was also observed by Choi et al.⁹³

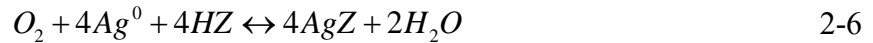
These oxidants decrease the iodine loading capacities of Ag⁰-Aerogel, Ag⁰Z and AgA by

oxidizing the silver nanoparticles.^{85,105,106} When contacting with NO and NO₂, the silver nanoparticles on the surface of Ag⁰Z are oxidized to Ag⁺ and then migrate from the surface to the pores, resulting in the unavailability of the elemental silver. For example, the reaction pathway of NO aging was proposed as,¹⁰⁵



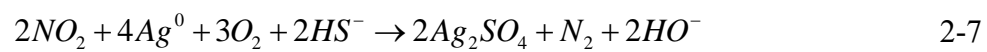
where Ag⁰ and Z denote the elemental silver and mordenite respectively. In one month, with being aged by continuous-flow 1% NO, the Ag⁰Z losses over 95% of its original capacity, and the result is similar when 2% of NO₂ present.

For the dry air and moist air aging process, the oxygen takes the role of NO, and the reaction pathway is,



where the H₂O in the moist air accelerates this process.⁹³ In dry air, Ag⁰Z loses 40% of capacity in one month and the aging effect is more severe with the presence of H₂O, the Ag⁰Z loses 50-55% of capacity.

With the specially designed structure, Ag⁰-Aerogel is more resistant to the aging effects. When contacting with continuous-flow dry air, moist air, NO and NO₂ for one month, the iodide adsorption capacity of Ag⁰-Aerogel decreases for 20%, 19%, 24% and 80%. Choi et al.¹⁰⁵ suggested that the dry air, moist air and NO aging on Ag⁰-Aerogel is the process of Ag₂S formation and the NO₂ aging is the formation of Ag₂SO₄. For example, the pathway of NO₂ aging can be represented as,



The NO_2 oxidizes the Ag^0 to Ag^+ and the Ag^+ further reacts with the thiol (HS^-) functional group and O_2 to form Ag_2SO_4 .

Chapter 3. Experimental

3.1 Experimental Setup

In the experiments, the mass changes were measured by the microbalance and data were recorded using a computer. Figure 3-1 is the schematic diagram of the continuous flow adsorption system and the photos are shown in Figure 3-2. The organic iodides were generated in the Dynacalibrator (VICI[®], Model 450 and 500) by heating the permeation tubes to a desired temperature and flowing the carrier gas (Airgas, Air, Ultra Zero) through. The gas mixture, with flow rate of 500 sccm (standard cubic centimeter per minute) was then passed through the pre-heating coil around the adsorption column (Inner Diameter = 30 mm) and being heated to the adsorption temperature (100, 150 or 200 °C). In the adsorption column, one layer of pellets was placed on a tray and suspended under the microbalance. During the adsorption, mass change was measured by the microbalance and saved by the data acquisition system. In the experiments, the temperature was controlled by the furnace controller and flow rates were controlled by mass flow controllers.

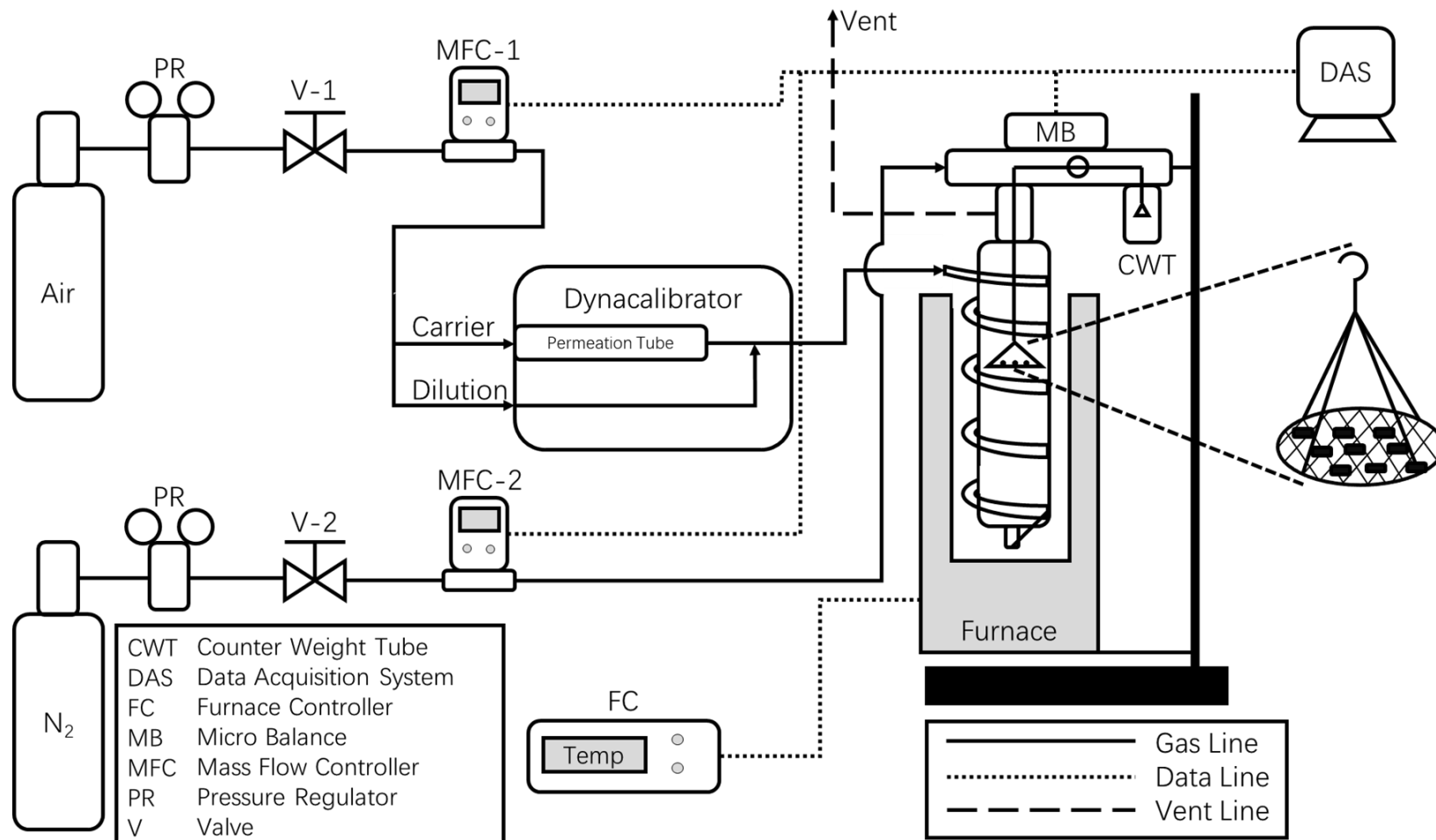


Figure 3-1. Schematic diagram of the continuous flow organic iodides adsorption system.

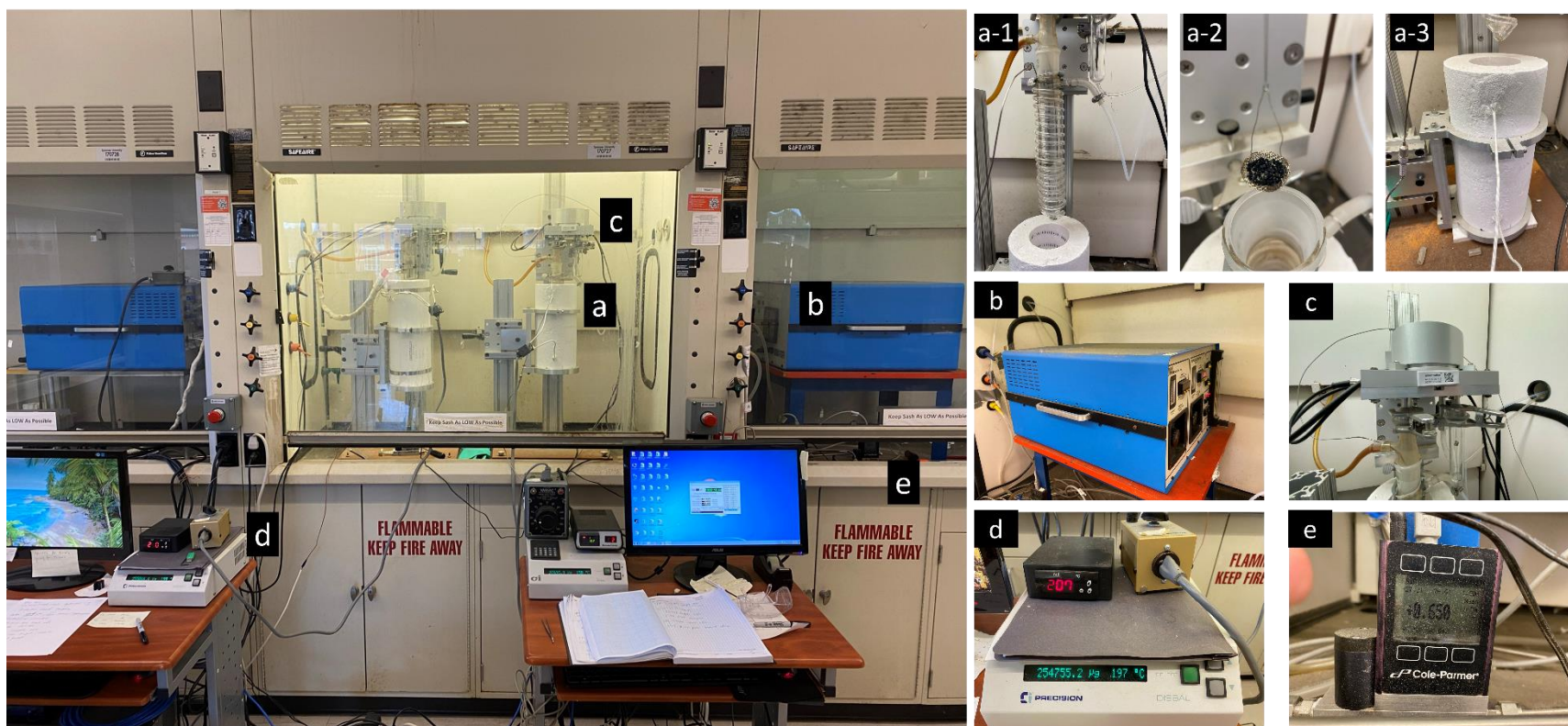


Figure 3-2. Photographs of the continuous flow adsorption system. (a-1) Adsorption column, (a-2) Ag^0 -Aerogel on the tray, (a-3) Furnace, (b) Dynacalibrator, (c) Microbalance head, (d) Microbalance controller and temperature controller, (e) Mass flow controller.

A total of three continuous flow adsorption systems were used in the experiments, Dynacalibrators (Model 500) were used in two of the systems and the other system used Dynacalibrator Model 450. Named after the Dynacalibrator, three systems were labeled as 450, 500-1 and 500-2.

A Dynacalibrator consists of three major parts, the temperature-controlled permeation chamber (two chambers for Model 500 and one chamber for Model 450), the flow rate-controlled dilution line and the vent/flow mode switch.

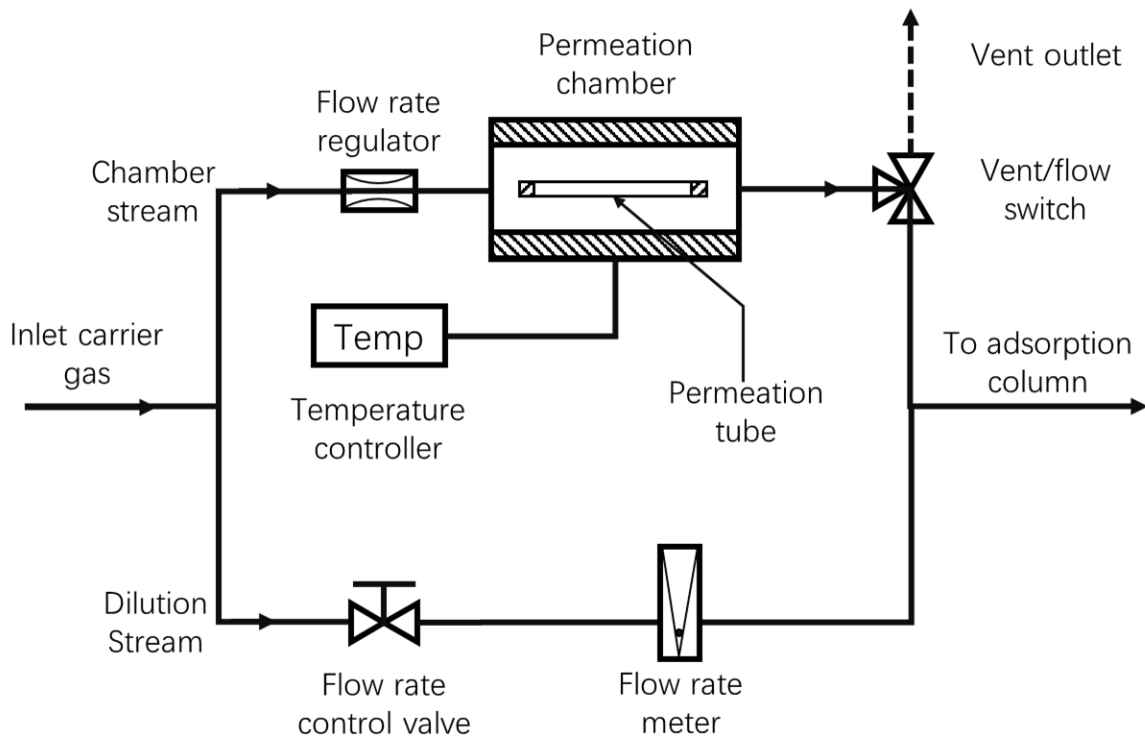


Figure 3-3. The schematic diagram of the Dynacalibrator Model 450 (in flow mode).

A schematic diagram of the Dynacalibrator model 450 in flow mode is shown in Figure 3-3. The carrier gas (Airgas[®], Air, Ultra Zero) flows into the Dynacalibrator and splits into two streams.

The chamber stream first passes through a flow rate regulator and then enters the permeation chamber. By heating up the permeation tube, the organic iodide is released into the chamber stream. The chamber temperature is controlled automatically by the Dynacalibrator and the temperature is set to the target temperature specified by the manufacturer of permeation tubes.

The dilution steam passes through a valve to control the dilution flow rate, and the dilution flow rate is shown by a flow rate meter. By switching to flow mode, the chamber stream mixes with the dilution steam and the mixture further flows to the adsorption column. When the Dynacalibrator is in vent mode, the chamber flow is released directly and only the dilution flow passes to the adsorption column.

The flow rate of the chamber stream is set to be constant by the flow rate regulator; for Dynacalibrator model 450, the chamber stream flow rate is 170 sccm and Dynacalibrator model 500 has two chambers with flow rate of 75 sccm each. Since the permeation rate of the permeation tube is constant, the difference in the chamber flow rate shows no impact on the organic iodide concentration in the outlet stream.

Shown in Figure 3-1, a mass flow controller is used to control the flow rate of the carrier gas entering the Dynacalibrator. Since only one of two chambers is used for generating organic iodide, for Dynacalibrator model 500, the inlet flow rate is set to be 575 sccm for flow mode and 650 sccm for vent mode. For Dynacalibrator model 450, the inlet flow rate is 500 sccm for flow mode and 670 sccm for vent mode.

Three microbalances made by Precision[®] were used in the continuous flow adsorption systems.

The microbalance contains a sample tray and a counterweight; the mass of the sample is measured by an electromagnetic coil in the head of the microbalance. The limit of precision is 0.1 μg and the standard deviation is approximately 35 μg for all microbalances. To avoid the oxidation of the counterweight, nitrogen (Airgas[®], Nitrogen, Ultra High Purity) with 40 sccm flow rate is used as the protective gas.

Two mass flow controllers made by Cole-Parmer[®] are used in each adsorption system to control the flow rates of the adsorption stream and the protective gas stream. The standard deviations of the flow rates are approximately 1 – 2 sccm for all six mass flow controllers. Additionally, one furnace is used in each adsorption system to maintain the adsorption temperature. The temperature is controlled by a temperature controller and the standard deviations are 1 – 2 $^{\circ}\text{C}$ for all three furnaces.

3.2 Organic Iodides

The organic iodides used in the experiments (structures shown in Figure 3-4) are iodomethane (aka. methyl iodide, CAS No: 74-88-4, CH_3I), 1-iodopropane (CAS No: 107-08-4, $\text{C}_3\text{H}_7\text{I}$), 1-iodohexane (CAS No: 638-45-9, $\text{C}_6\text{H}_{13}\text{I}$), 1-iodooctane (CAS No: 629-27-6, $\text{C}_8\text{H}_{17}\text{I}$) and 1-iodododecane (CAS No: 4292-19-7, $\text{C}_{12}\text{H}_{25}\text{I}$).

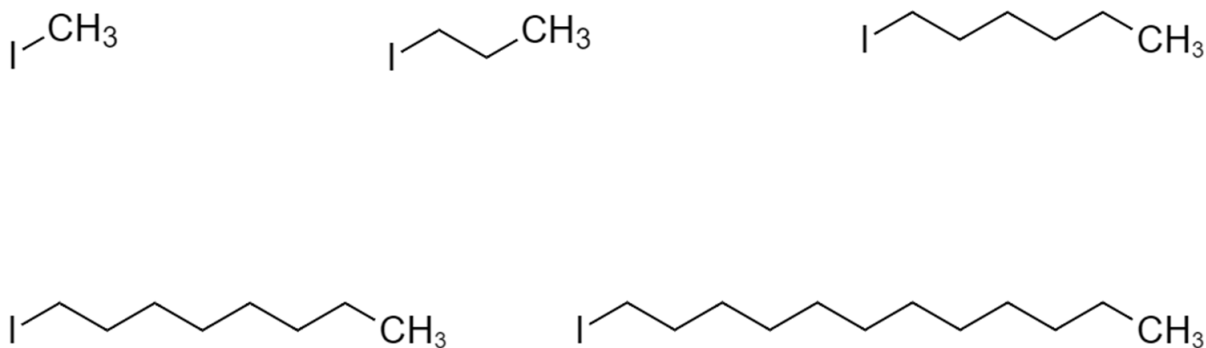


Figure 3-4. Molecule structures of CH_3I , $\text{C}_3\text{H}_7\text{I}$, $\text{C}_6\text{H}_{13}\text{I}$, $\text{C}_8\text{H}_{17}\text{I}$ and $\text{C}_{12}\text{H}_{25}\text{I}$.

CH_3I is toxic; National Institute for Occupational Safety and Health (NIOSH)¹⁰⁷ reported that the LD_{50} (lethal dose, 50% death) for rats is 150 – 200mg/kg and Buckell¹⁰⁸ reported that the LC_{50} (lethal concentration, 50% death) for mice is approximately 57 minutes at 5 mg/L concentration. The toxicities of CH_3I to liver¹⁰⁷, human erythrocytes¹⁰⁹, respiratory system^{110,111} and reproductive system¹¹² were also reported. However, the detailed toxicity data were rarely reported for organic iodides with longer alkyl groups.

The permeation tubes were ordered from VICI[®]. The desired concentrations and flow rates of gas mixture were provided to the manufacturer and VICI[®] made the Dynacal[®] permeation tubes as requested. VICI[®] describes the permeation tubes as:

The perm tube, a sealed permeable cylinder containing the desired permeant reference material, is the most widely used of the various permeation devices. Release of the chemical occurs by permeation through the walls of the PTFE tube for the entire length between the impermeable plugs. A wide range of rates can be achieved by varying the length and thickness of the tube, with typical rates ranging from 5 ng/min to 50,000 ng/min.



Figure 3-5. The 104 ppbv CH₃I permeation tube.

The permeation tubes (Figure 3-5) are made by polytetrafluoroethylene (PTFE), containing liquid organic iodide. Organic iodide diffuses through the tube wall and the permeation rate can be controlled by the chamber temperature. The flow rates provided by the manufacture are measured in ng/min, and the organic iodides concentrations in ppbv (part per billion by volume) and mol/cm³ are calculated using,

$$FR(\text{mol of orgI} / \text{min}) = \frac{PR(\text{ng of orgI} / \text{min})}{MW} \times 10^{-9} \quad 3-1$$

$$FR(\text{cm}^3 \text{ of orgI} / \text{min}) = \frac{RT_{ads} \times FR(\text{mol of orgI} / \text{min})}{P_{ads}} \quad 3-2$$

$$FR(\text{cm}^3 \text{ of Air} / \text{min}) = \frac{FR(\text{cm}^3 \text{ of Air at standard condition} / \text{min}) \times T_{ads}}{T_{std}} \quad 3-3$$

$$C(\text{ppbv of orgI}) = \frac{FR(\text{cm}^3 \text{ of orgI} / \text{min})}{FR(\text{cm}^3 \text{ of Air} / \text{min})} \times 10^9 \quad 3-4$$

$$C(\text{mol of orgI} / \text{cm}^3) = \frac{C(\text{ppbv of orgI})P_{ads}}{RT_{ads}} \times 10^{-9} \quad 3-5$$

where FR is the flow rate (mol/min or cm^3/min), PR is the permeation rate (ng/mol), MW is the molecular weight of organic iodides (g/mol), R is the gas constant ($83.14 \text{ cm}^3 \cdot \text{bar} \cdot \text{K}^{-1} \cdot \text{mol}^{-1}$), T is the temperature (K) and P is the pressure (bar). The units of flow rate and concentration are listed in the parentheses. Subscript *std* denotes the standard condition (273 K, 1 bar) and *ads* denotes adsorption conditions.

The target concentrations of CH_3I permeation tubes were, 100, 250, 1000 and 10000 ppbv; $\text{C}_3\text{H}_7\text{I}$, 100 ppbv; $\text{C}_6\text{H}_{13}\text{I}$, 100 and 1000 ppbv; $\text{C}_8\text{H}_{17}\text{I}$, 100 ppbv; and $\text{C}_{12}\text{H}_{25}\text{I}$, 100 and 1000 ppbv. Limited by the manufacturing techniques, the concentrations received are not identical to those of the requests. Additionally, the 10000 ppbv permeation device was provided as a 3-tube kit, with the concentration of each tube is approximately 3000 ppbv and the total concentration is 9584 ppbv.

The permeation rates were measured by the manufacture using a method similar to thermogravimetric analysis (TGA). The permeation tubes were heated to the target temperatures and mass losses were monitored continuously. After a certain period of time, the permeation rates can be calculated, and the accuracies were also reported. To reduce the losses of organic iodides

during storage, the permeation tubes were placed in a laboratory refrigerator.

The specifications of all permeation tubes used are listed in Table 3-1; the permeation rates, accuracies and the chamber temperature were provided by the manufacturer. The concentrations in ppbv at 500 sccm flow rate of all permeations tubes are, CH₃I-104 ppbv, CH₃I-245 ppbv, CH₃I-1044 ppbv, CH₃I-9584 ppbv, C₃H₇I-96 ppbv, C₆H₁₃I-101 ppbv, C₆H₁₃I-733 ppbv, C₈H₁₇I-60 ppbv, C₁₂H₂₅I-113 ppbv and C₁₂H₂₅I-606 ppbv.

The vapor pressures of the organic iodides are reported in EPA Distributed Structure-Searchable Toxicity (DSSTox) database, and the vapor pressure of CH₃I, C₃H₇I, C₆H₁₃I, C₈H₁₇I and C₁₂H₂₅I are 405, 43.1, 1.4, 0.25 and 1.4×10^{-2} mmHg, or, 5.33×10^8 , 5.7×10^7 , 1.8×10^6 , 3.3×10^5 and 1.8×10^4 ppbv respectively.¹¹³⁻¹¹⁷ Considering the C₁₂H₂₅I-606 ppbv adsorption, the highest C₁₂H₂₅I concentration may exist in the chamber stream (Figure 3-3) of Dynacalibrator model 500 with chamber flow rate of 75 sccm, and the concentration is approximately 4000 ppbv, far lower than the vapor pressure of C₁₂H₂₅I. Therefore, the condensation of organic iodides may not happen anywhere in the adsorption system.

Organic Iodides	Permeation Rate (ng/min) *	Accuracy *	Chamber Temperature* (°C)	Conc' (ppbv)	Conc' at 100°C (mol/cm ³)	Conc' at 150°C (mol/cm ³)	Conc' at 200°C (mol/cm ³)
CH ₃ I	329.00	±1.82%	45	104	3.39×10 ⁻¹²	2.99×10 ⁻¹²	2.68×10 ⁻¹²
	775.02	±1.87%	60	245	8.00×10 ⁻¹²	7.05×10 ⁻¹²	6.31×10 ⁻¹²
	3307.29	±0.44%	35	1044	3.41×10 ⁻¹¹	3.01×10 ⁻¹¹	2.67×10 ⁻¹¹
	9587.03**	±0.47%	35	3027	9.89×10 ⁻¹¹	8.72×10 ⁻¹¹	7.80×10 ⁻¹¹
	10352.80**	±0.11%	35	3269	1.07×10 ⁻¹⁰	9.42×10 ⁻¹¹	8.42×10 ⁻¹¹
	10412.60**	±0.37%	35	3288	1.07×10 ⁻¹⁰	9.47×10 ⁻¹¹	8.47×10 ⁻¹¹
C ₃ H ₇ I	366.07	±1.28%	50	96	3.15×10 ⁻¹²	2.78×10 ⁻¹²	2.49×10 ⁻¹²
C ₆ H ₁₃ I	478.46	±2.97%	60	101	3.30×10 ⁻¹²	2.91×10 ⁻¹²	2.60×10 ⁻¹²
	3468.20	±1.50%	60	733	2.39×10 ⁻¹¹	2.11×10 ⁻¹¹	1.89×10 ⁻¹¹
C ₈ H ₁₇ I	323.62	±1.65%	80	60	1.97×10 ⁻¹²	1.74×10 ⁻¹²	1.56×10 ⁻¹²
C ₁₂ H ₂₅ I	749.75	±4.35%	100	113	3.71×10 ⁻¹²	3.27×10 ⁻¹²	2.92×10 ⁻¹²
	4009.52	±2.38%	100	606	1.98×10 ⁻¹¹	1.75×10 ⁻¹¹	1.56×10 ⁻¹¹

* Provided by the manufacturer

**3-tube kit, total concentration = 9584 ppbv

Table 3-1. Specifications of the permeation tubes, concentrations calculated for 500 sccm flow rate.

3.3 Materials

Figure 3-6 shows the materials tested in this presented work include reduced silver functionalized aerogel (Ag^0 -Aerogel), hydrogen reduced silver exchanged mordenite (Ag^0Z) and silver nitrate impregnated alumina (AgA). The Ag^0 -Aerogel was provided by Pacific Northwest National Laboratory (PNNL); the Ag^0Z was prepared by reducing the IONEX-TYPE AgZ (Ag-900 E16, Lot# 111515-1, Molecular Products, Inc) in 4% H_2 /96 % Argon (Airgas) at 400 °C for 24h; and the AgA was self-prepared following the procedure described in **Section Chapter 4**.



Figure 3-6. Photographs of Ag^0 -Aerogel, Ag^0Z and AgA.

The properties of the materials are listed in Table 3-2. To measure the chemisorption iodine loading capacity and the available silver content for reaction, the 50 ppmv I_2 adsorptions at 150 °C on the three materials were performed using the continuous flow adsorption system. The chemisorption iodine loading capacities determined (Figure 3-7) are, 37.2, 12.8 and 11.2 wt% for

Ag⁰-Aerogel, Ag⁰Z and AgA, respectively. The iodine loading capacities of Ag⁰-Aerogel vary between different manufacturing batches, and the values were reported up to 48 wt%.^{64,98,118} The capacity of Ag⁰Z was reported by Nan et al.⁹⁵ as more than 12 wt% and a capacity of 10.1 wt% for AgA was measured by Jordan and Jubin.¹¹⁹

Properties	Ag⁰-Aerogel	Ag⁰Z	AgA
Density (g/cm ³)	0.58	1.87	0.89
Diameter (mm)	2.0	1.8	2.0
Silver Content (wt%)	31.6	10.9	9.5
Iodine Chemisorption Capacity (wt%)	37.2	12.8	11.2
BET Surface Area (m ² /g)	291.1	178.9	254.6
BJH Pore Volume (cm ³ /g)	0.263	0.097	0.450

Table 3-2. Properties of Ag⁰-Aerogel, Ag⁰Z and AgA.

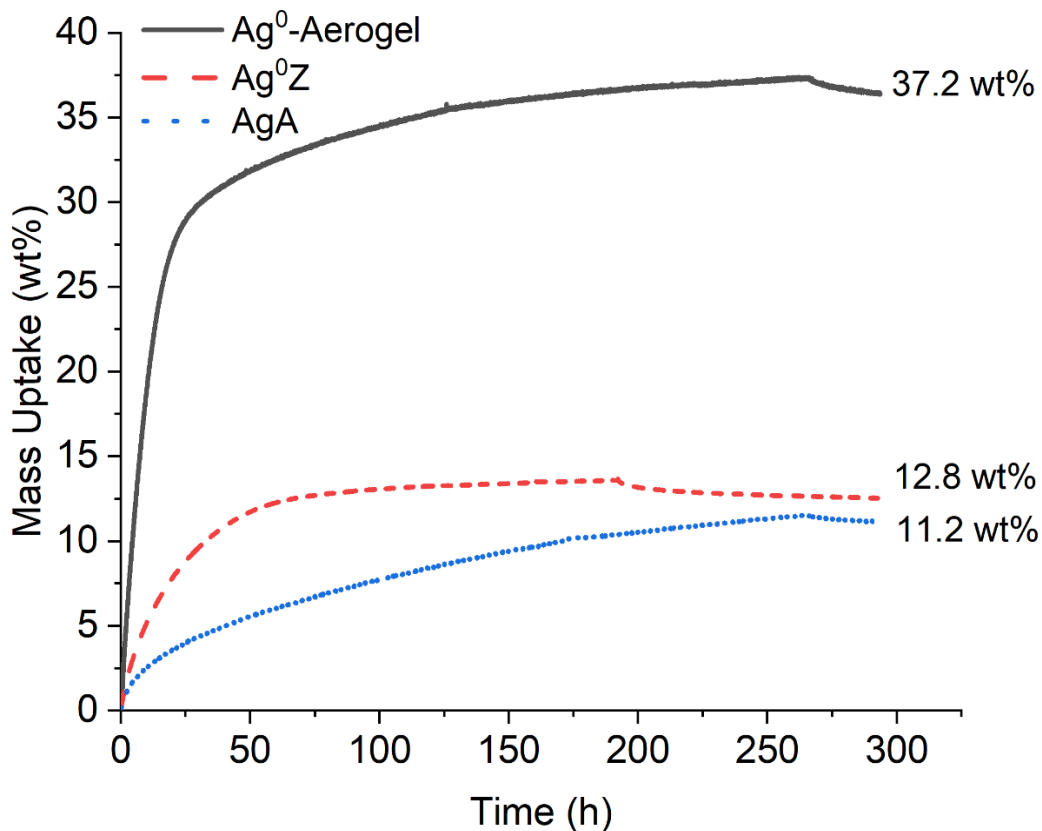


Figure 3-7. I₂ adsorption kinetics of Ag⁰-Aerogel, Ag⁰Z and AgA.

3.4 Experimental Conditions

By performing the iodide adsorption on Ag⁰Z at various flow rates, Nan et al.⁹⁵ reported no significant impact of the iodine uptake at superficial gas velocity greater than 1.1 m/min. More specifically, Nan performed the I₂ adsorption on Ag⁰Z at 150 °C with flow rates and concentrations combinations of 9 ppmv - 2000 sccm, 9 ppmv - 500 sccm, 25 ppmv - 1000 sccm, 25 ppmv - 500 sccm, 50 ppmv - 500 sccm, and 50 ppmv - 250 sccm. Comparing to 50 ppmv - 500 sccm adsorption, both uptake rate and maximum iodine adsorption capacity decreased at 50

ppmv - 250 sccm condition, whereas the adsorption behaviors remained similar at other conditions.

The inner diameter of the adsorption column is 30 mm; therefore, Nan et al.⁹⁵ calculated the superficial gas velocity of 1.1 m/min and reported it as the minimum gas velocity with no impact on adsorption behaviors. Similar results were also suggested by Jubin.⁹² Jubin performed approximately 1000 ppbv CH₃I adsorption on Ag⁰Z with superficial velocities of 1, 2, 5, and 10 m/min and no significant impact of uptake rate was observed. Based on their conclusions, 500 sccm is selected to be the flow rate of all experiments in this presented work.

Additionally, the optimum temperature for I₂ adsorption on Ag⁰Z was also examined by Nan et al.⁹⁵ By performing the 10 – 50 ppmv I₂ adsorption on Ag⁰Z at 100, 150 and 200 °C, Nan observed a maximum I₂ adsorption capacity at 150 °C and an increasing uptake rate with increasing temperature. Since the higher I₂ adsorption capacity is preferred for ppmv level adsorption, Nan et al. reported 150 °C as the optimum I₂ adsorption temperature. The 150 °C temperature was also used in multiple iodine removal experiments including, I₂ and CH₃I column adsorption on Ag⁰-Aerogel,^{87,100} NO₂ aging of Ag⁰Z and Ag⁰-Aerogel,⁸⁸ I₂ and CH₃I column adsorption on Ag⁰Z¹⁰⁰ and I₂ and CH₃I single layer adsorption on Ag⁰Z^{15,92}. Therefore, 150 °C was selected to be the standard adsorption temperature and 100 and 200 °C experiments were also performed.

3.5 Analytical Techniques

3.5.1 SEM-EDX

Scanning electron microscopy with energy dispersive x-ray analyses (SEM-EDX) were conducted to observe the structure and surface composition changes of the sample. The SEM analyses were performed using JEOL JSM IT100LA at SUNY College of Environmental Science and Forestry (SUNY-ESF). Secondary electron detector (SED) images were collected for observing the surface structure changes and backscattered electron composition (BEC) images with elemental mappings were used for identifying the surface compositions and the distributions of silver. The acceleration voltage was 10-15 kV and the probe current is 20-30 nA for SED mode and 55-65 nA for BEC mode.

3.5.2 XPS

X-ray photoelectron spectroscopy (XPS) analyses were performed to determine the surface compositions and the oxidation states of elements using the Scienta Omicron ESCA-2SR at Cornell University. The operating pressure is 1×10^{-9} Torr, and the monochromatic Al K α x-rays (1486.6 eV) were generated at 300W (15 kV; 20mA). For each sample, a wide survey scan was performed to measuring the surface composition and regional elemental scans of Ag and I. The regional C spectrum was also obtained to calibrate all other spectra collected.

3.5.3 Nitrogen Titration

The nitrogen titration analyses were used to determine the porosities, surface areas, pore volumes and pore size distributions of the materials. The adsorption isotherms were collected using Micrometrics ASAP 2020 Surface Area and Porosity Analyzer. The Brunauer-Emmett-Teller (BET) method¹²⁰ was used to determining the BET surface area; the Harkins-Jura (HJ) t-plot method¹²¹ was used to measuring the micropore volume, micropore area and external surface area; the Barrett-Joyner-Halenda (BJH) method¹²² was used to estimate the surface area, pore volume and pore distribution of mesopores; and Density Function Theory (DFT)¹²³ was used to obtain a general pore size distribution.

3.6 Modeling

3.6.1 Shrinking Core Model

The Shrinking Core Model (SCM) model has been widely used in the nuclear waste treatment area including water adsorption on molecular sieves 3A¹²⁴, water adsorption on Ag⁰Z^{15,125}, I₂ adsorption on Ag⁰Z^{15,95}, CH₃I adsorption on Ag⁰Z⁹², etc. In a typical SCM gas-solid adsorption process, the adsorbate first reaches the pellet surface by diffusing through a gas film around the pellet. Then, the adsorbate reacts with the adsorbent surface. When the surface is fully reacted, the adsorbate diffuses into the pellet and reacts with the second layer of the adsorbent. Because the size of the unreacted core decreases as the adsorption proceeds, the model is named 'shrinking core'. The SCM was developed by Yagi and Kunii¹²⁶ in 1955 and modified by

Levenspiel¹²⁷. It consists of a gas film diffusion term, pore diffusion term and reaction term. The SCM assumes that the reaction sites are evenly distributed in the pellet. Additionally, this model also assumes that the reaction between the adsorbent and adsorbate is relatively fast. Therefore, the adsorbate is limited at the reacting surface.

SCM relates the time and adsorption mass by using 3 parts shown in Eq. 3-6:

$$t = \frac{q}{q_e} \tau_1 + \left(1 + 2 \left(1 - \frac{q}{q_e} \right) - 3 \left(1 - \frac{q}{q_e} \right)^{2/3} \right) \tau_2 + \left(1 - \left(1 - \frac{q}{q_e} \right)^{1/3} \right) \tau_3 \quad 3-6$$

where q is the average sorbate concentration in adsorbent (mol/g) at time t (s) and q_e is the saturation sorbate concentration in adsorbent (mol/g). In the SCM, the ‘saturation’ is when the adsorbent reaches its maximum capacity and the uptake mass no longer changes, indicating that all available sites (Ag) are occupied by the adsorbate or deactivated by other toxic gases such as NO_x for Ag⁰-Aerogel adsorption.^{86,91} For convenience, q and q_e are sometimes represented as ‘mass uptake’, ‘adsorption capacity’ or ‘loading capacity’ with the unit ‘wt%

($\frac{\text{Uptake mass}}{\text{Adsorbent mass}}$), which can be easily converted by the atomic mass of iodine. τ_1 , τ_2 , and τ_3 are

the gas film diffusion term, pore diffusion term, and 1st order reaction term respectively. By

assuming the gas-solid reaction is 1st order, τ_1 , τ_2 , and τ_3 can be calculated by Eq. 3-7 to 3-9.

$$\tau_1 = \frac{R_a q_e \rho_p}{3b k_f C_b} \quad 3-7$$

$$\tau_2 = \frac{R_a^2 q_e \rho_p}{6b D_p C_b} \quad 3-8$$

$$\tau_3 = \frac{R_a q_e \rho_p}{b k_s C_b} \quad 3-9$$

where R_a is the radius of the pellet (cm), ρ_p is the density of the pellet (g/cm³), C_b is the bulk adsorbate concentration (mol/cm³), k_f is the gas film mass transfer coefficient (cm/s), D_p is the pore diffusivity (cm²/s), k_s is the 1st order reaction rate constant (cm/s) and b is the stoichiometric coefficient of Ag in Ag-organic iodides reaction, which is 1. Since an analytical solution with respect to q is not available and t was used for model fitting. After the parameters were obtained, the q 's were calculated using the parameters and the relative error was determined.

To improve the SCM, the unnecessary 1st order reaction assumption may be replaced by the n^{th} order reaction, which τ_1 and τ_2 remain the same and τ_3 is replace by the n^{th} order reaction term τ_3^* given in Eq. 3-10:

$$\tau_3^* = \frac{R_a q_e \rho_p}{b k_s^* C_b^n} \quad 3-10$$

where n is the reaction order and k_s^* is the n^{th} order reaction rate constant ((cm/s)·(mol/cm³)¹⁻ⁿ)

To reduce the variables to be fitted in the model and increase the accuracy of the result, an alternative method of determining k_f was used by Nan et al.⁹⁵ k_f can be determined using Eq. 3-11 to 3-14.¹²⁸⁻¹³¹

$$k_f = \frac{D_{AB} Sh}{2R_a} \quad 3-11$$

$$Sh = 2 + 0.6 Sc^{\frac{1}{3}} Re^{\frac{1}{2}} \quad 3-12$$

$$D_{AB} = \frac{0.00143T^{1.75}}{PM_{AB}^{1/2} \left[(\sum \nu)_A^{1/3} + (\sum \nu)_B^{1/3} \right]^2} \quad 3-13$$

$$M_{AB} = \frac{2}{1/M_A + 1/M_B} \quad 3-14$$

Sh , Sc , and Re are the Sherwood number, Schmidt number, and Reynolds number respectively, D_{AB} is the binary diffusion coefficient (cm^2/s), T is the temperature (K), P is the pressure (bar), M_{AB} is the average molecular weight of species A , organic iodides, and species B , air, and v is the atomic diffusion volume (cm^3). For CH_3I adsorption, $M_{AB} = 48.12 \text{ g/mol}$, $(\sum v)_A = 52.63 \text{ cm}^3$ and $(\sum v)_B = 19.7 \text{ cm}^3$.¹²⁹ The D_{AB} for CH_3I at $150 \text{ }^\circ\text{C}$ determined using this method is approximately $0.196 \text{ cm}^2/\text{s}$, which is similar to the value of $0.207 \text{ cm}^2/\text{s}$ measured experimentally by Matsunaga et al.¹³²

The differential form of the diffusion term of the SCM is also used in the modeling the water adsorption/desorption, which is,

$$V \frac{dq(r,t)}{dt} = 4\pi r^2 D \frac{dq(r,t)}{dr} \quad 3-15$$

where $q(r;t)$ is the sorbate concentration (mol/g) at radius r (cm) at time t (sec).

3.6.2 Volume Reaction Model

Another model used to determine the adsorption on porous material is the volume reaction model (VRM), also known as the progressive conversion model. As the VRM described, the adsorbate diffuses into the pellet and with a concentration gradient that exist during the adsorption.

According to its concentration, the adsorbate reacts with the adsorbent at different rates. The

VRM was proposed by Ramachandran and Doraiswamy^{133,134}, which is,

$$\ln \left[\frac{1-q/q_e}{W_1(1+\zeta)} - \frac{W_2}{W_1} \exp(-\theta) \right] + \theta = \frac{\phi_v^2}{B_{12}} \left[1 - \frac{1-q/q_e}{W_1(1+\zeta)} + \frac{W_2}{W_1} \exp(-\theta) \right] \quad 3-16$$

where,

$$\theta = bk_v C_b t \quad 3-17$$

and,

$$\phi_v^2 = \frac{R_a^2 k_v C_{Ag}}{D_p} \quad 3-18$$

For spherical pellets, the geometry coefficients ζ , B_{12} , W_1 and W_2 are 2, 10.5, 0.233 and 0.1, respectively.¹³⁴ θ is the dimensionless time, k_v is the rate constant for volume reaction ($\text{cm}^3/\text{mol/s}$), ϕ is the Thiele modulus, C_{Ag} is the silver concentration (mol/cm^3) and the symbols not mentioned are same as SCM.

The Thiele modulus ϕ represent the ratio of the reaction rate to diffusion rate. For $\phi \gg 1$, the diffusion is much slower than the reaction rate; the adsorption is therefore the diffusion-controlled process and vice versa. The VRM was fit by minimize the difference between the two sides of Eq. 3-16.

3.6.3 Linear Driving Force Model

The Linear Driving Force Model (LDFM) was proposed by Glueckauf and Coates¹³⁵; it is commonly used for its simplicity and the straight-forward physical interpretation. It is assumed that the reaction occurs homogenously and the average reaction rate is proportional to the amount of remaining sites in the pellet. The model is given by Eq. 3-19,

$$\frac{dq}{dt} = k_{LDF} (q_e - q) \quad 3-19$$

where k_{LDF} is the linear driving force mass transfer coefficient (s^{-1}).

For isothermal adsorption, k_{LDF} can be estimated by,¹³⁶

$$\frac{1}{k_{LDF}} = \frac{R_a}{3k_f} \left(\frac{q_e \rho_p}{C_b} \right) + \frac{R_a^2}{15\varepsilon_p D_a} + \frac{\bar{R}_i^2}{15D_i} \quad 3-20$$

where ε_p is the porosity of the pellet, \bar{R}_i is the radius of the micropore, D_a and D_i are the macropore and micropore diffusivity.

The SCM, VRM and LDFM are similar in their physical implications, adsorbate diffuses into the pellet and reacts with the available sites with the rate related to the in-pellet adsorbate concentration. However, the diffusion and the concentration gradient of adsorbate in the three models are different.

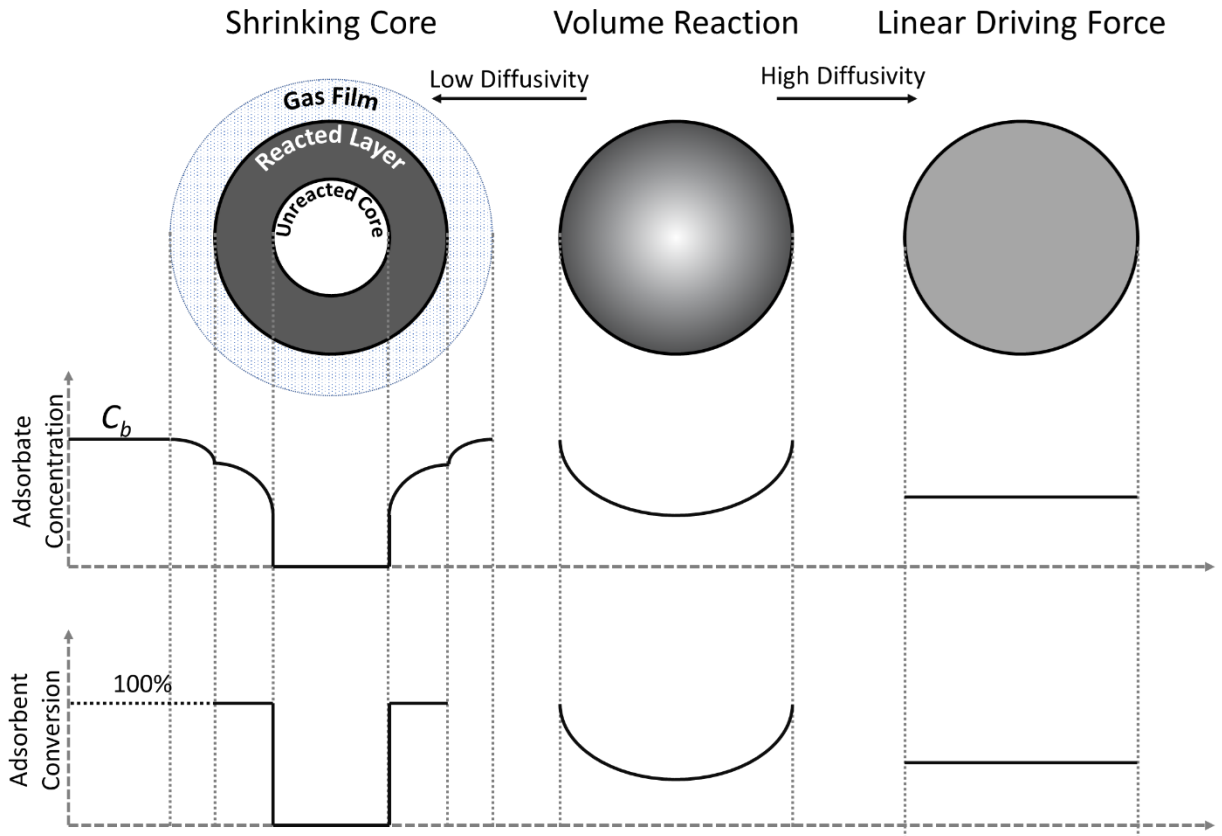


Figure 3-8. Comparison of the shrinking core, volume reaction and linear driving force models

(Curves only represent trends).

Figure 3-8 represents the relative adsorbate concentrations and the fractional conversions of the adsorbent of the SCM, VRM and LDFM. The diffusivity in VRM is moderate and a concentration gradient exists in the pellet. The shrinking core model represents the low diffusivity; the diffusion of adsorbate is much slower than the consumption and a reacting surface may form in this circumstance. When diffusivity increases significantly and the concentration gradient is negligible, the adsorption may be described by the LDFM with homogenous adsorbate concentration and adsorbent conversion. Additionally, it is important to

notice that the concentration and conversion are average values and the diffusivities can be interpreted by Eq. 3-20.

3.6.4 Pore Diffusion Model

The pore diffusion model (PDM) was developed by Ruckenstein et al.¹³⁷, and it considers both macropore and micropore diffusion. In the PDM, the pellets consist of macropores and the macropores consist of micropores. The adsorbate first diffuses into the macropores and further into the micropores. Therefore, the diffusivities of both macro and micro pores can be determined.

The PDM assumes that the adsorptions in the pores are linear¹⁵, and the macropore diffusion is expressed as,

$$\frac{D_a \varepsilon_a}{r_a^2} \frac{\partial}{\partial r_a} \left(r_a^2 \frac{\partial C_a}{\partial r_a} \right) = \varepsilon_a \frac{\partial C_a}{\partial t} + S_a \frac{\partial C_{sa}}{\partial t} + 4\pi m \bar{R}_i^2 \varepsilon_i D_i \left(\frac{\partial C_i}{\partial r_i} \right)_{r_i = \bar{R}_i} \quad 3-21$$

From left to right, Eq. 3-21 implies that the flux of adsorbate equals to the summation of volume accumulation in macropores, surface adsorption in macropores and the diffusion to micropores.

The micropores diffusion can be expressed as,

$$\frac{D_i \varepsilon_i}{r_i^2} \frac{\partial}{\partial r_i} \left(r_i^2 \frac{\partial C_i}{\partial r_i} \right) = \varepsilon_i \frac{\partial C_i}{\partial t} + S_i \frac{\partial C_{si}}{\partial t} \quad 3-22$$

where the physical meaning is similar to that of macropore diffusion. In Eq. 3-21 and 3-22, a and i denote the macropore and micropore, D is the diffusivity (cm²/s), m is the number of micropores per unit volume of macropore, ε is the porosity, C is the fluid phase sorbate

concentration (mol/cm³), C_s is the adsorbed phase concentration on the pore surface (mol/cm²), S is the pore surface area (cm²), \bar{R} is radius of pores (cm) and r is the distance from pore center to the pore surface (cm).

The analytical solution for Eq. 3-21 and 3-22 is,¹³⁷

$$\frac{q}{q_e} = \frac{\left[1 - \frac{6}{\pi^2} \sum_{\bar{n}=1}^{\infty} \frac{1}{\bar{n}^2} \exp\left(-\frac{\bar{n}^2 \pi^2 D_a' t}{\bar{R}_a^2}\right) \right] + \frac{\beta}{3\alpha} \left[1 - \frac{6}{\pi^2} \sum_{\bar{n}=1}^{\infty} \frac{1}{\bar{n}^2} \exp\left(-\frac{\bar{n}^2 \pi^2 D_i' t}{\bar{R}_i^2}\right) \right]}{1 + \frac{\beta}{3\alpha}} \quad 3-23$$

where \bar{n} is the summation index and other parameters are given as,

$$D_a' = \frac{D_a}{1 + \frac{H_a S_a}{\varepsilon_a}} \quad 3-24$$

$$D_i' = \frac{D_i}{1 + \frac{H_i S_i}{\varepsilon_i}} \quad 3-25$$

$$\alpha = \frac{D_i' \bar{R}_a^2}{D_a' \bar{R}_i^2} \quad 3-26$$

$$\beta = \frac{3(1 - \varepsilon_a) \varepsilon_i}{\varepsilon_a} \frac{D_i' \bar{R}_a^2}{D_a' \bar{R}_i^2} = \frac{3(1 - \varepsilon_a) \varepsilon_i}{\varepsilon_a} \alpha \quad 3-27$$

where H is the Henry's law constant of adsorption, and D' is the effective diffusivity.

In the numerator of Eq. 3-23, the left term represents the macropore diffusion and the right one represents the micropore diffusion. If the macropore diffusion is the rate-limiting step, Eq. 3-23 can be simplified as,¹³⁷

$$\frac{q}{q_e} = 1 - \frac{6}{\pi^2} \sum_{\bar{n}=1}^{\infty} \frac{1}{\bar{n}^2} \exp\left(-\frac{\bar{n}^2 \pi^2 D_a t}{\bar{R}_a^2 (1 + K(1 - \varepsilon_p) / \varepsilon_p)}\right) \quad 3-28$$

where,

$$K = \frac{q_e \rho_p}{C_b} \quad 3-29$$

If the micropore diffusion is the rate-limiting step, the process can be expressed as,¹³⁷

$$\frac{q}{q_e} = 1 - \frac{6}{\pi^2} \sum_{\bar{n}=1}^{\infty} \frac{1}{\bar{n}^2} \exp\left(-\frac{\bar{n}^2 \pi^2 D_i t}{\bar{R}_i^2}\right) \quad 3-30$$

3.6.5 Fick's Law

Generally, the diffusion in the spherical adsorbent can be described by the Fick's law¹²⁷, which is

$$\frac{\partial q(r,t)}{\partial t} = D_p \frac{1}{r^2} \frac{\partial}{\partial r} \left(r^2 \frac{\partial q(r,t)}{\partial r} \right) \quad 3-31$$

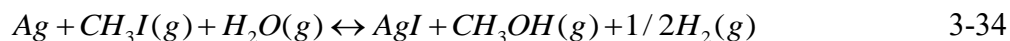
where $q(r,t)$ is the sorbate concentration (mol/cm³) at radius r (cm) at time t (s). The average sorbate concentration $q(t)$ can be calculated using,

$$q(t) = \frac{1}{V} \int_0^r 4\pi r^2 q(r,t) dr \quad 3-32$$

where V is the volume of the pellet (cm³) and r is the distance from the pellet center to surface.

3.7 Difficulties in Organic Iodides Adsorption on Ag⁰-Aerogel

After the comparison of three materials (**Chapter 4**), this presented work is particularly focused on the organic iodides adsorption on Ag⁰-Aerogel, which contains multiple difficulties. Unlike the I₂ adsorption, the reactions between organic iodides and Ag would be more complex. For CH₃I and Ag, Scheele et al.⁶⁸ proposed the reactions as,





where the CH₃I react with Ag and forms gas phase C₂H₆ (ethane). With H₂O presented, CH₃OCH₃ (dimethyl ether) and CH₃OH (methanol) may be generated. These organic products were observed by Soelberg and Watson,⁸⁹ the scission of C-I bond was proposed by Jenks et al.¹³⁸ and the formation of C₂H₆ in similar reactions was suggested by Zhou et al.¹³⁹. With the presence of NO_x in the gas stream, other organic compounds such as CH₃NO₂ (nitromethane) and C₃H₉NO (3-amino-1-propanol) were also detected.⁹⁰

The iodoalkanes used in the experiments range from CH₃I to C₁₂H₂₅I (iodododecane). As the length of alkyl group increased, the compounds become more unstable. The cleavages of C-C bonds in organic iodides on metal surface were reported by Tjrandra and Zaera¹⁴⁰ and Yamauchi et al;¹⁴¹ and the dehydrogenation was also observed in previous experiments.^{142,143} These studies indicate that the products of the iodoalkane-Ag reactions may not be limited to the alkanes with the length doubled (e.g. C₂H₆ as for CH₃I-Ag reaction) and with the increasing length of alkyl group, the complexity of the reactions may increase exponentially.

The second difficulty is the concentrations of iodoalkanes. Unlike the ppmv level concentrations in previous single-layer adsorption studies,^{15,92} the concentrations selected are down to tens or hundreds of ppbv level. At such concentrations, measuring the mass uptakes was highly challenging. To obtain reliable data, the pellets were dried carefully before the adsorption, or the mass change due to moisture equilibrium will impact the results significantly. Moreover, since no permeation tubes with higher organic iodides concentration are available, determining the

maximum organic iodides adsorption capacities may be impracticable. Therefore, by assuming the capacities of organic iodides adsorptions and I₂ adsorption are similar, the uptake capacities used in modeling works are estimated by the 50 ppmv I₂ adsorption at 150 °C.

Additionally, the Ag⁰-Aerogel is a highly heterogeneous material. The shape, size and silver coverage are uneven, which implies that the actual properties of Ag⁰-Aerogel used in experiments may vary slightly. Additionally, Bruffey et al.⁹⁹ suggested that Ag⁰-Aerogel may crack during the adsorptions, large particles break down to smaller particles, which results in the decrease of average pellet size during the experiments.

To avoid the influences of the variations of properties between experiments, the adsorption kinetics were collected and reported on following bases,

1. If the adsorption kinetics collected were questionable or the trends did not agree with the expectations, the experiments were repeated at least once (or twice if the kinetics are critical for making conclusions).
2. In the repeats (including the first trial), if a kinetics is highly unlikely to be reasonable (comparing with literature works and the trends observed in previous experiments performed), the kinetics was excluded from the data analyses.
3. In two repeats, if the kinetics were similar, only one of the results was reported. If the two kinetics were not agreed, a third repeat was performed.
4. In three repeats, if two of the kinetics were similar, both two results were reported. If three repeats were not agreed, the kinetics with moderate uptake rate was reported.

Chapter 4. Material Comparison: Ag⁰-Aerogel, Ag⁰Z and AgA

4.1 AgA Manufacturing

Silver nitrate impregnated alumina spheres were manufactured following the procedure suggested by Jordan and Jubin.¹¹⁹ 100 g of alumina spheres (Sorbent Technologies, activated alumina spheres, 7×14 Tyler mesh, 2mm) were mixed with the solution of 25 g of AgNO₃ (silver nitrate, Sigma-Aldrich) in 76 ml DI water. The mixture was then transferred to a rotary evaporator (Büchi Rotavapor R-114) and dried under vacuum at 125 °C using an oil bath (Büchi Heating Bath B-491). After 9 hours, the dried samples were transferred to plastic sample vials and stored under vacuum.

The nitrogen titration analyses were performed using both the alumina spheres and AgA. The results showed that no micropores exist in both samples, the BET surface area of the sample decreased from 300.8 m²/g to 254.6 m²/g during the treatment and the BJH pore volume decreased from 0.454 cm³/g to 0.450 cm³/g.

Assuming the mass of the alumina sphere remained constant, the procedure-based silver composition can be calculated to be approximately 13.7 wt%. The sample composition was scanned using XPS and SEM-EDX and the results are shown in Table 4-1. N is not determined in either spectrum; the Ag composition ranges from 20 wt% to 25 wt%. Additionally, 50 ppmv I₂ adsorption on AgA at 150 °C was also performed using the continuous flow adsorption system and the maximum I₂ capacity is approximately 11.2 wt%. Assuming the silver is fully consumed and the molar ratio is 1, the adsorption-based Ag composition is approximately 9.5 wt%.

Method	C (wt%)	O (wt%)	Al (wt%)	Ag (wt%)
XPS	3.69	34.05	41.50	20.76
SEM-EDX	2.31	37.87	34.50	25.32

Table 4-1. Composition of AgA measured by XPS and SEM-EDX.

4.2 Adsorption Kinetics and Modeling Results

To compare the effectiveness of Ag⁰-Aerogel, Ag⁰Z and AgA in organic iodides removal, the 104 and 1044 ppbv CH₃I adsorptions at 150 °C were performed using the continuous flow adsorption system and the results are plotted in Figure 4-1.

In the 1044 ppbv adsorption, the AgA obtained the slowest uptake rate among three materials, only approximately 1/5 of Ag⁰-Aerogel and Ag⁰Z. As for the 104 ppbv adsorption, no significant mass uptake on AgA was measured in approximately 12 days. It is important to notice that no significant mass uptake measured does not necessarily imply no CH₃I adsorbed, instead, a trace amount of I was observed in the XPS analysis.

In the CH₃I adsorptions on Ag⁰Z at both concentrations, significant mass increases were observed in the first day. The uptake mass in the first 5 hours exceeded 0.5 wt% and approximately 0.8 wt% of CH₃I was adsorbed in 24 hours. Similarly, the significant mass decreases were also observed after the adsorption stopped and the desorption started; in 5 hours, approximately 0.3 wt% of adsorbed CH₃I desorbed from the Ag⁰Z, which indicated that the physisorption of CH₃I on Ag⁰Z is much more significant than that on Ag⁰-Aerogel. Using the adsorption column, it is impracticable to observe such behavior since the mass gain cannot be

measured continuously.³⁷ Neither in the 50 ppmv I₂ single layer adsorption¹⁵; the chemisorption of I₂ is much more rapid than the physisorption and therefore covered the physisorption region. Excluding the physisorption uptake, in 104 ppbv adsorptions, Ag⁰-Aerogel and Ag⁰Z reached 0.42 and 0.62 wt% respectively and in the 1044 ppbv adsorption, Ag⁰-Aerogel, Ag⁰Z and AgA reached 3.71, 2.90 and 0.75 wt%.

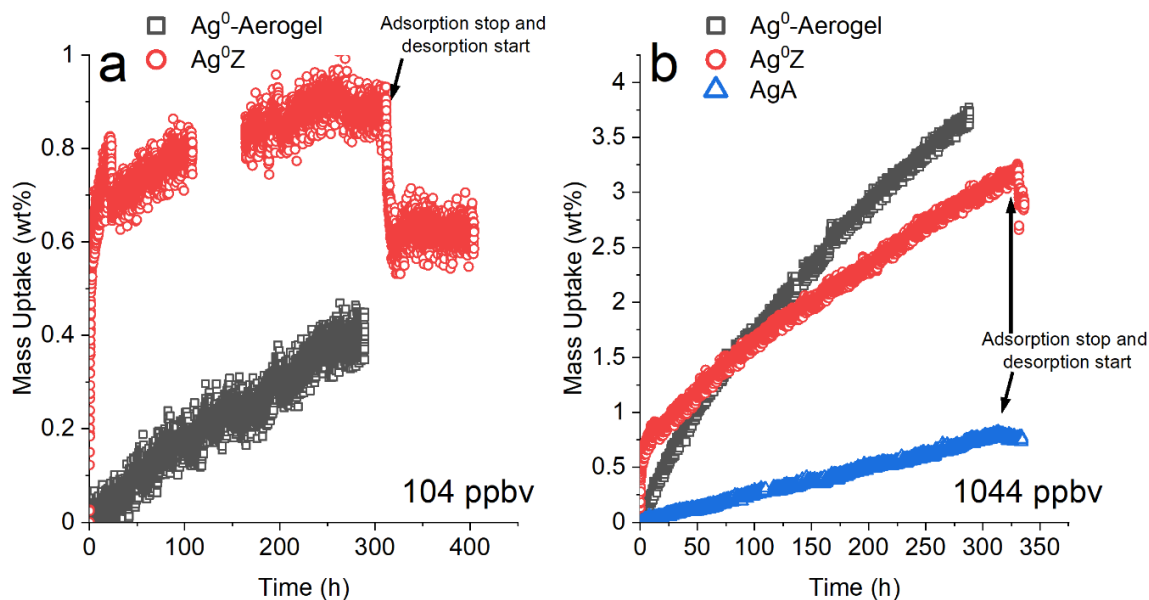


Figure 4-1. Adsorption kinetics of 104 (a) and 1044 (b) ppbv CH₃I adsorptions on Ag⁰-Aerogel, Ag⁰Z and AgA at 150 °C (No significant mass uptake on AgA observed at 104 ppbv).

Considering the chemisorption region, the reaction rate constants and the pore diffusivities can be determined using the shrinking core model and the results are listed in Table 4-2. The diffusivities were not determined at 104 ppbv concentrations because the mass uptakes were too

low to enable any diffusion process to be revealed. The Ag⁰-Aerogel obtains the highest average uptake rate, approximately 50% higher than that of Ag⁰Z. However, due to the variations in the maximum iodide loading capacities and the silver contents, the reaction rate constants of Ag⁰-Aerogel are actually lower than those of Ag⁰Z.

Concentration (ppbv)	Material	Max Capacity (wt%)	Avg Uptake Rate (wt%/h)	k_f (cm/s)	D_p (cm ² /s)	k_s (cm/s)	AARD (%)
104	Ag ⁰ -Aerogel	37.2	1.45×10 ⁻³	2.71*	N.D**	0.23	14.74%
	Ag ⁰ Z	12.8	9.90×10 ⁻⁴	2.97*	N.D**	0.60	48.01%
	AgA***	11.2	NA	NA	NA	NA	NA
1044	Ag ⁰ -Aerogel	37.2	1.42×10 ⁻²	2.71*	7.07×10 ⁻⁴	0.40	1.87%
	Ag ⁰ Z	12.8	8.02×10 ⁻³	2.97*	2.42×10 ⁻³	0.58	1.59%
	AgA	11.2	2.50×10 ⁻³	2.71*	6.68×10 ⁻⁴	0.06	5.50%

*Calculated theoretically

**Not determined.

***No significant mass uptake measured

Table 4-2. The model fitting parameters and results for 104 and 1044 ppbv CH₃I adsorption on Ag⁰-Aerogel, Ag⁰Z and AgA.

4.3 Physical Analyses Results

The Ag and I compositions were measured using XPS and SEM-EDX and the results are listed in Table 4-3. To compare the compositions of the samples with different iodide uptake, the weight

percent of Ag and I was calibrated as,

$$\text{Calibrated.wt\%} = \frac{\text{measured.wt\%}}{(1 - \text{Iodine\%})} \quad 4-1$$

which means the iodide was considered as additional mass.

Material	Conc' (ppbv)	XPS			SEM-EDX			Iodine Uptake* (wt%)
		Ag (wt%)	I (wt%)	I:Ag (%)	Ag (wt%)	I (wt%)	I:Ag (%)	
Ag ⁰ Z	Fresh	8.84						
	104	8.94	4.10	46%	18.47	1.86	10%	0.62
	1044	10.78	9.22	86%	14.12	10.17	72%	2.90
AgA	Fresh	20.76			25.32			
	104	19.53	0.21	1%	24.57	0.11	0.4%	NA**
	1044	21.39	1.89	9%	29.36	3.40	12%	0.75
Ag ⁰ -Aerogel	Fresh	33.7			31.5			
	104	28.0	2.5	9%	38.5	1.2	3%	0.42
	1044	27.8	12.4	45%	34.3	5.0	15%	3.71

*Chemisorption iodine uptake

**No significant mass uptake measured

Table 4-3. The Ag and I compositions of Ag⁰-Aerogel, Ag⁰Z and AgA measured by XPS and SEM-EDX.

The iodine compositions determined in Table 4-3 are roughly comparable with the iodine uptakes measured experimentally. Both the modeling and the physical analyses results indicate that the AgA obtains the lowest efficiency in iodine removal and the chemisorption rate of Ag⁰-Aerogel is greater than that of Ag⁰Z.

4.4 Aging Resistance

Besides the adsorption rate, the aging resistance is another critical factor to be considered in comparing the efficiency for iodide removal. In the off-gas streams, a considerable amount of NO_x exists and induces the losses of adsorption capacities of the adsorbents by oxidizing the silver contained.^{65,98} In the study conducted by Choi et al.,¹⁰⁵ the NO_2 was identified as the species that obtains the highest aging effect to Ag^0Z and Ag^0 -Aerogel among dry air, moist air, NO , and NO_2 . When contacting with NO_2 at $150\text{ }^\circ\text{C}$, Ag^0Z loses more than 90% of its original iodine capacity in the first week and at 1 month, the capacity is close to zero.^{84,85}

AgA obtains stronger resistance to NO_2 aging but the capacity loss is still considerable. Jordan observed 76% loss in 1-month NO_2 aging experiments and the remaining capacity is approximately 2.4 wt%.⁸⁴ The NO_2 aging resistance is similar for Ag^0 -Aerogel (80% loss of capacity in 1 month). However, since the initial adsorption capacity is much higher, Ag^0 -Aerogel maintains approximately 6 wt% of capacity.

These literature works suggest that for its high silver content and special structures, the Ag^0 -Aerogel obtains the highest aging resistance among the three materials.

4.5 Conclusions

When determining the optimal adsorption temperature, Nan et al.⁹⁵ reported $150\text{ }^\circ\text{C}$ at which the highest adsorption capacity was observed. However, the criterion changes for the ppbv level adsorption. To be discussed in **Chapter 5**, reaching the maximum capacities of the adsorbents is

not applicable. For example, based on the model predictions, the adsorption process on Ag⁰-Aerogel may last for decades at 104 ppbv. Therefore, it is not necessary to consider the capacities in determining the efficiencies of the materials. Instead, the uptake rate becomes more important. With the adsorbent of higher uptake rate, the adsorption column may be shortened with no impact on the designated removal ratio.

Moreover, the aging resistance is another crucial factor to be considered. Discussed in the previous section, Ag⁰-Aerogel maintains the highest adsorption capacity of 8 wt% after contacting with NO₂ at 150 °C for one month, whereas Ag⁰Z lost all the capacity and AgA remains 2-3 wt%.

Therefore, since the Ag⁰-Aerogel obtains the highest iodine uptake rate, adsorption capacity and aging resistance, Ag⁰-Aerogel is considered as the optimal material among the three materials.

However, there are multiple factors not considered. Ag⁰-Aerogel is a novel material developed in the 2010s, whereas the Ag⁰Z and AgA were developed decades ago and have been used around the world. The techniques of maintaining and operating the Ag⁰Z and AgA adsorption are well-developed. In other words, to replace with Ag⁰-Aerogel, the adsorption system may need to be altered and additional training may be required. These additional procedures increase the capital cost and may obstruct the application of Ag⁰-Aerogel.

Secondly, the understanding of Ag⁰-Aerogel is still limited. The adsorption kinetics, iodine capacities and the aging effects were investigated but the results are still not adequate to provide a comprehensive overview of the material. To employ the Ag⁰-Aerogel in the industrial waste

reprocessing system, more application-oriented studies are required.

Chapter 5. CH₃I Adsorption on Ag⁰-Aerogel: Concentration Dependence

5.1 Introduction

The Ag⁰-Aerogel was selected as the most effective material among Ag⁰-Aerogel, Ag⁰Z and AgA for its high CH₃I adsorption rate and aging resistance. To further examine the adsorption behaviors and provide parameters for column modeling and design, the single-layer CH₃I adsorptions at various concentrations were conducted to understand the concentration dependence of the adsorption.

In the single-layer adsorption experiments, Ag⁰-Aerogel was placed in a tray connected to a microbalance, enabling real-time and high-precision measurement of the mass change. The temperature was 150 °C and gas flow rate was set to be 500 sccm in order to satisfy the 1.1 m/s superficial gas velocity suggested by Nan et al.⁹⁵ To provide an overview of the CH₃I adsorption, two long term adsorptions were performed at 245 and 9584 ppbv concentrations. The results indicated that reaching adsorption saturations is unrealistic for concentrations under approximately 1 ppmv, therefore, the 104 and 1044 ppbv CH₃I adsorptions were stopped at about 12 days (approximately 300h).

The adsorption kinetic data at various CH₃I concentrations were obtained and used to evaluate the models and determining pore diffusivity and reaction rate of CH₃I in Ag⁰-Aerogel. To explain the inconsistency of reaction rate constants at different concentrations, an nth order shrinking core model was applied and the modeling results were used to improve the predictions of adsorption

behavior at various CH₃I concentrations.

5.2 Adsorption Kinetics

Four adsorption experiments with 104, 245, 1044 and 9584 ppbv CH₃I in dry air were conducted.

The concentrations were calculated from the data provided by the permeation tube manufacturer and confirmed by measuring the mass differences of the permeation tubes before and after the experiments. Approximately 288 hours adsorption data of 104, 245, 1044 and 9584 ppbv CH₃I adsorption on Ag⁰-Aerogel are plotted in Figure 5-1. At 288 hours, mass uptakes reached 0.39, 0.91, 3.7 and 14.7 wt% at 104, 245, 1044 and 9584 ppbv respectively; and the long-term adsorptions at 245 and 9854 ppbv reached 4.1 and 28.5 wt% (The full adsorption kinetics are plotted in Figure 5-2). To eliminate the physically adsorbed CH₃I, the Ag⁰-Aerogel was left in the adsorption column and desorbed by stopping CH₃I generation and flowing only dry air for 24-48 h. During this desorption process, no significant mass losses were observed, indicating CH₃I adsorption on Ag⁰-Aerogel was mostly chemisorption.

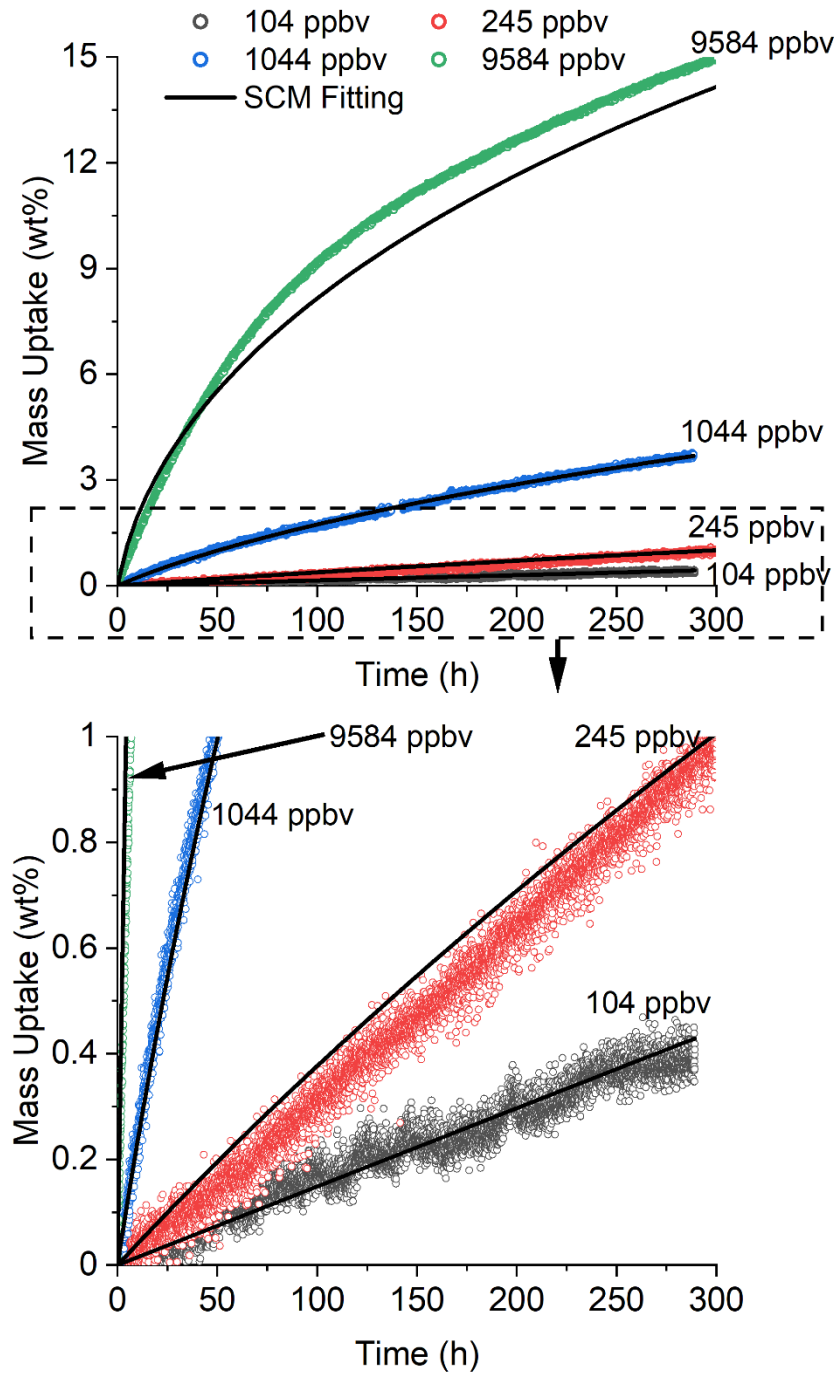
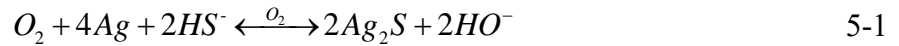


Figure 5-1. Uptake curves of 104, 245, 1044 and 9584 ppbv CH₃I adsorptions on Ag⁰-Aerogel for up to 288 hours.

5.3 Considering the Aging Effect

When being heated in air, Ag⁰-Aerogel tends to lose its adsorption capacity and this aging phenomenon becomes significant when the exposure time is long enough. Reported by Matyáš et al.⁶⁵ Ag⁰-Aerogel loses 21.5% of its original capacity when being aged in 150 °C dry air for 6 months and Choi et al.¹⁰⁵ observed a 19.7% loss in 1 month. The long term CH₃I adsorptions at 245 and 9854 ppbv reached 4.1 and 28.5 wt%, which provide an excellent opportunity for examining the aging effect during iodine removal.

Choi et al.¹⁰⁵ proposed the dry air aging mechanism of Ag⁰-Aerogel to be,



The silver sites are deactivated by reacting with thiol groups (HS⁻) with air present and the rate can be written as,

$$\frac{d\bar{C}_{Ag}}{dt} = -k_1^* \bar{C}_{HS^-} \bar{C}_{Ag} + k_{-1} \bar{C}_{S^-} \bar{C}_{Ag^+} \quad 5-2$$

where,

$$k_1^* = k_1 \bar{C}_{O_2} \quad 5-3$$

k_1 and k_{-1} are the forward and reverse reaction rate constants and \bar{C} 's are the dimensionless concentration.

The material balance of Ag and S can be represented as,

$$1 - \bar{C}_{HS^-} = \bar{C}_{S^-} \quad 5-4$$

$$\bar{C}_{S^-} = 2\bar{C}_{Ag^+} \quad 5-5$$

$$\bar{C}_{Ag^+} = 1 - \bar{C}_{Ag} \quad 5-6$$

Therefore, Eq. 5-2 can be written in k 's and \bar{C}_{Ag} as,

$$\frac{d\bar{C}_{Ag}}{dt} = -k_1^* \bar{C}_{Ag} (2\bar{C}_{Ag} - 1) + k_{-1} (\bar{C}_{Ag} - 1)(2\bar{C}_{Ag} - 2) \quad 5-7$$

with the initial condition as,

$$\bar{C}_{Ag} \Big|_{t=0} = 1 \quad 5-8$$

and $k_1^* = 1.3 \times 10^{-4} \text{ hr}^{-1}$ and $k_{-1} = 1.3 \times 10^{-3} \text{ hr}^{-1}$.¹⁰⁵

Assuming the deactivation of Ag sites is homogeneous through the pellet, the aging effect can be incorporated into the adsorption model and the q_e (saturation sorbate concentration) used for modeling may be replaced with a time-dependent $q_e(t)$ as,

$$q_e(t) = q_e \bar{C}_{Ag}(t) \quad 5-9$$

The model fitting results using the shrinking core model (SCM), volume reaction model (VRM), linear driving force model (LDFM) and the micropore term of the pore diffusion model (PDMI) of the 245 and 9584 ppbv CH_3I adsorption on Ag^0 -Aerogel with fixed $q_e = 37 \text{ wt}\%$ and the aging effect-incorporated, time-dependent $q_e(t)$ are plotted in Figure 5-2 and the parameters determined are listed in Table 5-1.

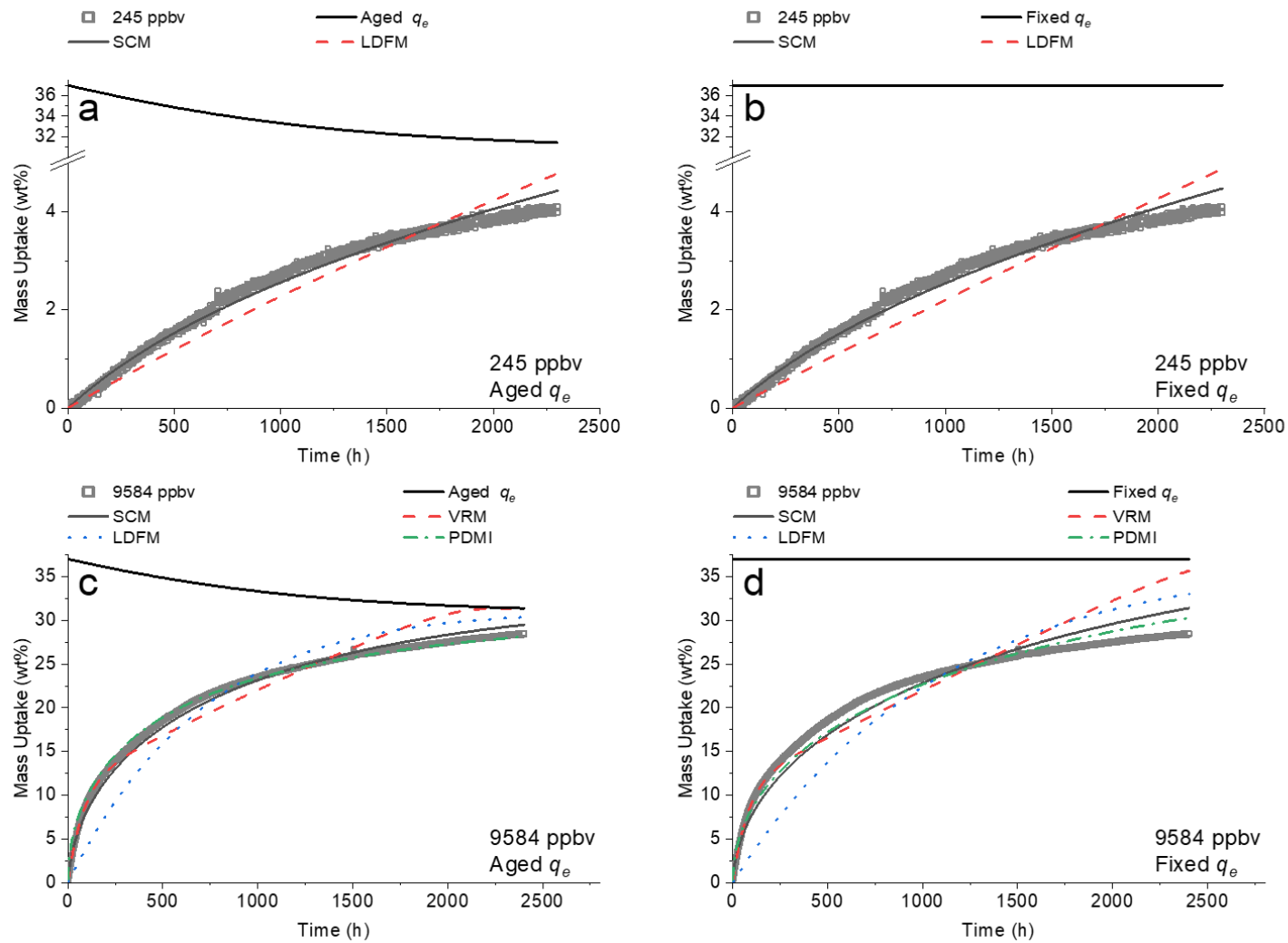


Figure 5-2. Model fitting results using SCM, VRM, LDFM and PDMI of the 245 and 9584 ppbv CH_3I adsorption on Ag^0 -Aerogel

with fixed $q_e = 37 \text{ wt}\%$ and the aging effect-incorporated, time-dependent $q_e(t)$.

Concentration (ppbv)	SCM				VRM				LDFM		PDMI	
	k_f (cm/s)	D_p (cm ² /s)	k_s (cm/s)	AARD (%)	k_v (cm ³ /mol/s)	D_p (cm ² /s)	ϕ^2	AARD (%)	k_{LDF} (s ⁻¹)	AARD (%)	D_i (cm ² /s)	AARD (%)
245 (Fixed q_e)	2.71*	4.95×10 ⁻⁴	0.28	2.48	7.77×10 ³	NA**	NA**	NA**	1.71×10 ⁻⁸	17.56%	NA**	NA**
245 (Aged q_e)	2.71*	5.86×10 ⁻⁴	0.27	1.62	1.00×10 ⁴	NA**	NA**	NA**	1.87×10 ⁻⁸	14.91%	NA**	NA**
9584 (Fixed q_e)	2.71*	5.65×10 ⁻⁴	0.88	2.59	1.29×10 ⁴	7.18×10 ⁻⁴	303.8	3.98	2.58×10 ⁻⁷	6.60%	6.21×10 ⁻²³	5.74%
9584 (Aged q_e)	2.71*	7.16×10 ⁻⁴	0.62	1.29	1.26×10 ⁴	8.98×10 ⁻⁴	236.9	2.93	3.27×10 ⁻⁷	4.62%	9.05×10 ⁻²³	5.09%

*Determined theoretically using Eq. 3-11 to 3-14.

**No reasonable fitting results could be determined.

Table 5-1. The parameters determined using SCM, VRM, LDFM and PDMI with fixed q_e and aging-incorporated q_e .

To average the weights of different sections in the adsorption curves and increase the accuracy of data fitting, the variables to be fitted were rescaled by \log_{10} before applying the least square regressions. More specifically,

$$\min_{para1, para2...} \sum_i \left(\log_{10} \left(f(para1, para2...) \right)_i - \log_{10} (data_{exp})_i \right)^2 \quad 5-10$$

was used instead of,

$$\min_{para1, para2...} \sum_i \left(f(para1, para2...) - (data_{exp})_i \right)^2 \quad 5-11$$

where f is the equation of the model to be fitted, $para1, para2...$ are the parameters in the model, subscript i is the number of experimental data and $data_{exp}$ is the experimental data.

Eq. 5-11 is a typical method of performing model fitting, and another method is,

$$\min_{para1, para2...} \sum_i \left(\frac{f(para1, para2...) - (data_{exp})_i}{(data_{exp})_i} \right)^2 \quad 5-12$$

In these two methods, the weights of the values are highly uneven. For example, in Eq. 5-11, the model tends to focus on the data with greater values since a relative error for the data with smaller value contribute much less absolute error than that with a greater value. Similarly, when using the method in Eq. 5-12, the model tends to focus on the data with smaller values because relative error for a small value data may be magnified significantly by the denominator. The effect of uneven weights of the data becomes significant especially for the data with a wide range; e.g., for the SCM, t is fitted and the range is from 1 up to 10^6 second. Therefore, to narrow-down the range and even the weights of the values, the method shown in Eq. 5-10 was applied.

The *AARD*'s (average absolute relative deviation) were calculated using,

$$AARD = \frac{1}{N} \sum_i^N \left| \frac{q_i^{exp} - q_i^{model}}{q_i^{exp}} \right| \times 100 \quad 5-13$$

where *model* indicates model fitting result and *N* is the number of data points.

Since the a near-saturation was achieved in 9584 ppbv adsorption, the process can be fitted by all four models and the *AARD*'s are relatively low. However, limited by the low mass uptake, no reasonable results can be determined for the 245 ppbv adsorption using VRM and PDMI. (Four models will be compared in the next section.)

Incorporating the aging effect enabled better model fitting results since the *AARD*'s in Table 5-1 decreased. Additionally, visualized in Figure 5-2, the 9584 ppbv adsorption was approaching the saturation and the maximum capacity may be located at approximately 30-31wt%, 19% lower than the fresh capacity, which is close to the aged capacity reported by Matyáš et al.⁶⁵ and Choi et al.¹⁰⁵

To further understand the aging effect during CH₃I adsorption, some estimations were made based on the aging model proposed. When the aging time exceeds approximately 170 days, the adsorption capacity equilibrates at about 30.8 wt%. Additionally, the aging effect may only be significant when the adsorption time is long enough, (months or longer) and in 12 days (the time selected for other adsorption experiments), the adsorption capacity decreased form 37 wt% to 35.7 wt%, which may not impact the adsorption parameters determined. To maintain the consistency of model fitting processes, the aging effect was always incorporated in the model for

the rest of presented work unless specified particularly.

5.4 Model Fitting Results and Model Comparison

To analyze the kinetic data collected for 104, 245, 1044 and 9584 ppbv CH₃I adsorption on Ag⁰-Aerogel at 150 °C, the shrinking core model (SCM), volume reaction model (VRM), linear driving force model (LDFM) and the micropore term of the pore diffusion model (PDMI) were applied and a comparison of the four models was made. Figure 5-3 shows the adsorption kinetics and model fitting results and the parameters determined are listed in Table 5-2. k_f in the SCM was calculated theoretically using Eq. 3-11 to 3-14. The value was 2.71 cm/s, which is comparable with what Jubin calculated under similar conditions.⁹² For 104, 245 and 1044 ppbv adsorption, no reasonable parameters could be determined using PDMI and the diffusivities in VRM are not reasonable either. Additionally, the LDFM results are not reliable for 104, 245 and 1044 ppbv adsorption.

The 9584 ppbv adsorption can be described by all four models, and the parameters determined by LDFM and PDMI agree well. When the micropore diffusion is the controlling term for LDFM, the Eq. 3-20 reduces to,¹²⁵

$$\frac{1}{k_{LDF}} = \frac{\bar{R}_i^2}{15D_i} \quad 5-14$$

For Ag⁰-Aerogel, the micropore diameter is 6.6 Å, and the D_i can be estimated using Eq. 5-14 to be 9.51×10^{-23} cm²/s.

By applying the SCM, D_p 's were determined to be 5.86×10^{-4} , 7.07×10^{-4} and 7.16×10^{-4} cm²/s for

245, 1044 and 9584 ppbv respectively, and the D_p was not determined using the SCM at 104 ppbv adsorption since no significant diffusion process was observed. More specifically, at low concentration, the CH_3I has not consumed all Ag on the surface of Ag^0 -Aerogel pellet during the test time frame and therefore no significant pore diffusion was observed. The average D_p by SCM was $6.70 \pm 0.73 \times 10^{-4} \text{ cm}^2/\text{s}$ and the value of $8.98 \times 10^{-4} \text{ cm}^2/\text{s}$ determined using VRM at 9584 ppbv concentration is also comparable.

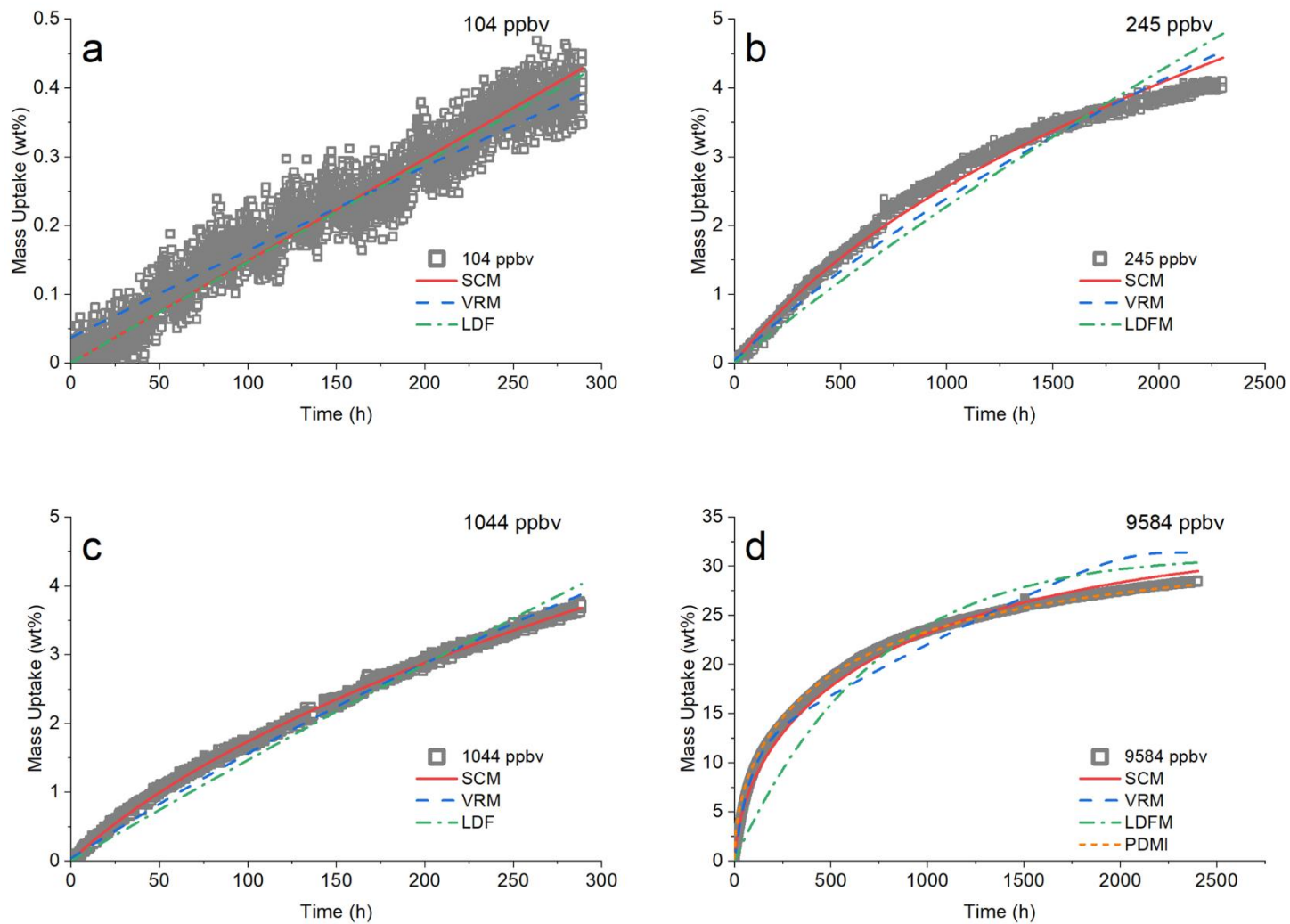


Figure 5-3. The adsorption kinetics and model fitting results of 104, 245, 1044 and 9584 ppbv CH_3I adsorption on Ag^0 -Aerogel.

Concentration (ppbv)	SCM				VRM				LDFM		PDMI	
	k_f (cm/s)	D_p (cm ² /s)	k_s (cm/s)	AARD (%)	k_v (cm ³ /mol/s)	D_p (cm ² /s)	ϕ^2	AARD (%)	k_{LDF} (s ⁻¹)	AARD (%)	D_i (cm ² /s)	AARD (%)
104	2.71*	N.D**	0.23	14.74	9.96×10 ³	N.D**	N.D**	N.D**	1.11×10 ⁻⁸	14.52	N.D**	N.D**
245	2.71*	5.86×10 ⁻⁴	0.27	1.62	1.00×10 ⁴	N.D**	N.D**	N.D**	1.87×10 ⁻⁸	14.91	N.D**	N.D**
1044	2.71*	7.07×10 ⁻⁴	0.40	1.87	1.28×10 ⁴	N.D**	N.D**	N.D**	1.13×10 ⁻⁷	12.61	N.D**	N.D**
9584	2.71*	7.16×10 ⁻⁴	0.62	1.29	1.26×10 ⁴	8.98×10 ⁻⁴	236.9	2.93	3.27×10 ⁻⁷	4.62	9.05×10 ⁻²³	5.09

*Determined theoretically using Eq. 3-11 to 3-14.

**No reasonable fitting results could be determined.

Table 5-2. The parameters determined for 104, 245, 1044 and 9584 ppbv CH₃I adsorption on Ag⁰-Aerogel.

The pore diffusion model has been used in the CH₃I and water adsorption on Ag⁰Z by Jubin⁹² and Nan¹⁵; the D_a and D_i determined agreed well in their experiments and the errors are acceptable. In the 9585 ppbv adsorption, the mass uptake reached 28.5 wt%. Adequate amount of CH₃I diffused into the pellet and the overall process is mainly diffusion controlled (To be discussed in **Section 5.7**). Therefore, the process can be described by the pore diffusion model and the micropore diffusivity D_i was calculated to be 9.05×10^{-23} cm²/s. However, the pore diffusion model is not applicable for ‘partial adsorptions’. For 104, 245 and 1044 ppbv CH₃I adsorption, the highest mass uptake achieved was approximately 4 wt%, less than 1/9 of the full capacity. In such case, only limited amount of diffusion exists and the adsorptions are mainly controlled by reaction. Similarly, the reactions are not included in the linear driving force model, and the results determined are not reliable either. Therefore, since the pore diffusion model and linear driving force model do not consider the reaction between organic iodides and Ag⁰-Aerogel, the PDM and LDFM are not suitable for the ‘partial adsorptions’ of organic iodides on Ag⁰-Aerogel.

Unlike the PDM and LDFM, the VRM considers both the reaction and diffusion processes in the adsorption but the results are not ideal either. For the ‘partial adsorption’ at 104, 245 and 1044 ppbv, only the reaction rates were interpreted using the VRM and the D_p ’s were not determined. For the same reason discussed above, the diffusivities may not be reliable when the diffusion process in the adsorption is not significant enough, and the threshold of determining a reliable D_p for VRM may be higher than that of SCM. Additionally, since the natural logarithm was required

when applying the VRM (Eq. 3-16), results with imaginary numbers may exist in certain circumstances, which introduces additional difficulties in the model fitting process.

Additionally, a shrinking core process was observed by cutting a partial reacted Ag^0 -Aerogel pellet. In the CH_3I adsorption, the color of Ag^0 -Aerogel changed from black to pale yellow and therefore enabled observing the adsorption process in another perspective. By cutting a I_2 partial reacted Ag^0Z pellet in half, Nan¹⁵ observed a clear edge between the reacted and unreacted layer and concluded that the adsorption of I_2 on Ag^0Z is a shrinking core process. Similarly, the CH_3I partial adsorbed Ag^0 -Aerogel was cut in half and a dark unreacted core with yellow reacted layer was observed (Figure 5-4), therefore, the adsorption of CH_3I in Ag^0 -Aerogel is likely to be the shrinking core process.

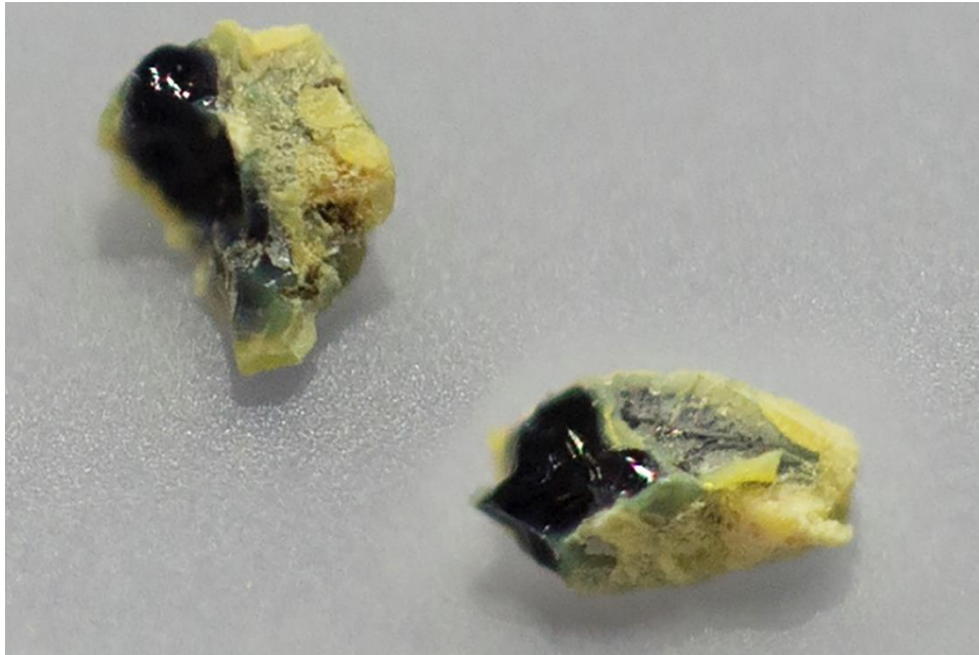


Figure 5-4. Shrinking core process observed in CH_3I adsorption on Ag^0 -Aerogel, two cut halves of a partially reacted pellet.

Based on the explanation above, the shrinking core model is considered as the most suitable model among SCM, VRM, LDFM and PDMI for its accuracy, straight-forward physical implication and easy applying.

Using the SCM, an average D_p was calculated and it can be used for further applying the SCM to predict the adsorption behavior in a wider concentration range. However, different from 3 similar D_p 's, k_s 's increase from 0.23 cm/s at 104 ppbv to 0.62 cm/s at 9584 ppbv. The concentration-dependent k_s is highly questionable. Theoretically, for a given reaction, the reaction rate constant only depends on temperature and shall not change with the reactant concentration.¹⁴⁴ Therefore, the orderly changed k_s indicates an n^{th} order reaction instead of the assumed 1st order.

5.5 N^{th} Order Shrinking Core Model

The n^{th} order SCM cannot be used directly to fit an adsorption curve because the $k_s^* C_b^n$ term in Eq. 3-10 contains two variables (k_s^* and n) and one constant (C_b). There exists an unlimited amount of combinations to yield the desired value. Instead, k_s^* and n were determined by plotting k_s (cm/s) and C_b (mol/cm³) using Eq. 5-15 and 5-16.

$$k_s C_b = k_s^* C_b^n \quad 5-15$$

$$\ln(k_s C_b) = \ln(k_s^*) + n \ln(C_b) \quad 5-16$$

The reaction order and n^{th} order reaction constant were determined using Figure 5-5 and shown in Table 5-3. For CH₃I-Ag⁰-Aerogel adsorption system, $n=1.22$ and $k_s^*=74.90$

(cm/s)·(mol/cm³)¹⁻ⁿ. As mentioned earlier, the SCM results can be applied to deep-bed adsorption

analysis. However, keeping the n^{th} order reaction assumption may introduce certain difficulties in calculations. Therefore, Eq. 5-15 can be rewritten as Eq. 5-17 to calculate the n^{th} -order-compensated, concentration-dependent *pseudo* k_s 's (cm/s).

$$\text{pseudo } k_s = k_s^* C_b^{n-1} \quad 5-17$$

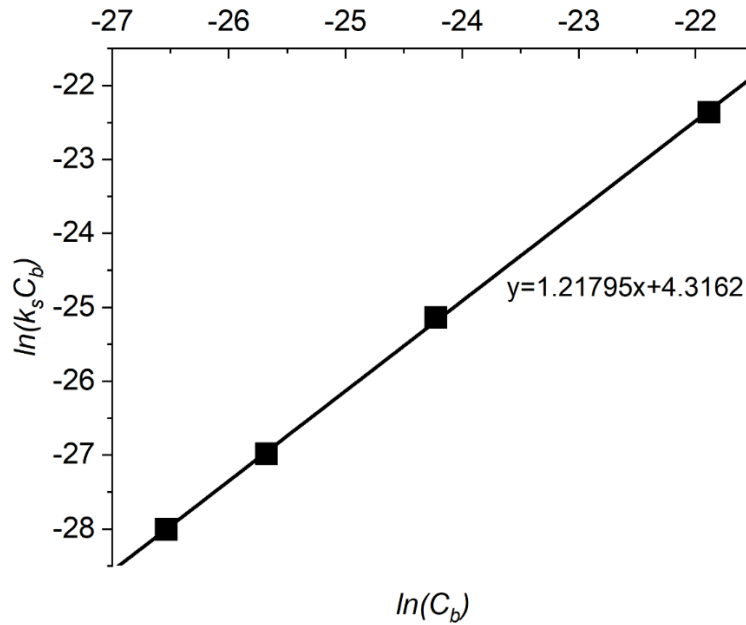


Figure 5-5. Reaction order plot, $\ln(C_b)$ vs. $\ln(k_s C_b)$.

Concentration (ppbv)	k_s (cm/s)	$\ln(k_s C_b)$	$\ln(C_b)$	<i>pseudo</i> k_s (cm/s)
104	0.23	-26.54	-28.01	0.23
245	0.27	-25.68	-26.98	0.28
1044	0.40	-24.23	-25.14	0.38
9584	0.62	-21.88	-22.36	0.64

$$n=1.22$$

$$k_s^* = 74.90 \text{ (cm/s)} \cdot (\text{mol/cm}^3)^{1-n}$$

Table 5-3. Parameters and results of determining reaction order.

Similar fractional reaction orders were also observed in other silver-containing materials. Zhou and White¹⁴⁵ suggested that the desorption of organic products from Ag(111) surface changes the order of the C₂H₅I-Ag reaction. Robb and Harriott¹⁴⁶ indicated that the diffusion limitation in supported silver catalysts changes the order of CH₃OH oxidation. Both researchers point out the effect of the physical process, the diffusion of product, to the order of chemical reaction, which will be discussed in **Section 5.8**.

5.6 Nth Order SCM Examination and Application

The effectiveness of the nth order SCM can be demonstrated by comparing predictions made by the nth order SCM and 1st order SCM with *average* k_s , which the *average* $k_s = 0.381$ cm/s was calculated by averaging 4 k_s 's directly. Figure 5-6 shows the prediction of 104 ppbv CH₃I adsorption behavior generated by using nth order SCM and 1st order SCM with *average* k_s , and the D_p used is the average value determined. Comparing with 1st order SCM with *average* k_s , the nth order SCM decreases AARD by approximately 35%. The mass uptakes in 288 hours predicted by using nth order SCM and 1st order SCM with *average* k_s are 0.40 wt% and 0.59 wt% respectively, where the measured mass uptake is approximately 0.39 wt%.

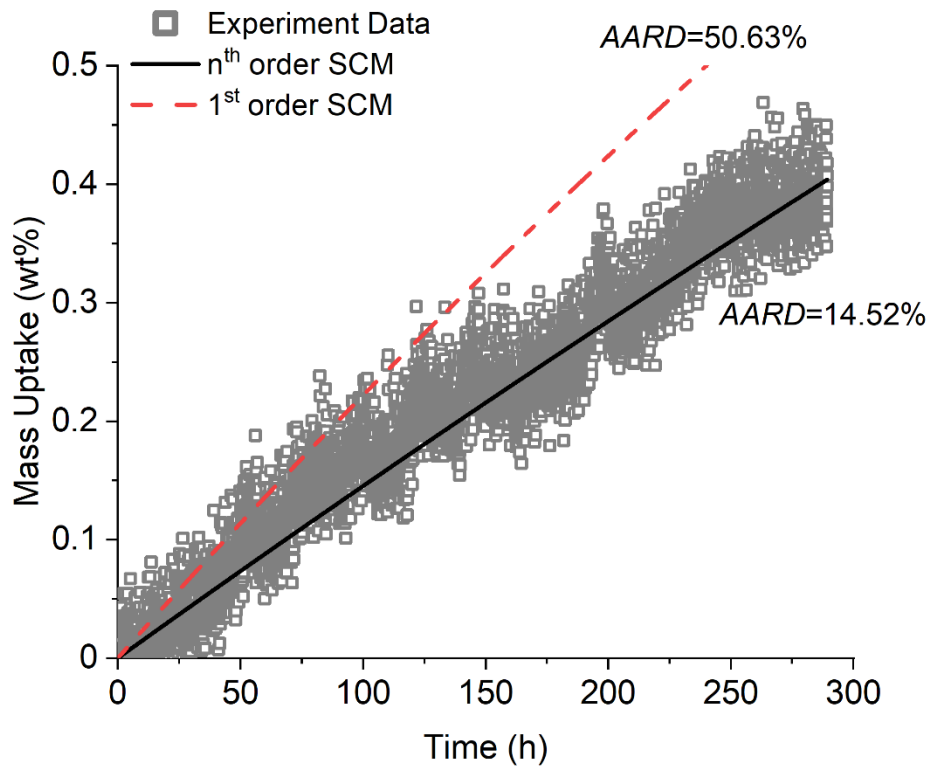


Figure 5-6. 104 ppbv CH₃I on Ag⁰-Aerogel, SCM prediction using nth order SCM and 1st order SCM with *average* k_s .

With the developed nth order SCM, the adsorption behavior can be predicted more accurately.

Figure 5-7 shows the predicted behavior of 104, 245, 1044 and 9584 ppbv CH₃I adsorption on Ag⁰-Aerogel at 150 °C using nth order SCM. The capacity loss caused by dry air aging effect was considered, and other parameters are $k_f = 2.71$ cm/s, $D_p = 6.70 \times 10^{-4}$ cm²/s, $n = 1.22$ and $k_s^* = 74.90$ (cm/s)·(mol/cm³)¹⁻ⁿ. Based on the results, for CH₃I adsorption on Ag⁰-Aerogel at 150 °C reaching saturation, 15.7K days are required at 104 ppbv condition, 7.7K days at 245 ppbv, 1.4K days at 1044 ppbv and 152 days at 9584 ppbv.

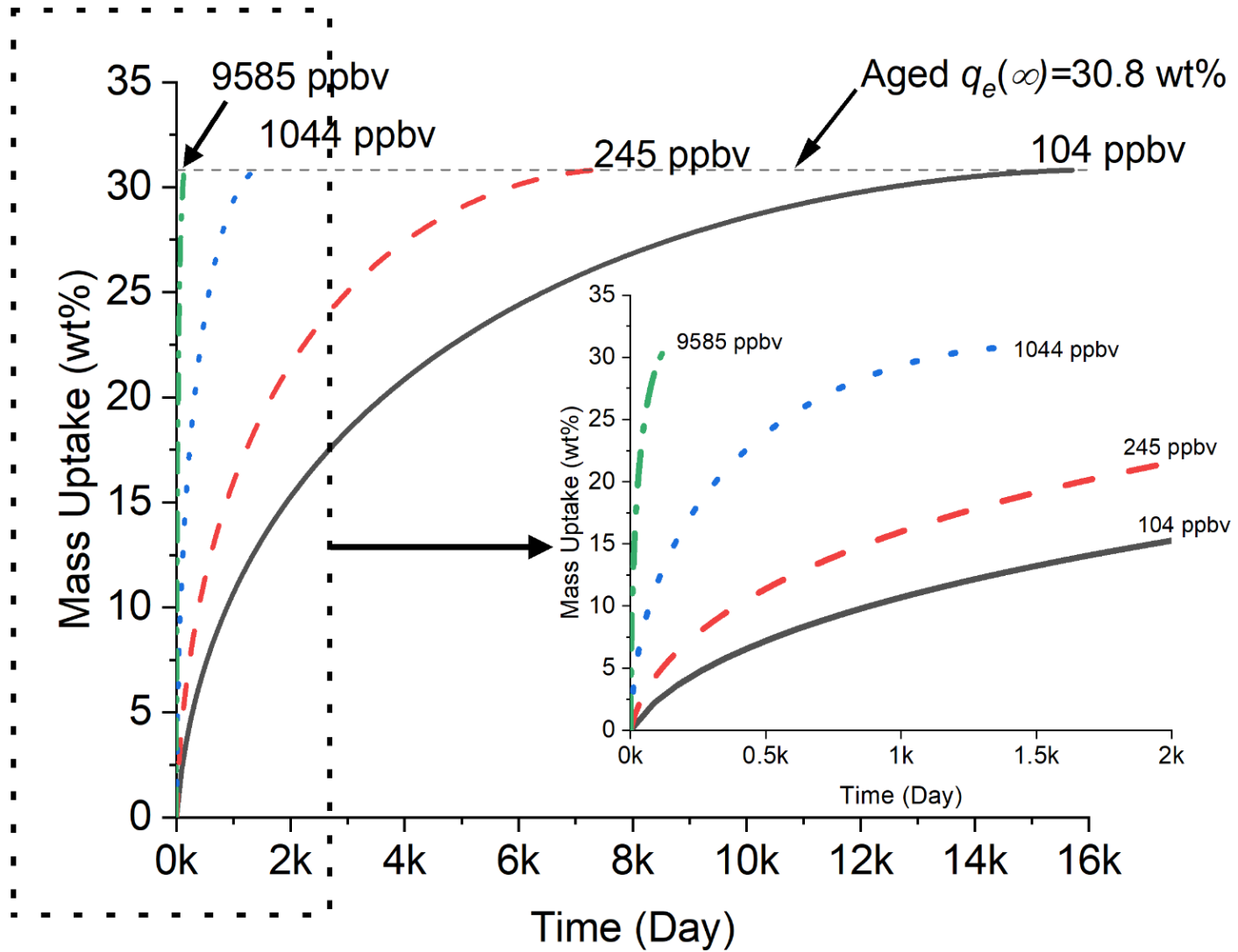


Figure 5-7. 104, 245, 1044 and 9584 ppbv CH₃I adsorption behavior prediction using nth order SCM.

The saturation times provided are based on only the initial part of the adsorption curve. For example, at 104 and 245 ppbv, the acquired results only contain 12-days of data, whereas the full adsorption processes would take decades. Admittedly, comparing the predictions with the data collected in a longer time period will provide more reliable and persuasive results. However, this is clearly not practicable. Therefore, the saturation times provided are only for estimation, but we expect that the actual times should be in the same time scale with our predictions.

5.7 Rate-Controlling Step

For further analysis and application of the SCM results, it is necessary to understand the rate-controlling step of the process. To determine how the CH₃I-Ag⁰-Aerogel adsorption is controlled, τ_1 , τ_2 , and τ_3 at 4 different concentrations were calculated using Eq 3-7 to 3-9 with the determined parameters shown in Table 5-2. τ_1 , τ_2 , and τ_3 are the partial adsorption saturation time contributed by the gas film diffusion, pore diffusion, and reaction term. More straightforwardly, the saturation time, t_{sat} , can be expressed as,

$$t_{sat} = \tau_1 + \tau_2 + \tau_3 \quad 5-18$$

For the SCM, the control term can be represented by overall resistance ratio, τ_i/t_{sat} , where $i = 1, 2, \text{ or } 3$.¹²⁵

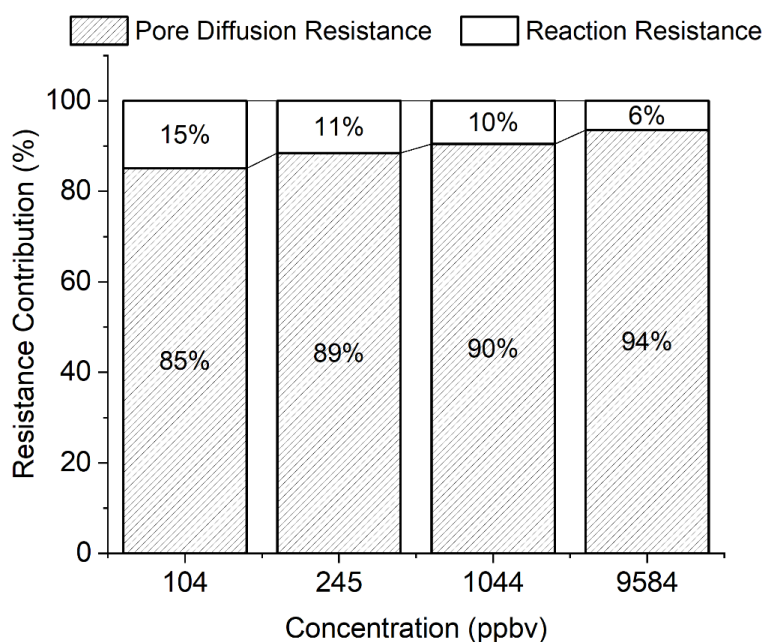


Figure 5-8. Resistance contributions of pore diffusion and reaction terms for $\text{CH}_3\text{I-Ag}^0\text{-Aerogel}$ adsorption at 104, 245, 1044 and 9584 ppbv.

Figure 5-8 shows the resistance contributions of the pore diffusion term and reaction term, whereas the gas film diffusion term is less than 1% and not shown in the figure. It was found that the reaction resistance contribution decreases from 15% at 104 ppbv to 6% at 9584 ppbv and the pore diffusion resistance contribution increases accordingly. Generally, for a given adsorption system, the resistance contribution is independent of the concentration of the adsorbate. Therefore, the change shown in Figure 5-8 is due to the n^{th} order reaction which has been discussed previously.

The adsorption rate is determined by the process with the highest resistance. Visualized from Figure 5-8, the pore diffusion contributes the most among the gas film diffusion, pore diffusion,

and reaction term, especially at high CH₃I concentration. Therefore, the CH₃I-Ag⁰-Aerogel adsorption is identified as an ‘overall’ diffusion-controlled process. The overall process is diffusion-controlled, but at certain conditions, the process may not be controlled by diffusion, which will be discussed in the following content. Moreover, as the concentration decreased from 9584 to 104 ppbv, the ratio of reaction resistance contribution increases accordingly, indicating that the CH₃I-Ag⁰-Aerogel adsorption may change from a pore diffusion-controlled to a reaction-controlled process if the concentration decreases substantially.

Although the overall process is controlled by the pore diffusion of CH₃I, at VOG conditions, the rate determining step may vary because of the actual adsorption process. As mentioned above, in the VOG stream, the CH₃I concentration is in ppbv level, and the adsorption rate is extremely low. For example, at 104 ppbv, the prediction of the single-layer adsorption shows that the adsorption may not reach saturation in decades. Therefore, in the industrial application, the active regions are only the initial parts of the adsorption curves. These regions correspond to the surface reaction between CH₃I and Ag⁰-Aerogel, which are highly reaction-controlled. In this process, CH₃I reacts with Ag on the surface of Ag⁰-Aerogel and only a limited amount of CH₃I diffuses into the pellets. Quantitatively speaking, at VOG conditions, the q/q_e term in Eq. 3-6 is much smaller than 1 and by specifying the q/q_e values, the real-time contributions of diffusion term and reaction term can be calculated. For example, as Figure 5-9 shows, at 104 ppbv, the reaction term contributes approximately 49% at $q = 5 \text{ wt}\%$, which approximately 300 days are required to reach this point. Additionally, within 1 months, the reaction term contribution is

higher than 80% and the mass uptake is below 1 wt%. Therefore, it is important to notice that although the overall adsorption process is controlled by the pore diffusion, at actual VOG conditions, the effect of pore diffusion to the uptake rate is minor in at least months. For the industry application purpose, when determining the $\text{CH}_3\text{I-Ag}^0\text{-Aerogel}$ adsorption behavior at low concentration conditions, the analysis should focus on the initial part, and this part is mainly controlled by the reaction rate instead of the pore diffusivity.

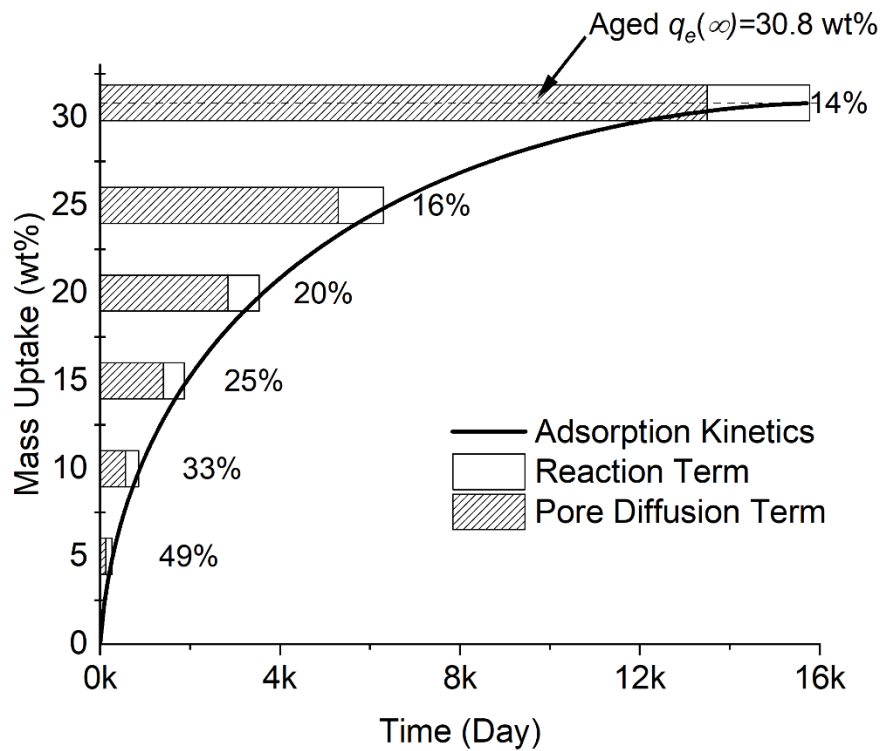


Figure 5-9. Real-time contribution of reaction term and pore diffusion term in $\text{CH}_3\text{I-Ag}^0\text{-Aerogel}$ adsorption at 104 ppbv (percentage represents reaction contribution).

Because the adsorption behavior at low concentration minorly depends on the gas film diffusion and pore diffusion term, the SCM in Eq. 3-6 can be reduced to Eq. 5-19 and the mass uptake rate is given by Eq. 5-20.

$$t = \left(1 - \left(1 - \frac{q}{q_e} \right)^{1/3} \right) \tau_3 \quad 5-19$$

$$\frac{dq}{dt} = \frac{3q_e(\tau_3 - t)^2}{\tau_3^3} \quad 5-20$$

Since at the initial region, $t \ll \tau_3$, Eq. 5-20 can be written as Eq. 5-21 for n^{th} order reaction.

$$\frac{dq}{dt} = \frac{3bk_s^* C_b^n}{R_a \rho_p} \quad 5-21$$

Furthermore, by replacing R_a and ρ_p , Eq. 5-21 becomes,

$$\frac{dq}{dt} = Abk_s^* C_b^n \quad (\text{When } t \ll t_{sat} \text{ and } q \ll q_e) \quad 5-22$$

where A is the specific surface area (cm^2/g) of the material. This result indicates that at VOG conditions, the initial part, the only region need be considered, of n^{th} order SCM reduces to a simple n^{th} order surface reaction with a constant uptake rate, which can be demonstrated by 104 and 245 ppbv adsorption curves in Figure 5-1. However, to increase the adsorption efficiency, simply increasing the surface area by reducing the diameter may not be applicable. The surface reaction condition may not hold due to the change of flow regime caused by fine pellets.

5.8 Potential Reaction Mechanism

For the chemisorption with gas phase product generated, Zhou and White¹⁴⁵ and Robb and Harriott¹⁴⁶ suggested that the formation of gases and the successive diffusion limitations may result in a fractional order reaction, which has been observed in the CH₃I adsorption. To explain this observation, a potential reaction pathway is proposed.

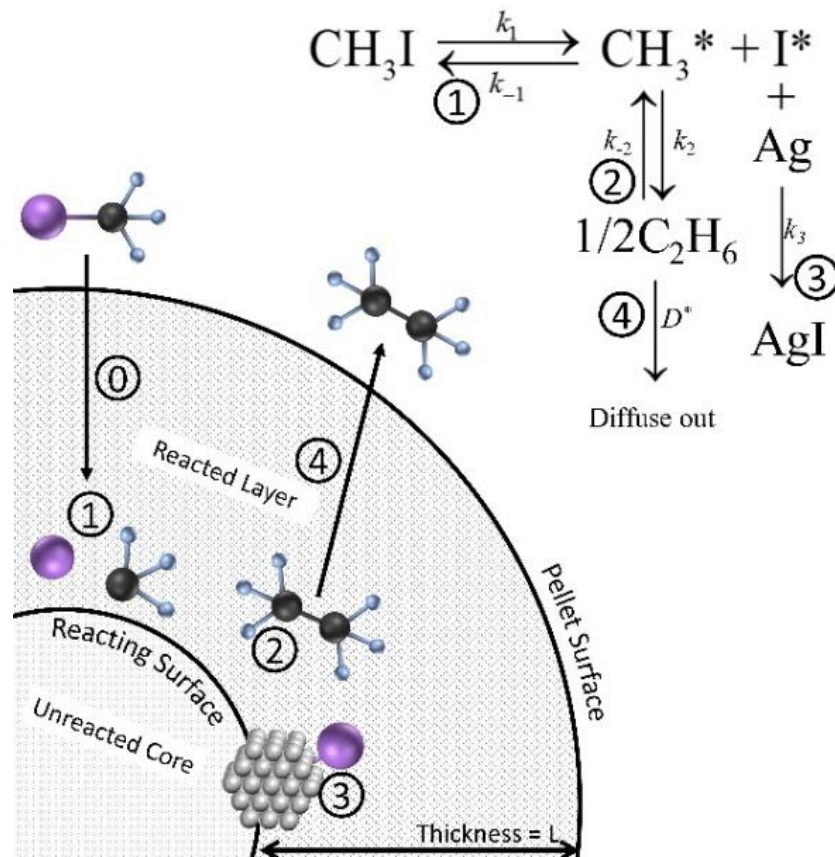


Figure 5-10. The proposed reaction pathway between CH₃I and Ag in Ag⁰-Aerogel.

In the shrinking core model, the reactions only happen on the reacting surface, which separates the reacted layer and the unreacted core. Once the Ag sites on one surface are fully consumed, the reactions proceed to the next surface. As Figure 5-10 shows, during the adsorption, CH₃I first

diffuses through the reacted layer and reaches the reacting surface (0). On the reacting surface, CH₃I breaks reversibly into two free radicals (1), CH₃^{*} and I^{*}. Two CH₃^{*} radicals bind with each other and form C₂H₆ (2); I^{*} radical binds with Ag and forms AgI (3); and C₂H₆ diffuses out through the reacted layer (4). In this process, to satisfy the observed 1.22 reaction order, the reaction order of CH₃I is assumed to be *n*; the orders of other reactions are 1 to each component; and the reason will be discussed in the following contents.

The formation/consumption rates of the components can be written as,

$$r_{CH_3I} = -k_1 C_{CH_3I}^n + k_{-1} C_{CH_3^*} C_{I^*} \quad 5-23$$

$$r_{I^*} = k_1 C_{CH_3I}^n - k_3 C_{I^*} - k_{-1} C_{CH_3^*} C_{I^*} \quad 5-24$$

$$r_{CH_3^*} = k_1 C_{CH_3I}^n - k_{-1} C_{CH_3^*} C_{I^*} - k_2 C_{CH_3^*} + k_{-2} C_{C_2H_6} \quad 5-25$$

$$r_{C_2H_6} = k_2 C_{CH_3^*} - k_{-2} C_{C_2H_6} - \frac{D^* C_{C_2H_6}}{L} \quad 5-26$$

where *k*'s are the surface reaction rate constants, *D*^{*} is the diffusivity of C₂H₆, and *L* is the thickness of the reacted layer. The stoichiometric coefficient of C₂H₆ is ignored in the equations since it does not impact the results.

Assuming pseudo-equilibrium, the steady state is established immediately after the reactions proceed to the next surface, CH₃^{*}, I^{*} and C₂H₆ are assumed to not accumulate on the reacting surface and the rates, *r*_{CH₃^{*}}, *r*_{I^{*}}, and *r*_{C₂H₆} should be 0.

Set Eq. 5-26 = 0 and solve for *C*_{C₂H₆},

$$r_{C_2H_6} = k_2 C_{CH_3^*} - k_{-2} C_{C_2H_6} - \frac{D^* C_{C_2H_6}}{L} = 0 \quad 5-27$$

$$C_{C_2H_6} = \frac{k_2 C_{CH_3^*}}{\left(k_{-2} + \frac{D^*}{L}\right)} \quad 5-28$$

Set Eq. 5-24 = 0 and solve for C_{I^*} ,

$$r_{I^*} = k_1 C_{CH_3I}^n - k_3 C_{I^*} - k_{-1} C_{CH_3^*} C_{I^*} = 0 \quad 5-29$$

$$C_{I^*} = \frac{k_1 C_{CH_3I}^n}{k_3 + k_{-1} C_{CH_3^*}} \quad 5-30$$

Insert Eq. 5-28 and Eq. 5-30 into Eq. 5-25, set Eq. 5-25 = 0 and solve for $C_{CH_3^*}$,

$$r_{CH_3^*} = k_1 C_{CH_3I}^n - k_{-1} C_{CH_3^*} \frac{k_1 C_{CH_3I}^n}{k_3 + k_{-1} C_{CH_3^*}} - k_2 C_{CH_3^*} + k_{-2} \frac{k_2 C_{CH_3^*}}{\left(k_{-2} + \frac{D^*}{L}\right)} = 0 \quad 5-31$$

Reorganize Eq. 5-31,

$$k_1 C_{CH_3I}^n - k_{-1} C_{CH_3^*} \frac{k_1 C_{CH_3I}^n}{k_3 + k_{-1} C_{CH_3^*}} = k_2 C_{CH_3^*} - k_{-2} \frac{k_2 C_{CH_3^*}}{\left(k_{-2} + \frac{D^*}{L}\right)} \quad 5-32$$

Further reorganize,

$$k_1 C_{CH_3I}^n \left(1 - \frac{k_{-1} C_{CH_3^*}}{k_3 + k_{-1} C_{CH_3^*}}\right) = k_2 C_{CH_3^*} \left(1 - \frac{k_{-2}}{\left(k_{-2} + \frac{D^*}{L}\right)}\right) \quad 5-33$$

Define,

$$\Phi = \frac{k_{-2} L}{D^*} \quad 5-34$$

Eq. 5-33 can be written as,

$$\frac{k_1 k_3 C_{CH_3I}^n}{k_3 + k_{-1} C_{CH_3^*}} = \frac{k_2 C_{CH_3^*}}{1 + \Phi} \quad 5-35$$

Linearize Eq. 5-35,

$$k_{-1}k_2C_{CH_3^*}^2 + k_2k_3C_{CH_3^*} - (1 + \Phi)k_1k_3C_{CH_3I}^n = 0 \quad 5-36$$

Solve for $C_{CH_3^*}$,

$$C_{CH_3^*} = \frac{-k_2k_3 + \sqrt{k_2^2k_3^2 + 4k_1k_{-1}k_2k_3C_{CH_3I}^n(1 + \Phi)}}{2k_{-1}k_2} \quad 5-37$$

Reorganize,

$$C_{CH_3^*} = \frac{\sqrt{\frac{4k_1k_{-1}C_{CH_3I}^n(1 + \Phi)}{k_2k_3} + 1} - 1}{2k_{-1}/k_3} \quad 5-38$$

or,

$$\frac{k_{-1}C_{CH_3^*}}{k_3} = \frac{\sqrt{\frac{4k_1k_{-1}C_{CH_3I}^n(1 + \Phi)}{k_2k_3} + 1} - 1}{2} \quad 5-39$$

Plug Eq. 5-30 to Eq. 5-23 and reorganize,

$$r_{CH_3I} = -\frac{k_1C_{CH_3I}^n}{1 + \frac{k_{-1}C_{CH_3^*}}{k_3}} \quad 5-40$$

Plug Eq. 5-39 to Eq. 5-40, r_{CH_3I} can be written as Eq. 5-41,

$$r_{CH_3I} = -\frac{2k_1C_{CH_3I}^n}{\sqrt{\frac{4k_1k_{-1}C_{CH_3I}^n(1 + \Phi)}{k_2k_3} + 1} + 1} \quad 5-41$$

$$\Phi = \frac{k_{-2}L}{D^*} \quad 5-42$$

where Φ is similar to the Thiele modulus, the ratio of the reaction rate to the diffusion rate.¹⁴⁷

As more than five parameters are included, determining the r_{CH_3I} step-wise would be

impractical. Considering two limiting cases, when $\frac{4k_1k_{-1}C_{CH_3I}^n(1+\Phi)}{k_2k_3} \gg 1$, the reaction rate

r_{CH_3I} would be proportional to $C_{CH_3I}^{n/2}$; if $\frac{4k_1k_{-1}C_{CH_3I}^n(1+\Phi)}{k_2k_3} \ll 1$, r_{CH_3I} would be proportional to

$C_{CH_3I}^n$. Since the reaction order would be between $n/2$ and n , the integer that satisfies the observed 1.22 order is $n = 2$.

Additionally, Eq. 5-41 indicates that the temperature change may impact the reaction rate.

Generally, the relationship between k (or D) and T can be written as Eq. 5-43,

$$\ln\left(\frac{k'}{k}\right) = -\frac{\Delta E}{R}\left(\frac{1}{T'} - \frac{1}{T}\right) \quad 5-43$$

which implies that the temperature change may impact the overall reaction rate by changing the

magnitude of $\frac{4k_1k_{-1}C_{CH_3I}^n(1+\Phi)}{k_2k_3}$.

5.9 Conclusions

The kinetic data of CH₃I adsorption on Ag⁰-Aerogel at 150 °C were obtained using the continuous flow adsorption system. The CH₃I concentrations were 104, 245, 1044 and 9584 ppbv. Because the corresponding shrinking core process was observed, the shrinking core model was applied to determine the gas film diffusivity, pore diffusivity and reaction rate constant. The 1st order reaction was originally assumed. The well-agreed pore diffusivities were determined in three of the total four trials. The average value was $6.70 \pm 0.73 \times 10^{-4}$ cm²/s. Orderly increasing reaction rate constants were observed and, therefore, the modified nth order SCM was selected

for analysis.

The reaction order of $\text{CH}_3\text{I-Ag}^0$ -Aerogel adsorption was calculated to be approximately 1.22 and the reaction rate constant was approximately $74.90 \text{ (cm/s)} \cdot (\text{mol/cm}^3)^{1-n}$. This n^{th} order SCM effectively increases the accuracy of adsorption behavior prediction. Using n^{th} order SCM instead of 1^{st} order SCM, the *AARD* of 104 ppbv adsorption behavior prediction decreases from 50.63% to 14.52% (Figure 5-6). Furthermore, the overall single-layer adsorption behaviors at 104, 245, 1044 and 9584 ppbv were predicted. For example, it requires more than 40 years for a single-layer Ag^0 -Aerogel reach to saturation at 104 ppbv, 150 °C and 500 sccm flow rate condition with the capacity loss due to dry air aging effects incorporated.

The rate-controlling step of $\text{CH}_3\text{I-Ag}^0$ -Aerogel adsorption was identified by plotting the resistance of different rate-dependent terms. Although the overall adsorption process is controlled by pore diffusion, the surface reaction between CH_3I and Ag is more crucial at VOG conditions in a predictable time period. The nature of low concentration in VOG streams limits the adsorption from a full n^{th} order SCM to a surface reaction. To increase the adsorption efficiency, decreasing the size of pellets is a theoretically applicable method. However, the detailed solution still requires further studies in deep-bed adsorption. By replacing the 1^{st} order SCM by n^{th} order SCM, the accuracy of adsorption behavior prediction at VOG conditions was increased significantly.

To determine the adsorption behavior for the column adsorption at ppb levels, it should be noticed that the adsorption process is mainly controlled by the surface reaction and the complete

saturation of pellets may not happen during the test period. For the column adsorption modeling, using only the n^{th} order SCM is insufficient, and directly applying the saturation time estimated in the presented work may be inappropriate. However, the idea of fractional reaction order and the parameters determined can be widely applied to the deep-bed adsorption system design of the off-gas treatment in the nuclear fuel reprocessing process.

Chapter 6. CH₃I Adsorption on Ag⁰-Aerogel: Temperature Dependence

6.1 Introduction

In Chapter 5, the results of 104, 245, 1044 and 9584 ppbv CH₃I adsorptions indicated that the adsorption is likely to be a shrinking core process and by applying the corresponding models, the diffusivities and reaction rate constants were determined. The diffusivities D_p 's determined were relatively constant with an average value of $6.70 \pm 0.73 \times 10^{-4}$ cm²/s. However, the reaction rate constants k_s 's change with concentration, which indicates that the reaction between CH₃I and Ag⁰-Aerogel may not be 1st order. Therefore, the SCM was modified to a nth order SCM and the reaction order determined was 1.22 and the nth order reaction rate constant was 74.90 (cm/s)·(mol/cm³)¹⁻ⁿ.

To further analyze the CH₃I adsorption behavior, additional experiments at 100 and 200 °C were performed at 104 and 1044 ppbv and the results were compared with the 150 °C adsorption.

During the experiments, an abnormally high uptake rate was observed for 104 ppbv CH₃I adsorption at 200 °C, and multiple physical analyses including nitrogen titration, scanning electron microscopy (SEM) and x-ray photoelectron spectroscopy (XPS) were performed. Based on the data collected and theoretical analyses, the factors impacting the uptake rate appear to be, unusual reactions and products, difference in silver site availability, change of diffusion limitation and impact of temperature to reaction rate described by the Arrhenius relationship.

6.2 Procedure Description

Using the continuous flow adsorption system, the mass changes of Ag⁰-Aerogel were recorded and the kinetic adsorption curves were generated. In this presented work, the adsorption experiments of 104 ppbv and 1044 ppbv of CH₃I at 100, 150 and 200 °C were performed. Since reaching equilibrium is not realistic at ppbv level concentrations, the experiments were stopped at approximately 300 hours.¹⁴⁸

Before the start of the organic iodide adsorption, the pellets were air-dried at the same temperature as that of the adsorption experiment until the mass change in the past 24 hours is lower than 0.005 wt% (approximately 1/5 of the adsorption rate of 104 ppbv CH₃I at 150 °C). Especially, at 200°C, the drying process induced the loss of organic moiety of up to 9 -10 wt%, which a similar observation was reported in Matyáš and Engler's thermogravimetric analysis (TGA).¹⁴⁹

Therefore, to determine the effect of organic moiety loss, the comparison experiments were performed at 104 ppbv-CH₃I-150°C and 1044 ppbv-CH₃I-150 °C using the Ag⁰-Aerogel with and without the organic moiety loss. The results showed no significant difference in the uptake curves (in wt%). To further accelerate the drying process (which usually takes weeks) and removing the organic moiety for all experiments, the pellets were vacuum dried overnight at 350 °C using the degas function of Surface Area and Porosity Analyzer (Micromeritics, ASAP 2020) and stored in N₂ after the treatment. Similarly, after degassing, the adsorption curves (in wt%) and the maximum iodine capacities (approximately 37 – 38 wt%, measured by 50 ppmv I₂

adsorption at 150 °C) are similar to the untreated adsorbent. It is important to notice that during the 350 °C treatment, the organic moiety loss results in approximately 10 % loss of pellet mass. Therefore, the similar uptake rate by pellet mass indicates an approximately 10% loss of uptake rate by silver mass. However, this loss could be considered as a ‘worthy cost’ due to the successive significant increase of the organic iodide uptake rate at 200 °C, which will be discussed in the following sections.

6.3 Adsorption Kinetics

The 104 ppbv and 1044 ppbv CH₃I adsorptions on Ag⁰-Aerogel at 100, 150 and 200 °C were performed using the continuous flow adsorption system. For consistency purposes, pellets used for all trials were vacuum dried at 350 °C before the adsorption. After the pre-dry process, the pellets were moved to the adsorption system and the final water equilibrium process (flowing the carrier gas at the target adsorption temperature) was performed before starting the adsorption.

Once the mass change of the pellets in the past 24h was less than 0.005 wt%, the CH₃I adsorption was started. During the CH₃I adsorption, no significant mass gain/loss was observed neither in the initial part (first 1-2 days) nor after the adsorption ended and the desorption started, which indicating the physisorption of CH₃I on Ag⁰-Aerogel is relatively minor.

The kinetic curves are shown in Figure 6-1, at 100 and 150 °C, the tendency agrees well with the previous studies of I₂ adsorption on Ag⁰Z⁹⁵, that the adsorption rates increase slightly as the temperature increases. However, at 200 °C, the uptake rate increases significantly (3 – 4 times

higher) at 104 ppbv, and the curvature of the curve decreases at 1044 ppbv. To analyze such abnormal behaviors, the shrinking core model (SCM) was applied. The parameters and results determined using the SCM are listed in Table 6-1. At 104 ppbv, the D_p 's were not determined since no significant pore diffusion processes were observed during the experiments.

It can be visualized that, at 200 °C, certain abnormal behaviors exist for both 104 and 1044 ppbv CH₃I adsorption. To explain such observation, the nitrogen titration, XPS and SEM-EDX analyses were performed and a potential reaction pathway was proposed.

Concentration (ppbv)	Temperature (°C)	k_f (cm/s)	D_p (cm ² /s)	k_s (cm/s)	AARD (%)
104	100	2.18*	N.D**	0.17	11.64%
	150	2.71*	N.D**	0.23	14.74%
	200	3.29*	N.D**	0.67	11.51%
1044	100	2.18*	3.48×10^{-4}	0.30	1.90%
	150	2.71*	7.07×10^{-4}	0.40	1.87%
	200	3.29*	5.45×10^{-3}	0.29	1.19%

*Calculated theoretically

**Not determined.

Table 6-1. Parameters and results of the SCM

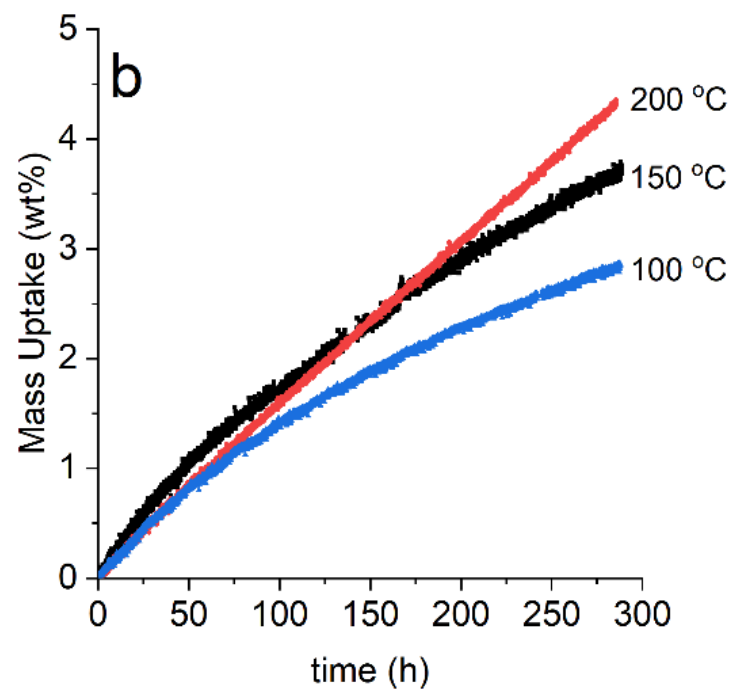
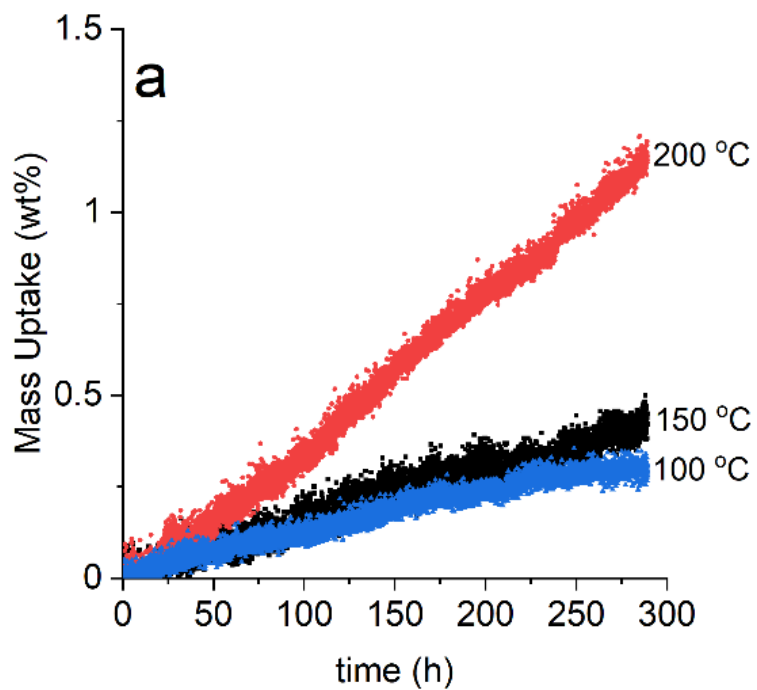


Figure 6-1. The CH₃I adsorption curves of 104 ppbv (a) and 1044 ppbv (b) at 100, 150 and 200 °C.

6.4 Water Equilibrium in Drying Process

Because of multiple factors including the pellet size of Ag⁰-Aerogel, the internal structure of Ag⁰-Aerogel, etc., the water concentration in the pellets after 350 °C vacuum drying may not be constant. Therefore, a final drying is still required before the CH₃I adsorption and the pellets may adsorb or desorb water in different trials. The water adsorbed was from the trace amount of moisture contained in the carrier gas (Airgas Inc. Air, Ultra Zero). According to the manufacturer, the air contains approximately 2 ppmv of water and the value was also validated by experimental measurement using a dewpoint meter. By selecting a water adsorption curve with the highest uptake (therefore the initial water concentration in the pellet can be assumed to be zero), the water adsorption process can be modeled using multiple models including the 1-D spherical Fick's Law¹²⁷ (Eq. 6-1), differential form of the diffusion term of the shrinking core model (SCM)¹²⁷ (Eq.6-2), and the micropore term of the pore diffusion model (PDMI)¹⁵ (Eq.6-3). For Fick's law and the shrinking core model, it is assumed that an equilibrium is established on the surface immediately.

$$\frac{\partial q(r,t)}{\partial t} = D_p \frac{1}{r^2} \frac{\partial}{\partial r} \left(r^2 \frac{\partial q(r,t)}{\partial r} \right) \quad 6-1$$

$$V \frac{dq(r,t)}{dt} = 4\pi r^2 D_p \frac{dq(r,t)}{dr} \quad 6-2$$

$$\frac{q}{q_e} = 1 - \frac{6}{\pi^2} \sum_{n=1}^{\infty} \frac{1}{n^2} \exp\left(-\frac{n^2 \pi^2 D_i t}{R_i^2}\right) \quad 6-3$$

$q(r,t)$ is the sorbate concentration (mol/cm³ or g/cm³) at radius r (cm) at time t (s), and the average sorbate concentration $q(t)$ can be calculated using,

$$q(t) = \frac{1}{V} \int_0^r 4\pi r^2 q(r,t) dr \quad 6-4$$

D_p is the pore diffusivity (cm^2/s), r is the radius at time t , V is the volume of the pellet (cm^3), D_i is the micropore diffusivity (cm^2/s) and R_i is the radius of the micropore (cm). R_i was measured by the nitrogen adsorption method using ASAP 2020 and the value is approximately 6.6 \AA .

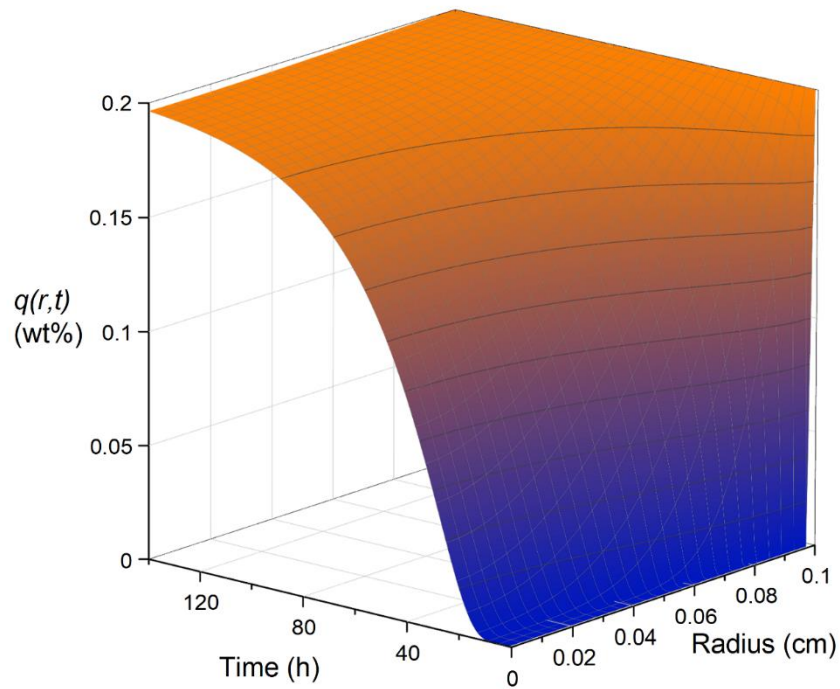


Figure 6-2. The 3-D fitting results of the Fick's law.

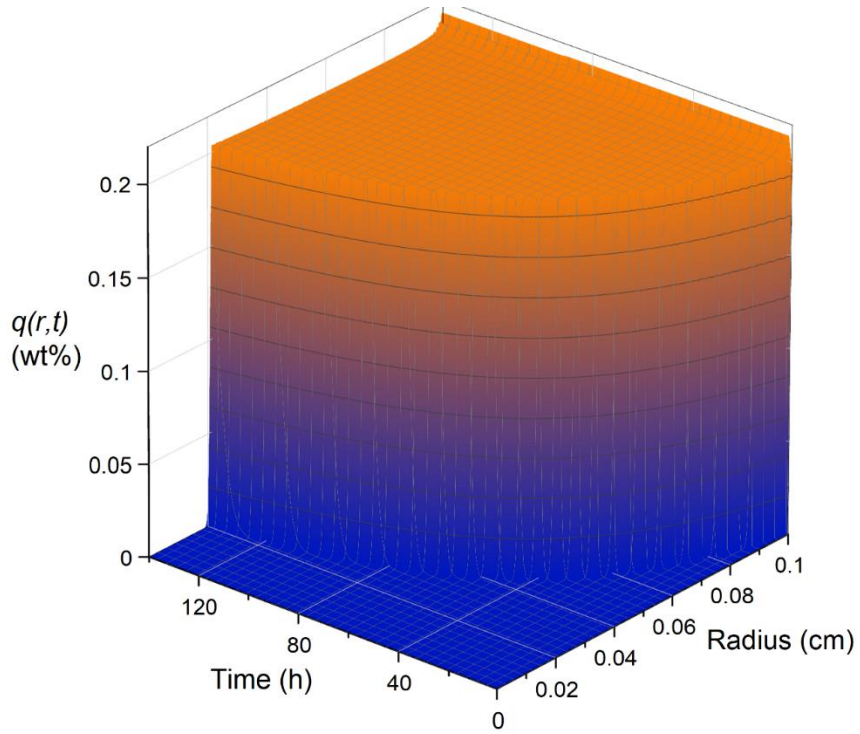


Figure 6-3 The 3-D fitting results of the SCM.

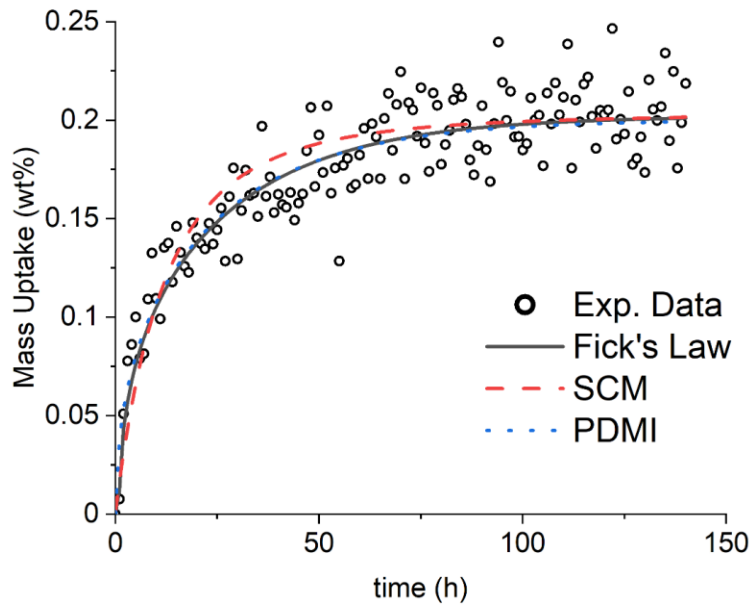


Figure 6-4. The adsorption curve and the modeling results of the water adsorption process

(Fick's Law and PDMI are overlapped).

The 3-D fitting results of the Fick's law and shrinking core model are plotted in Figure 6-2 and Figure 6-3; the experiment data and the model fitting results are shown in Figure 6-4. The diffusivities determine using Fick's Law, SCM and PDMI are 9.6×10^{-9} cm²/s, 2.6×10^{-8} cm²/s and 4.4×10^{-21} cm²/s respectively. By comparing with multiple literature works^{150,151}, the values of the diffusivities clearly fit in the range of micropore diffusion, indicating that the water adsorption/desorption in Ag⁰-Aerogel is a micropore diffusion process.

6.5 Nitrogen Adsorption Analyses

Since the carrier gas contains approximately 2 ppmv of water, the Ag⁰-Aerogel tends to reach moisture equilibrium with the ambient air during the adsorption of CH₃I. The moisture levels in the pellet at 100, 150, 200 °C were measured using the pre-dried pellet and the continuous flow adsorption system. The pre-dried (350 °C degassed) pellets were placed into the adsorption system with identical settings except flowing pure air instead of air/CH₃I mixture. The temperature of the adsorption column was firstly set at 200 °C, and the pellets started to adsorb water from the ambient air, with the mass change collected continuously. Once the mass change in the past 24h was less than 0.005 wt%, the temperature was decreased to 150 °C and further down to 100 °C when the same criterion was met. The time to settle a new equilibrium was 100 – 150 hours.

The results indicated that the differences in water concentration between each temperature were approximately 0.15 – 0.2 wt%. In other words, if the water concentration in the pellets at 200 °C

was set as the zero point, the water adsorbed at 150 and 100 °C were approximately 0.2 and 0.4 wt%. To examine such observation, the water desorption experiment in the reverse temperature order was also performed and the differences between each level were comparable.

In order to determine the effect of different concentrations of moisture in the pellets at various temperatures, the nitrogen adsorption analyses were performed using the Surface Area and Porosity Analyzer (Micromeritics, ASAP 2020). Traditionally, the samples used for nitrogen adsorption analysis were fully dried to prevent any residual water to influence the results. Since the standard drying conditions for Ag⁰-Aerogel were not reported, the fully dried result was the one with the highest pore volume and surface area, selected from multiple 350 °C degassed trials. Instead, to determine the surface area and pore volume at real adsorption temperatures, the Ag⁰-Aerogel was air dried using the adsorption column at the target temperatures (100, 150 and 200 °C) with the same criterion described above. Once the drying process was completed, the pellets were transferred to ASAP 2020 as quickly as possible (2-3 min). To minimize the potential water gain/loss during the analyses, multiple methods were applied including, minimize the time of transferring sample, measure the free volume of the test tube in advance (therefore, exposing the dried sample under vacuum at room temperature could be avoided), submerge the sample in liquid nitrogen immediately, only start the vacuum pump after the sample was submerged, and minimize the analysis time by selecting the minimal amount of sample points. Once the analysis was completed, the sample was transferred back to the adsorption column to measure the mass change during the porosity analysis. Since no significant mass changes were

observed, the water gain/loss during the analysis appears to be minor.

As a reference of the highest level of water that could be contained in the pellet during actual industrial usage, the nitrogen adsorption experiment without any sample pretreatment was also performed using normally stored Ag^0 -Aerogel (named as Room Condition Equilibrium in Figure 6-5, short as RC.EQ). The storage conditions measured by laboratory thermometer and hydrometer are, 20 – 23 °C and 20 – 30% humidity.

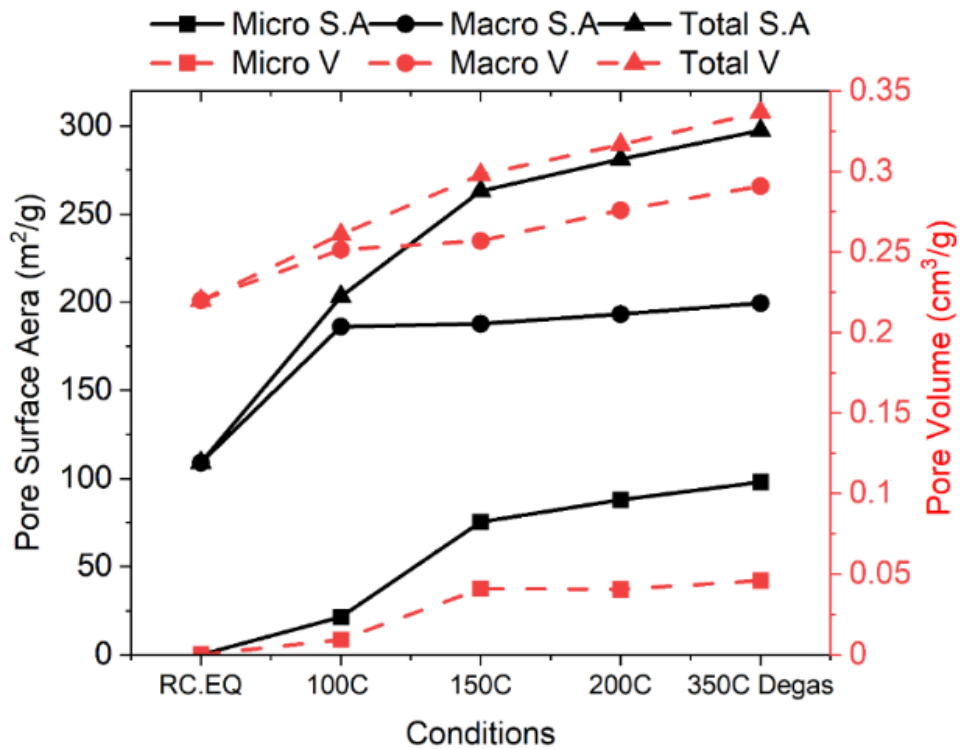


Figure 6-5. The surface area and pore volume of micropores, macropores and total pores measured using nitrogen titration method at different drying conditions.

The micro, macro and total pore surface area and volume are plotted in Figure 6-5. The total pore surface area of the 350 °C degassed sample is 297.6 m²/g and the total pore volume is 0.34 cm³/g, which are comparable with the trends of surface area and pore volume to silver composition in silica aerogel reported by Balkis Ameen et al.¹⁵²

Additionally, the plot shows that as the temperature decreases and the in-pellet water concentration increases, both pore surface area and pore volume decrease. As the temperature decreases to 100 °C, the micropores are significantly blocked by water and become fully blocked at room condition equilibrium.

Moreover, the diffusion of CH₃I and related gas form products in Ag⁰-Aerogel may also be impacted by the porosity change. The porosity ($\varepsilon = \text{total pore volume} / \text{density}$) of the pellet is larger at higher temperature, and an experimental relationship between pore diffusivity and porosity is given as,¹⁵³

$$D_p / D_{AB} = \varepsilon_p^m \quad 6-5$$

where m is usually between 2 – 4.5 depending on the material. This relationship indicates that the pore diffusivities of both CH₃I and gas phase products may increase with increasing temperature (D_{AB} increases with temperature), and therefore decreasing the diffusion limitations and speeding-up the adsorption process.

6.6 Pore Distribution and Silver Site Availability

Shown in Figure 6-5, the drying temperature impacts the pore surface area and the pore volume of the pellets by changing the water concentration in the pellet. When temperature decreases to below 100 °C, the micropores are significantly impacted. This can be further visualized by comparing the pore distribution plots of the Barrett-Joyner-Halenda (BJH) desorption method and the density function theory (DFT) of 350 °C degassed and room condition equilibrium samples.

The pore distribution plots (Figure 6-6) show that the Ag⁰-Aerogel mostly consists of mesopores (20-500 Å) and micropores (<20 Å) with a limited amount of macropores (> 500 Å), which agree with the SEM images that no significant structure was observed in the micrometer scale.

Comparing the two curves in Figure 6-6. b, two sharp peaks at approximately 6 and 12 Å were observed only in the fully dried sample, whereas the room condition equilibrium one only contained a small peak at 15-17 Å. A similar trend is also revealed in Figure 6-6. a: the 350 °C degassed sample contains a ‘tail’ at 20-25 Å.

Such observation further supports that the micropores (< 2 nm) are mostly blocked as the in-pellet water concentration increases (Discussed in **Section 6.5**) and the water adsorption/desorption process in Ag⁰-Aerogel is a micropore diffusion process (Discussed in **Section 6.4**).

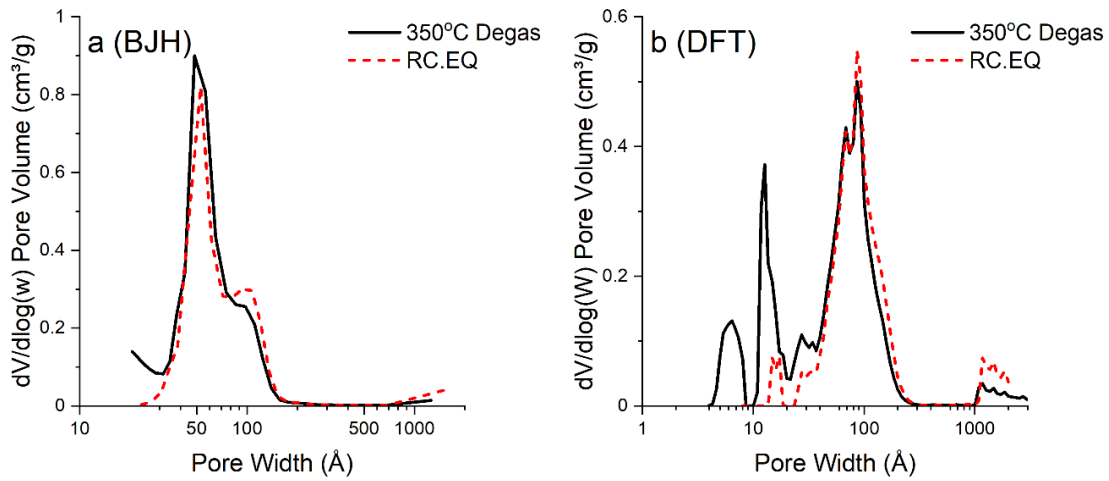


Figure 6-6. The BJH (a) and DFT (b) pore distribution plots of 350 °C degassed sample and room condition equilibrium (RC.EQ).

Since both pore surface area, pore volume and the amount of micropores decrease as the adsorption temperature decreases, the availability of silver sites may decrease due to the increasing water coverage.

6.7 Arrhenius Relationship and Eyring Equation

The well-known Arrhenius relationship is commonly used in describing the temperature dependence of reaction rate constant and diffusivity, which is, ¹⁴⁴

$$k_s = k_s^0 e^{-\Delta E/RT} \quad (\text{replace } k_s \text{ with } D \text{ for diffusion}) \quad 6-6$$

and the linear form is,

$$\ln(k_s) = \ln(k_s^0) + \left(\frac{-\Delta E}{R} \right) \left(\frac{1}{T} \right) \quad 6-7$$

Where k_s^0 is the pre-exponential factor (unit same as k_s), ΔE is the activation energy (kJ/mol) and R is the gas constant (kJ/mol/K). Discussed in **Chapter 5**, the CH_3I adsorption on Ag^0 -Aerogel may be a 1.22 order shrinking core process, where the calibrated k_s^* ($(\text{cm/s}) \cdot (\text{mol}/\text{cm}^3)^{1-n}$) can be represented as $k_s^* = k_s^0 C_b^{1-n}$. Therefore, the Arrhenius equation was applied to the calibrated k_s^* and the plot including the fitting results are shown in Figure 6-7.

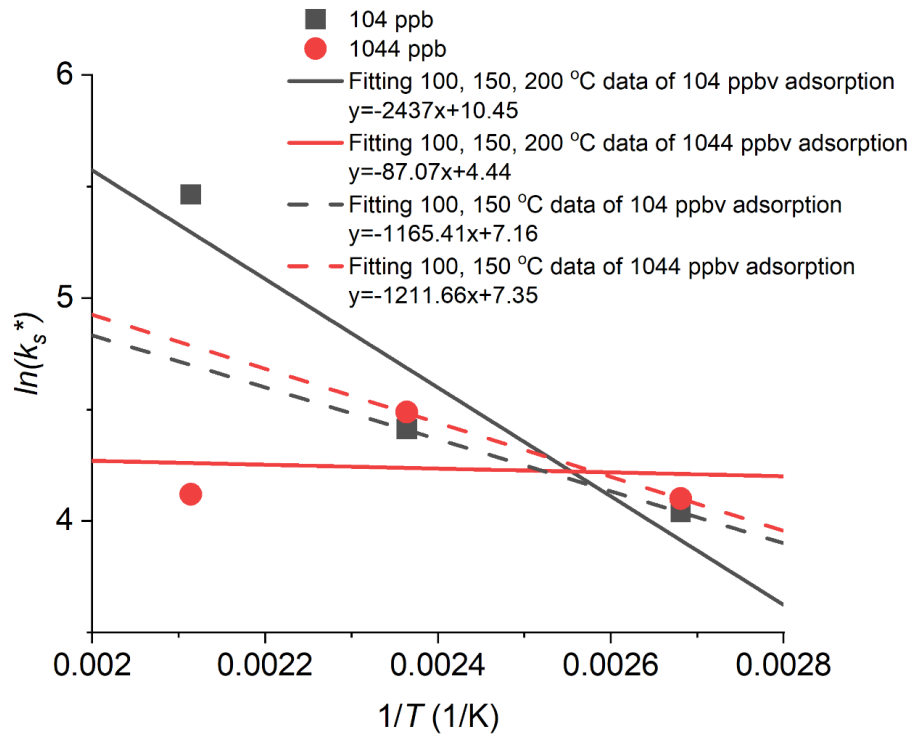


Figure 6-7. The Arrhenius plot of 104 and 1044 ppbv CH_3I adsorptions on Ag^0 -Aerogel at 100, 150 and 200 °C.

By fitting all three data points at each concentration, the ΔE 's are 20.21 and 0.64 kJ/mol for 104 and 1044 ppbv adsorptions respectively. As stated above, both adsorption behaviors at 200 °C are relatively abnormal. If excluding the 200 °C data and consider the 100 and 150 °C results only,

the ΔE 's of 104 and 1044 ppbv adsorptions are well-agreed. The activation energy determined using 100 and 150°C data of 104 ppbv adsorption is 8.6 kJ/mol, that of 1044 ppbv adsorption is 8.2 kJ/mol and the pre-exponential factors are 904 and 848 (cm/s)·(mol/cm³)¹⁻ⁿ respectively. The activation energy determined appear to be reasonable comparing with previous studies. Park et al.¹⁵⁴ performed the CH₃I adsorption on silver ion-exchange ZSM-5 (Ag-ZSM-5) at 50, 70, 90, 120 and 150 °C and reported the activation energy of 2.57 kJ/mol and Scheele et al.⁶⁸ proposed 20 – 40 kJ/mol for CH₃I adsorption on Ag⁰Z.

Another model describing the relationship between temperature and reaction rate constant is the Eyring equation,¹⁵⁵

$$k = \frac{k_B T}{h} e^{-\Delta G/RT} \quad 6-8$$

where k is the reaction rate (s⁻¹), k_B is Boltzmann's constant, h is Planck's constant and ΔG is the Gibbs free energy of activation. Since the unit and the physical meaning of k are different from k_s determined using SCM, a quantified result may not be given. However, some valuable trends and predictions can be interpreted. Representing the Gibbs free energy of the activation of the reaction between iodoalkane and Ag⁰-Aerogel as ΔG , dk/dT may be written as,

$$\frac{dk}{dT} = e^{-\Delta G/RT} \left(\frac{k_B}{hT} \right) \left(\frac{\Delta G}{R} + T \right) \quad 6-9$$

Eq. 6-9 indicates that the dependency of k to T may vary as $\Delta G/R$ changes. For example, given a range of temperature T_1 to T_3 , Figure 6-8 shows that how $-\Delta G/R$ changes the dependency of k to T .

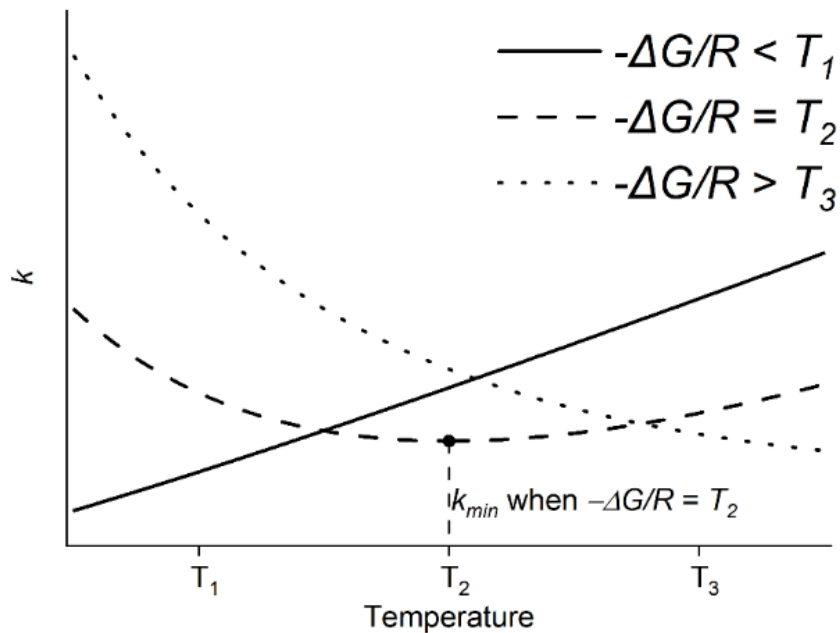


Figure 6-8. An example of the Eyring equation, how $\Delta G/R$ changes the dependency of k to T (curves have been rescaled and repositioned to clarify the tendencies).

When $-\Delta G/R < T_1$, $dk/dT > 0$, indicating the increasing temperature increases the reaction rate; when $-\Delta G/R > T_3$, $dk/dT < 0$, and the reaction rate may decrease with increasing temperature.

Interestingly, if $T_1 < -\Delta G/R < T_3$, a minimum value of k may be observed at $T = -\Delta G/R$.

Generally, the ΔG is represented as a positive number, but can it be negative in some circumstances?

Proposed in the **Chapter 5**, iodoalkane molecules may cleave into free radicals and produce alkanes and AgI in the re-bindings of radicals. The negative activation energies have been reported in some radicals-engaged reactions.^{156,157} Therefore, in the adsorptions of iodoalkanes

with larger alkane groups (e.g. C₆H₁₃I, C₁₂H₂₅I, etc.), the ΔG 's may decrease (or become negative) due to their instabilities,¹⁵⁸ and the rough estimation above suggests that the dependency of k to T may vary at certain circumstances (To be discussed in **Chapter 7**).

6.8 XPS and SEM-EDX Analyses

To determine the compounds formed during the adsorptions, XPS analyses were performed using, fresh Ag⁰-Aerogel, 350 °C degassed Ag⁰-Aerogel, CH₃I fully loaded (9585 ppbv, powdered adsorbent) Ag⁰-Aerogel, I₂ fully loaded (50 ppmv, powdered adsorbent) Ag⁰-Aerogel, 104 ppbv CH₃I adsorbed (partially loaded) Ag⁰-Aerogel at 100, 150 and 200 °C, and 1044 ppbv CH₃I adsorbed (partially loaded) Ag⁰-Aerogel at the same temperatures. Since the first scan of the 104 ppbv/200 °C was questionable, a rescan was performed using the identical sample and settings (marked as SC1 and SC2 in the spectra).

The XPS analyses were performed using the Scienta Omicron ESCA-2SR at Cornell University. The operating pressure is 1×10^{-9} Torr, and the monochromatic Al K α x-rays (1486.6 eV) were generated at 300W (15 kV; 20mA).

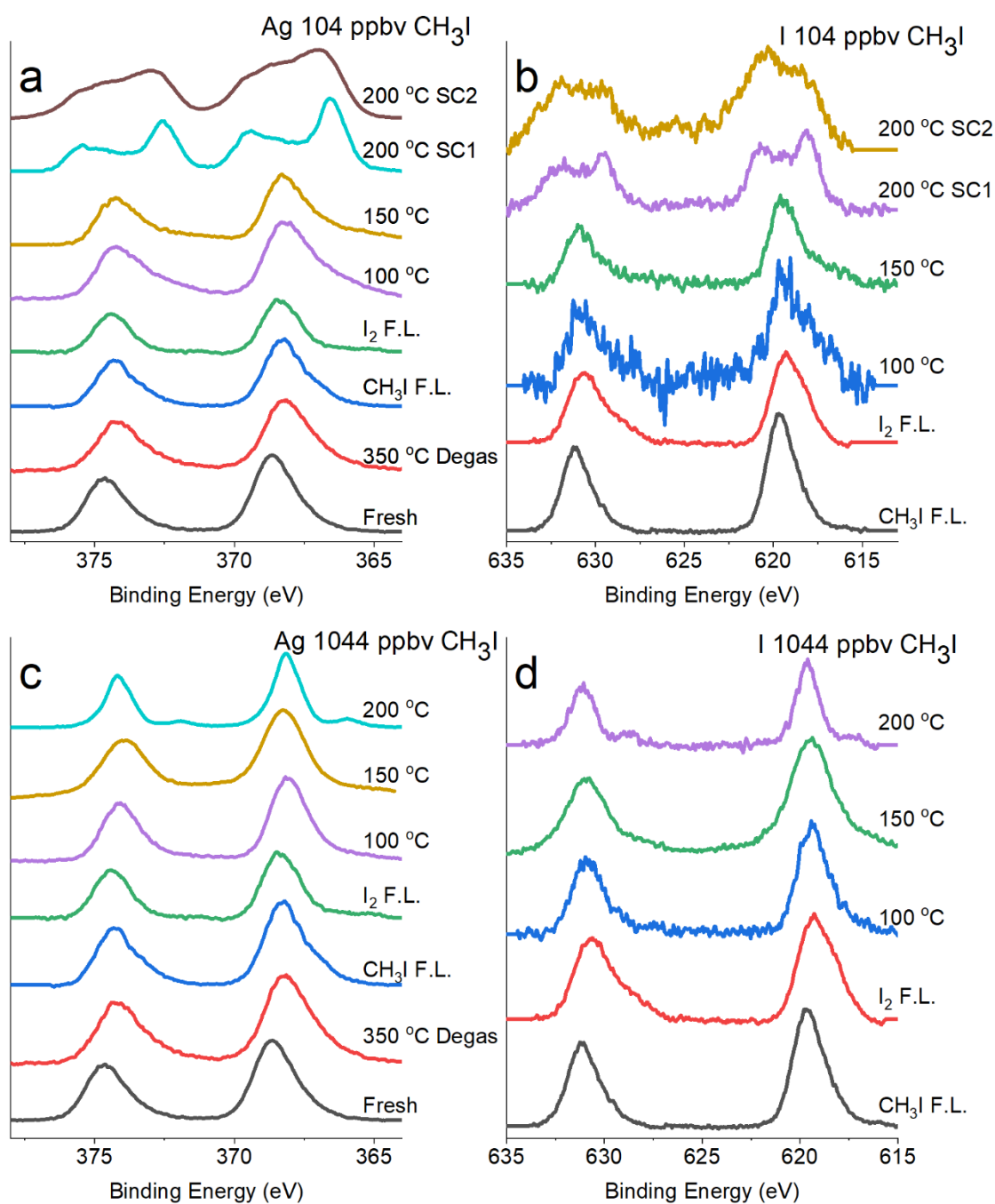


Figure 6-9. Regional scans of Ag (a), I (b) XPS spectra of 104 ppbv CH₃I adsorbed Ag⁰-Aerogel and Ag (c), I(d) of 1044 ppbv CH₃I adsorbed Ag⁰-Aerogel, with fresh, 350 °C degassed, CH₃I fully loaded at 150 °C and I₂ fully loaded Ag⁰-Aerogel at 150 °C as references.

The XPS spectra collected are shown in Figure 6-9. The fresh Ag⁰-Aerogel obtains the Ag3d_{5/2} peak located at approximately 368.6 eV and the Ag3d_{3/2} peak at approximately 374.6 eV, which are comparable to the binding energy (BE) reported by Matyáš et al.⁶⁵ After being degassed at 350 °C, the Ag BE decreases to 368.1 and 374.1 eV, indicating that certain amount of Ag₂S nanoparticles may be generated in this process.^{159,160} After reacting with CH₃I at different concentrations and temperatures, most of the Ag peaks shift to approximately 368.2 and 374.2 eV except those of the pellets at 104 ppbv/ 200 °C condition. The trend of iodine BE is slightly different from that of Ag, CH₃I fully loaded sample contains the I3d_{5/2} and I3d_{3/2} peaks at approximately 619.6 and 631.1 eV respectively, I₂ fully loaded sample contains I3d_{5/2} and I3d_{3/2} peaks at approximately 619.3 and 630.8 eV, and the peaks of remaining CH₃I reacted samples located in between the values above except the 104 ppbv/ 200 °C case.

However, the spectra of the 104 ppbv/200 °C CH₃I adsorbed Ag⁰-Aerogel are significantly different. Both Ag3d_{5/2} and Ag3d_{3/2} split to at least two peaks, locating at approximately 366.6, 369.5, 372.6 and 375.5 eV and I3d_{5/2} and I3d_{3/2} at 618.1, 620.9, 629.6 and 632.4 eV. The variations of the Ag and I spectra at 104 ppbv/ 200 °C condition indicate the Ag-I compounds formed may be different.

The SEM-EDX analyses were also conducted to measure the element compositions and potential structure changes on the pellet surface. The SEM-EDX analyses were performed using JEOL JSM IT100LA at SUNY College of Environmental Science and Forestry (SUNY-ESF). The acceleration voltage was 10-15 kV and the probe current is 20-30 nA for secondary electron

detector (SED) mode and 55-65 mA for backscattered electron composition (BEC) mode.

The SED and BEC (including the corresponding mappings of Ag and I) images are shown in Figure 6-10. The images show that the fresh Ag^0 -Aerogel (a) does not contain any notable Ag clusters in the micrometer scale on the surface. After reacting with 104 ppbv (b) and 1044 ppbv (c) CH_3I (partially loaded), the surfaces of the adsorbent become coarser, whereas the distributions of Ag and I remain relatively uniform. As the concentration of the adsorbate increases, certain surface structures were formed and some bright spots can be observed in the SED image of the 9585 ppbv CH_3I fully loaded Ag^0 -Aerogel(d). Similar bright spots were also identified in the BEC image and the corresponding Ag and I mappings. In the Ag and I mapping, a large bright spot exists on the top of the images and at least two other spots locate in the middle and the bottom-right corner. Therefore, the bright spots on the surface of CH_3I fully loaded samples appear to be AgI clusters.

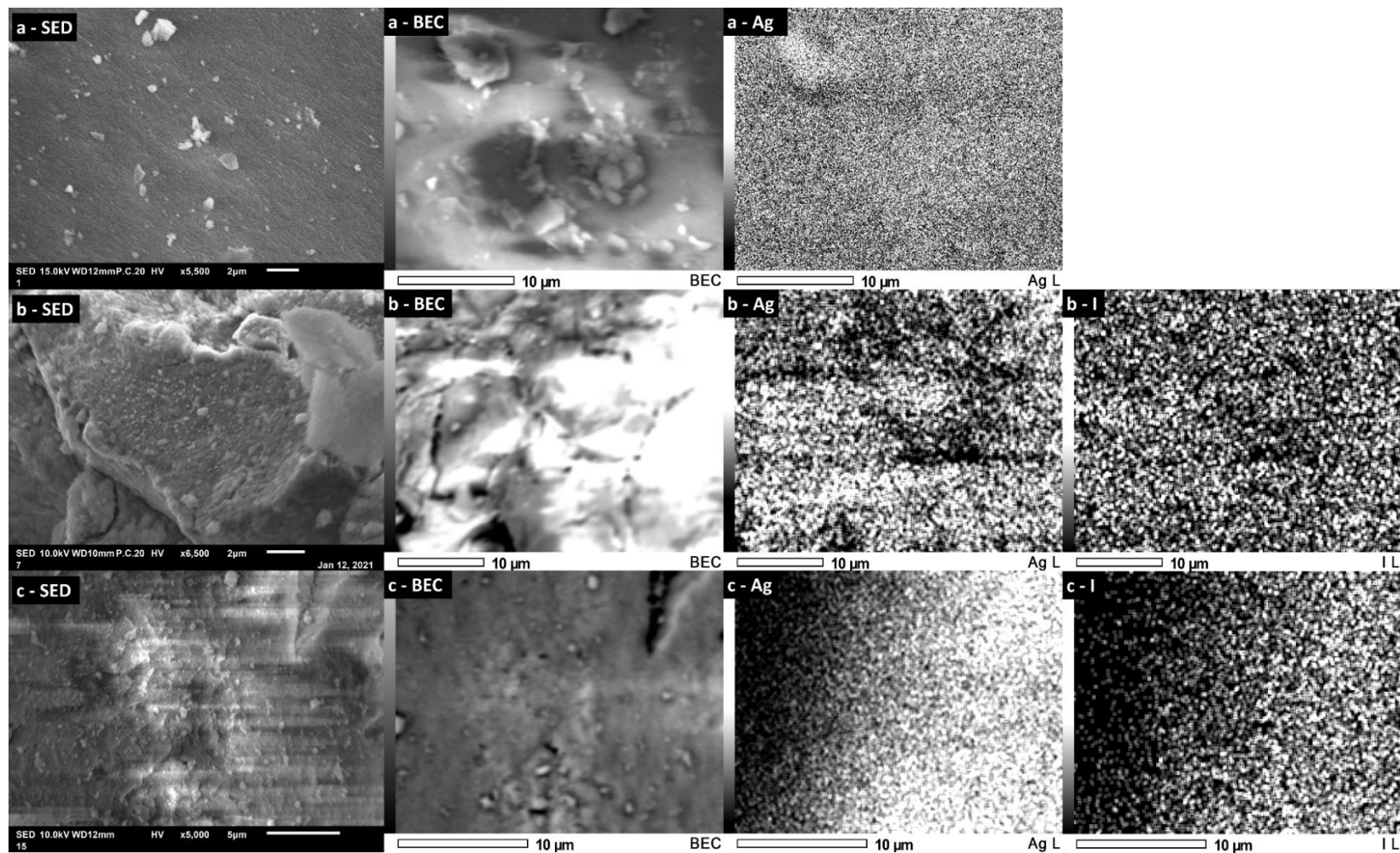


Figure 6-10. The SEM images including SED, BEC, Ag mapping and I mapping of various Ag⁰-Aerogels: (a) fresh, (b) 104 ppbv/150 °C CH₃I partially loaded, (c) 1044 ppbv/150 °C CH₃I partially loaded, (d) 9585 ppbv/150 °C CH₃I fully loaded and (e) 50 ppmv /150 °C I₂ fully loaded. (Continue in the next page)

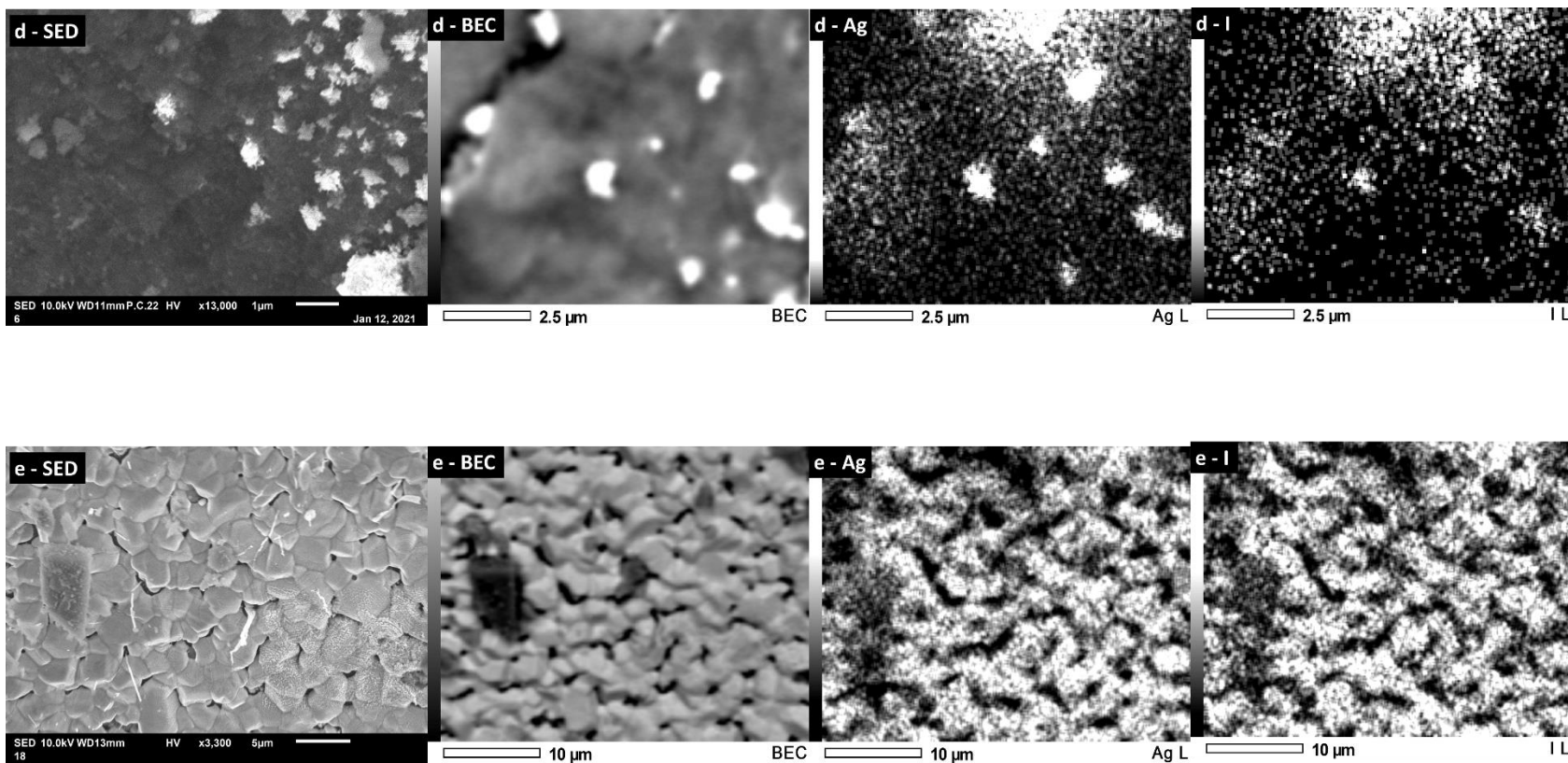


Figure 6-10. The SEM images including SED, BEC, Ag mapping and I mapping of various Ag⁰-Aerogels: (a) fresh, (b) 104 ppbv/150 °C CH₃I partially loaded, (c) 1044 ppbv/150 °C CH₃I partially loaded, (d) 9585 ppbv/150 °C CH₃I fully loaded and (e) 50 ppmv /150 °C I₂ fully loaded.

The change of surface structure is more significant for the 50 ppmv I₂ fully loaded sample (e). In the images, an obvious pattern can be identified, indicating a layer of AgI formed during the adsorption. The AgI clusters are in polygon shape and the diameter of the clusters are approximately 1-5 μm.

6.9 Surface Composition

Observed in the XPS results (Figure 6-9), the spectra of 104 ppbv/ 200 °C CH₃I adsorbed Ag⁰-Aerogel are significantly different from all others, which may further explain the abnormal high uptake rate. Figure 6-11 is the Ag(a) and I(b) regional scans of the 104 ppbv/200 °C CH₃I adsorbed pellets with the spectra of CH₃I fully loaded sample as references. Both Ag and I spectra of 104 ppbv/ 200°C sample consist of three groups of peaks, which are marked as 1, 2 and 3 in the figure. For Ag spectrum, 3 Ag3d_{5/2} peaks are located at 366.6, 368.2 and 369.45 eV, which the second group is well agreed with the peaks of CH₃I fully loaded sample. Similarly, the I spectrum also contains 3 groups of peaks and the binding energies of the second group are close to those of the fully loaded sample. The compositions of three groups of peaks were also determined, and the results are, approximately 52-55%, 15-20% and 28-29% for group 1, 2 and 3 respectively. Since the compositions acquired in both fittings are relatively similar, the additional peaks appear to be some form of Ag-I (not AgI, silver iodide) compounds.

Reported in multiple studies,¹⁶¹⁻¹⁶⁵ the Ag BE tends to decrease as the oxidation state increases.

For example, the Ag3d_{5/2} BE of metallic Ag is approximately 368.1 eV, and this value decreases

to 367.7-367.9 eV for Ag^+ and 367.3-367.6 eV for Ag^{2+} . Admittedly, the instrument deviations and data calibration standards may vary the BE measured, but the trend indicates that a certain amount of Ag^{2+} may be formed in 104 ppbv CH_3I adsorption at 200 °C, whereas the peak group 3 remains questionable.

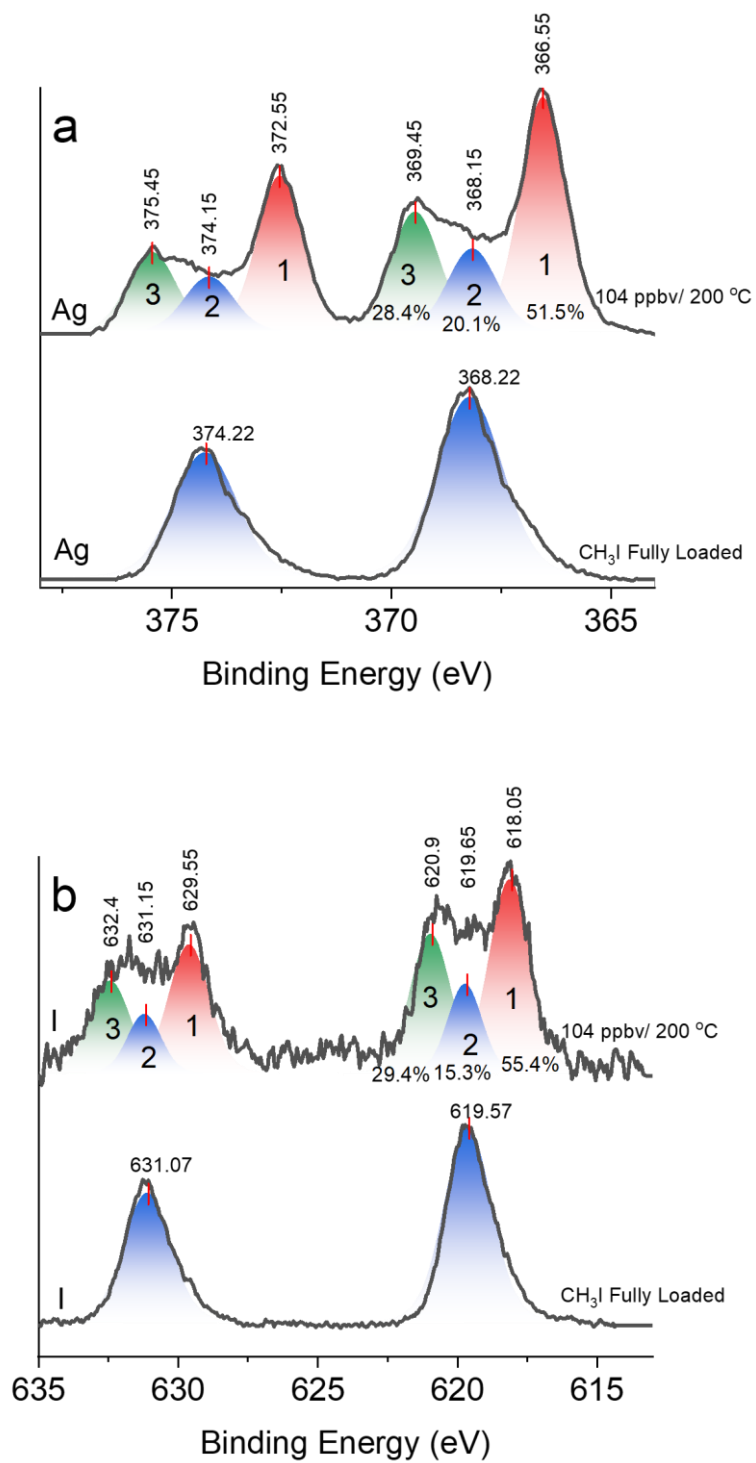


Figure 6-11. The regional scans of Ag(a), I(b) and the curve fits of the 104 ppbv/ 200 °C

CH₃I adsorbed Ag⁰-Aerogel.

The Ag and I concentrations can be interpreted from the XPS and SEM-EDX spectra, where the results are listed in Table 6-2. To compare the iodine concentrations between samples, the iodine compositions have been calibrated as additional mass, which the summations of all other elements are 100%. It is important to noticed that the Ag⁰-Aerogel is a highly heterogeneous material; the Ag coverage on the pellets is uneven, and the values measured by SEM-EDX and XPS may vary based on the specific location scanned.

Both SEM-EDX and XPS are the surface analysis techniques whereas the penetration depth of XPS is approximately 5-10 nm and that of SEM-EDX is 1-10 μm .^{166,167} Therefore, the higher iodine compositions for partially loaded Ag⁰-Aerogel observed by XPS indicate the existence of a strong concentration gradient in the pellet during the CH₃I adsorption. Additionally, it can also be visualized that the concentrations of I on the surface are much higher than the experimental measured iodine uptakes (same as CH₃I uptake, assuming CH₃ group diffuse out in C₂H₆ form), which further supports the existence of the surface reaction proposed in **Chapter 5**.

Conditions	Temperature (°C)	SEM-EDX				XPS				Iodine Uptake (wt%)
		Ag (wt%)	I (wt%)	I:Ag ⁽²⁾ (mol)	I:Ag ⁽³⁾ (wt)	Ag (wt%)	I (wt%)	I:Ag ⁽²⁾ (mol)	I:Ag ⁽³⁾ (wt)	
Fresh		31.5				33.7				
350 °C Degas		34.0				30.2				
CH ₃ I F.L. ⁽¹⁾	150	29.1	32.3	0.94	1.11	29.2	28.3	0.82	0.97	28.31
I ₂ F.L. ⁽¹⁾	150	--	--	--	--	26.9	27.1	0.86	1.01	37.24
104 ppb	100	39.0	0.9	0.02	0.02	27.7	1.8	0.05	0.06	0.29
	150	38.5	1.2	0.03	0.03	28.0	2.5	0.08	0.09	0.39
	200	41.9	2.6	0.05	0.06	28.7	5.8	0.17	0.20	1.15
1044 ppb	100	40.6	4.8	0.10	0.12	27.9	6.0	0.18	0.21	2.84
	150	34.3	5.0	0.12	0.15	27.8	12.4	0.38	0.45	3.71
	200	47.9	6.4	0.11	0.13	33.1	13.1	0.34	0.40	4.31

(1) Fully Loaded

(2) Molar ratio of I and Ag

(3) Mass ratio of I and Ag

Table 6-2. The Ag and I concentrations measured by SEM-EDX and XPS (I compositions have been calibrated as additional mass).

6.10 Explanation for the Additional Mass Uptake

Shown in Figure 6-1a, the mass uptake rate at 200 °C was approximately 3 times higher than that at 150 °C, and the mass uptake by 12 days increased from 0.39 wt% to 1.15 wt%. What is the additional mass? To explain this question, some theoretical analyses were performed and listed below.

Firstly, if the additional mass is not iodine, what could it be? According to the manufacturer, except N₂ and O₂, the carrier gas (Air, Airgas, Ultra Zero) of CH₃I used in adsorption experiments contains CO and CO₂ with a combining concentration less than 1 ppmv. Reported in previous studies, silver was used as catalyst in CO and CO₂ oxidation/reduction¹⁶⁸⁻¹⁷¹, and it may capture CO and CO₂^{172,173}. However, since the Ag⁰-Aerogel does not satisfy the requirement for catalyzing the impurities and the physical capturing of the CO and CO₂ does not require CH₃I, which implies that the physisorption should have happened during the drying process. Therefore, the abnormal mass increase caused by reaction between silver and impurities in carrier gas may be excluded.

Another possibility is that the Ag is oxidized by O₂ in the carrier gas and the additional mass is the result of oxidation. However, had the oxidation been the reason, the mass uptake should have been observed in the drying process and not only at 200 °C-104 ppbv condition, as the 'CH₃I induced' oxidation of Ag was not reported in literature. Therefore, the additional mass appears to be iodine. The surface compositions measured by XPS and SEM-EDX further support the conclusion. Shown in Table 6-2, the iodine fraction at 200 °C-104 ppbv condition is much higher

than that at 150 °C, indicating the abnormal mass gain is likely to be iodine.

6.11 Conclusions and Recommendations

Traditionally, after the adsorption, Ag⁰-Aerogel will be consolidated by compressing at high temperature, and removing the organic moieties at 350 °C before compressing benefits the consolidation results (higher product density and lower porosity).¹⁴⁹ In this presented work, a novel pre-treating method was applied. The Ag⁰-Aerogel was vacuum dried at 350 °C before the CH₃I adsorption to remove the organic moieties, and the uptake rate and maximum iodine adsorption capacity remain similar to the untreated one. Therefore, removing the organic moieties before the adsorption could be a practicable alternative, and the potential iodine contamination during the traditional organic moieties removing process could be avoided.

In the 104 and 1044 ppbv CH₃I adsorptions on Ag⁰-Aerogel at 100, 150 and 200 °C, an abnormal behavior was observed in 104 ppbv adsorption at 200 °C; the uptake rate was approximately 3 – 4 times higher than those of 100 and 150 °C adsorptions at the same concentration. The most intuitive explanation is the well-known Arrhenius relationship, the increase of temperature results in the increase of reaction rate and diffusivity.

Additionally, more potential explanations are proposed based on successive experimental and theoretical analyses. The nitrogen adsorption analyses were performed using the pellets at different drying conditions, and the results indicated that the increasing temperature decreases the water concentration in the pellet and therefore may increase the silver sites availability and the pore diffusivities of CH₃I and the gas form product. The gas form product, believed to be

C₂H₆, is considered as a ‘diffusion limitation’ for the adsorption process in the proposed reaction pathway, and the increase of its diffusivity may vary the reaction rate in another perspective.

Moreover, the XPS and SEM-EDX analyses were also performed and the results indicated that at 104 ppbv/ 200°C condition, some additional Ag-I compounds were generated. By comparing the binding energies of the peaks with previous studies, we presumed that the additional Ag-I compounds may contain a certain amount of Ag²⁺. However, identifying the peak group 3 in Figure 6-11 remains unsolved. To further determine the composition formed in CH₃I adsorption process, performing additional physical analyses such as regional scans of other elements in XPS, x-ray absorption spectroscopy (XAS) and Raman spectroscopy are recommended.

In the presented work, we observed an unusually high uptake rate for 104 ppbv CH₃I adsorption on Ag⁰-Aerogel at 200 °C, and suggested multiple explanations for this behavior. Our discoveries offer a new perspective in determining the optimum temperature for CH₃I adsorptions, whereas a commonly used temperature is 150 °C. However, for the purpose of carefulness and accuracy, we may not recommend 200 °C as the optimum adsorption temperature until further evidence has been revealed.

Chapter 7. Adsorption of Other Iodoalkanes

7.1 Introduction

In previous chapters, the temperature and concentration dependence of the CH₃I adsorptions on Ag⁰-Aerogel were examined. The CH₃I adsorptions at 150 °C are identified as an nth order shrinking core process. As the temperature increases, the reaction rate increases orderly, whereas an abnormal increase of reaction rate was observed at the CH₃I-104 ppbv-200 °C condition. To further analyze the reaction behavior of other iodoalkanes, the adsorptions of C₃H₇I, C₆H₁₃I, C₈H₁₇I and C₁₂H₂₅I were performed using the continuous flow adsorption system. The concentrations used include, C₃H₇I-96 ppbv, C₆H₁₃I-101 ppbv, C₆H₁₃I-733 ppbv, C₈H₁₇I-60 ppbv, C₁₂H₂₅I-113 ppbv and C₁₂H₂₅I-606 ppbv. The temperature dependences were studied for C₆H₁₃I and C₁₂H₂₅I at all four concentrations by performing the experiments at 100, 150 and 200 °C. The flow rate used is 500 sccm.

In the experiments performed, it was observed that the adsorption behaviors were much more unstable than those of CH₃I. Both the concentration dependency and the temperature dependency are different. To provide reliable conclusions, multiple repeats were performed and the results are presented in following sections.

7.2 Adsorption Kinetics

Since the repeatabilities of the C₃H₇I to C₁₂H₂₅I adsorptions are relatively poor compared with that of the CH₃I, multiple repeats were performed and all experiments appeared to be reasonable

are shown in Figure 7-1. At 100 - 200 °C, in approximately 300 h, the mass uptakes of C₆H₁₃I-101 ppbv adsorptions reached approximately 0.5 – 1 wt% and those of C₁₂H₂₅I-113 ppbv adsorptions reached 0.3-0.8 wt%. Unlike the CH₃I adsorptions, the mass uptakes are roughly proportional to the concentrations (104 ppbv-0.39 wt%, 245 ppbv-0.91 wt%, 1044 ppbv-3.7 wt% and 9584 ppbv-14.7 wt%), the mass uptakes of C₆H₁₃I-733 ppbv and C₁₂H₂₅I- 606 ppbv were relatively similar to those of the adsorptions at approximately 100 ppbv. The C₆H₁₃I-733 ppbv mass uptakes were 0.5-1.0 wt% and the C₁₂H₂₅I- 606 ppbv mass uptakes were 0.4-1.4 wt%, which indicates that the adsorption rates are relatively independent of the adsorbate concentrations.

Moreover, with lower concentrations, the C₃H₇I and C₈H₁₇I adsorption rates increased instead. The mass uptake of C₃H₇I-96 ppbv adsorption reached 1.6 wt% and that of C₈H₁₇I-60 ppbv reached 0.8 wt%. By repeating the adsorptions, the abnormal increases of the uptake rates for C₃H₇I-96 ppbv and C₈H₁₇I-60 ppbv were confirmed. To further analyze the data, the shrinking core model (SCM) was used in the data fitting and the results are shown in following sections.

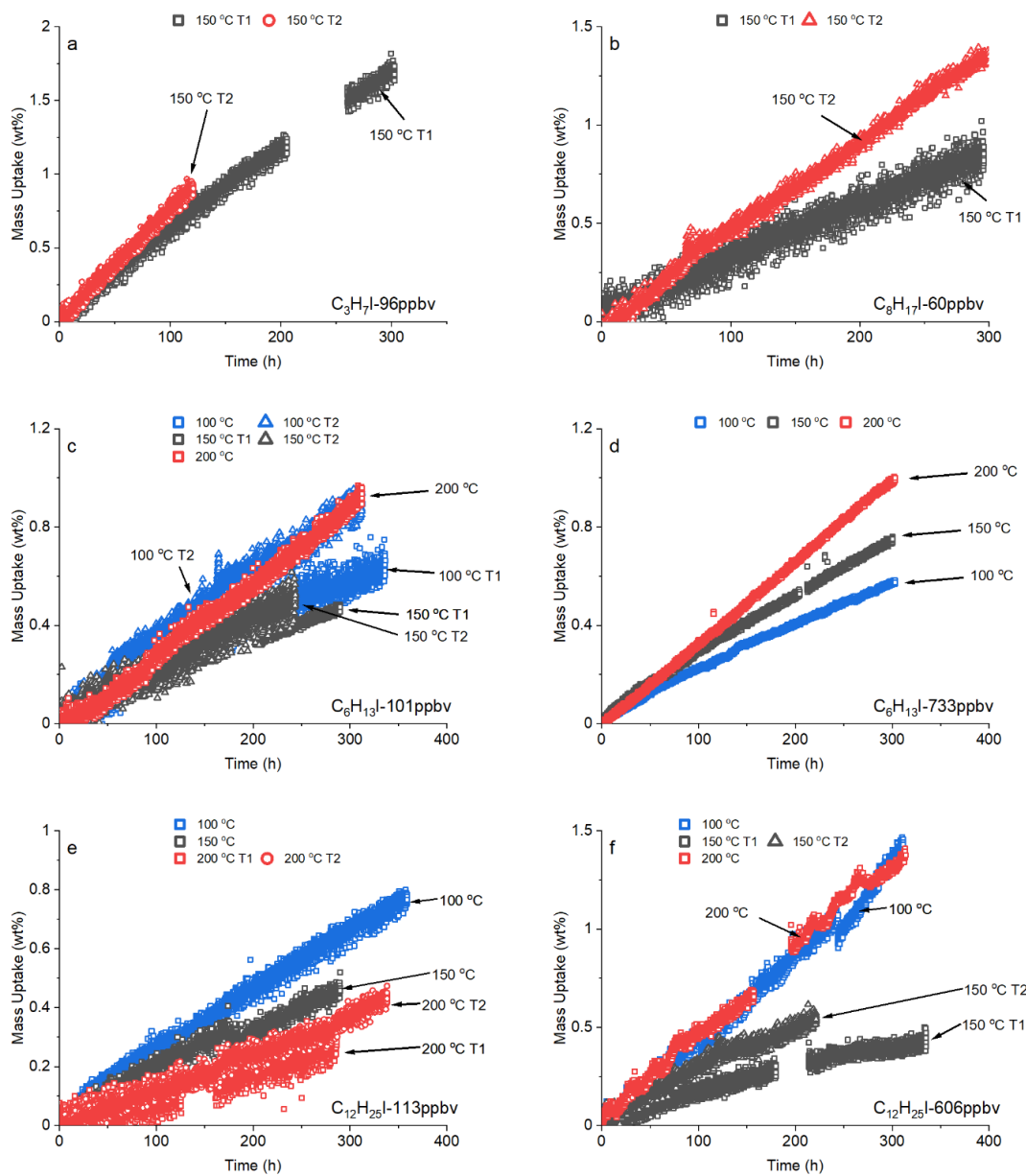


Figure 7-1. The adsorption kinetics at 100, 150 and 200 °C, (a) C_3H_7I -96 ppbv, (b) $C_8H_{17}I$ -60 ppbv, (c) $C_6H_{13}I$ -101 ppbv, (d) $C_6H_{13}I$ -733 ppbv, (e) $C_{12}H_{25}I$ -113 ppbv, (f) $C_{12}H_{25}I$ -606 ppbv. (T1 and T2 represent different experimental trials)

7.3 Shrinking Core Model Fitting

A preliminary SCM fitting was performed and the D_p ranged from 10^{-5} to 10^5 cm²/s, which is because that the mass uptakes of the adsorption are relatively low (generally under 1.5 wt%), and acquiring accurate diffusivities using the SCM is impracticable. Therefore, two additional methods were used. The first method is estimating the values of D_p 's and calculating the reaction rate constant k_s and the second method is ignoring the pore diffusivity term and only fitting the reaction term.

7.3.1 Estimating the Gas Film Diffusivity and Pore Diffusivity

Same as the CH₃I adsorption, the binary diffusivities (D_{AB}) and the gas film diffusivities (k_f) can be estimated using Eq. 3-11 to 3-14. Using the data suggested by Fuller et al.,¹²⁹ the diffusion volume (v) of organic iodide is the summation of the diffusion volumes of the alkyl group and the iodine atom. The values are 52.63, 93.67, 155.23, 196.27, 278.35 cm³, for CH₃I, C₃H₇I, C₆H₁₃I, C₈H₁₇I and C₁₂H₂₅I, respectively. The D_{AB} 's of the organic iodides range from 0.196 to 0.073 cm²/s. According to Currie,¹⁵³ D_p is related to D_{AB} by the pellet porosity (ϵ_p),

$$D_p / D_{AB} = \epsilon_p^m \quad 7-1$$

where m is generally between 2 – 4.5. Assuming ϵ_p and m are constant for the organic iodides adsorptions on Ag⁰-Aerogel, the relationship between D_p and D_{AB} can be written as,

$$\frac{D_p}{D_p'} = \frac{D_{AB}}{D_{AB}'} \quad 7-2$$

For the CH₃I, at 150 °C, the D_{AB} of 0.196 cm²/s and the average D_p of 6.70×10^{-4} cm²/s were calculated in **Section 5.4**. The k_f 's and D_p 's of other organic iodides at 100, 150, 200 °C can be therefore approximated using Eq. 7-2 and the results are listed in Table 7-1.

Organic Iodides	Temperature (°C)	ν (cm ³)	D_{AB} (cm ² /s)	k_f (cm/s)	D_p (cm ² /s)
CH ₃ I	150	52.63	0.196	2.71	6.70×10^{-4}
C ₃ H ₇ I	150	93.67	0.153	2.17	5.24×10^{-4}
C ₆ H ₁₃ I	100		0.097	1.43	3.33×10^{-4}
	150	155.23	0.121	1.76	4.15×10^{-4}
	200		0.147	2.11	5.05×10^{-4}
C ₈ H ₁₇ I	150	196.27	0.108	1.59	3.71×10^{-4}
	100		0.073	1.12	2.52×10^{-4}
C ₁₂ H ₂₅ I	150	278.35	0.092	1.37	3.14×10^{-4}
	200		0.111	1.64	3.81×10^{-4}

Table 7-1. The estimated k_f 's and D_p 's for the organic iodides adsorptions at 100, 150 and 200 °C.

7.3.2 Model Fitting Results

The SCM fitting results of C₃H₇I, C₆H₁₃I, C₈H₁₇I and C₁₂H₂₅I adsorptions using three methods, full SCM, full SCM and estimated D_p , and the SCM with only gas film diffusion and reaction terms are listed in Table 7-2.

Conc (ppbv)	Temp (°C)	Avg Ads Rate (wt%/h)	Full SCM				Full SCM + Estimated D_p				Gas Film Diff + Reaction		
			k_f^* (cm/s)	D_p (cm ² /s)	k_s (cm/s)	AARD (%)	k_f^* (cm/s)	D_p^* (cm ² /s)	k_s (cm/s)	AARD (%)	k_f^* (cm/s)	k_s (cm/s)	AARD (%)
C₃H₇I													
96	150 T1	5.65×10 ⁻³	2.17	1.94×10 ⁻²	1.703	4.14%	2.17	5.24×10 ⁻⁴	7.507	20.57%	2.17	1.651	4.58%
	150 T2	7.59×10 ⁻³	2.17	1.80×10 ⁻²	2.474	12.37%	2.17	5.24×10 ⁻⁴	9.561	26.47%	2.17	2.474	12.37%
C₆H₁₃I													
101	100 T1	1.90×10 ⁻³	1.43	4.70×10 ⁻⁴	0.394	8.73%	1.43	3.33×10 ⁻⁴	0.416	8.73%	1.43	0.348	9.94%
	100 T2	2.78×10 ⁻³	1.43	4.61×10 ⁻⁴	0.883	9.30%	1.43	3.33×10 ⁻⁴	1.028	10.41%	1.43	0.622	12.26%
	150 T1	1.51×10 ⁻³	1.76	1.19×10 ⁻⁴	0.491	6.90%	1.76	4.15×10 ⁻⁴	0.375	10.65%	1.76	0.338	14.08%
	150 T2	2.02×10 ⁻³	1.76	2.60×10 ⁻⁴	0.528	14.75%	1.76	4.15×10 ⁻⁴	0.504	15.83%	1.76	0.437	17.54%
	200	3.01×10 ⁻³	2.11	4.94×10 ⁻⁵	0.525	12.84%	2.11	5.05×10 ⁻⁴	0.631	18.48%	2.11	0.525	12.84%
	100	1.85×10 ⁻³	1.43	2.70×10 ⁻⁵	0.051	4.77%	1.43	3.33×10 ⁻⁴	0.041	9.50%	1.43	0.040	10.27%
733	150	2.38×10 ⁻³	1.76	4.00×10 ⁻⁵	0.084	5.57%	1.76	4.15×10 ⁻⁴	0.063	10.67%	1.76	0.061	11.81%
	200	3.34×10 ⁻³	2.11	3.18×10 ⁻⁵	0.076	3.17%	2.11	5.05×10 ⁻⁴	0.078	4.51%	2.11	0.076	3.17%

*Calculated theoretically

Table 7-2. The shrinking core model parameters determined for C₃H₇I, C₆H₁₃I, C₈H₁₇I and C₁₂H₂₅I adsorptions on Ag⁰-Aerogel at 100, 150 and 200°C. (Continue in the next page).

Conc (ppbv)	Temp (°C)	Avg Ads Rate (wt%/h)	Full SCM				Full SCM + Estimated D_p				Gas Film Diff + Reaction		
			k_f^* (cm/s)	D_p (cm ² /s)	k_s (cm/s)	AARD (%)	k_f^* (cm/s)	D_p^* (cm ² /s)	k_s (cm/s)	AARD (%)	k_f^* (cm/s)	k_s (cm/s)	AARD (%)
C₈H₁₇I													
60	150 T1	2.80×10 ⁻³	1.59	7.20×10 ⁻⁴	3.190	15.74%	1.59	3.71×10 ⁻⁴	9.382	19.35%	1.59	1.697	17.48%
	150 T2	4.64×10 ⁻³	1.59	7.79×10 ⁻⁴	3.562	14.03%	1.59	3.71×10 ⁻⁴	21.818	40.80%	1.59	3.563	14.04%
C₁₂H₂₅I													
113	100	2.09×10 ⁻³	1.12	2.63×10 ⁻⁴	0.517	2.22%	1.12	2.52×10 ⁻⁴	0.525	2.21%	1.12	0.379	3.15%
	150	1.46×10 ⁻³	1.37	9.02×10 ⁻⁵	0.476	5.12%	1.37	3.14×10 ⁻⁴	0.340	2.50%	1.37	0.301	4.44%
	200 T1	0.96×10 ⁻³	1.64	3.41×10 ⁻⁵	0.149	16.95%	1.64	3.81×10 ⁻⁴	0.152	17.07%	1.64	0.149	16.95%
	200 T2	1.25×10 ⁻³	1.64	4.20×10 ⁻⁵	0.182	19.61%	1.64	3.81×10 ⁻⁴	0.189	21.04%	1.64	0.182	19.61%
606	100	4.34×10 ⁻³	1.12	1.50×10 ⁻³	0.104	7.05%	1.12	2.52×10 ⁻⁴	0.116	9.36%	1.12	0.102	6.82%
	150 T1	1.26×10 ⁻³	1.37	2.26×10 ⁻⁵	0.048	10.50%	1.37	3.14×10 ⁻⁴	0.040	13.20%	1.37	0.039	13.64%
	150 T2	2.31×10 ⁻³	1.37	3.44×10 ⁻⁵	0.108	7.57%	1.37	3.14×10 ⁻⁴	0.079	11.23%	1.37	0.076	12.36%
	200	4.35×10 ⁻³	1.64	1.66×10 ⁻⁴	0.193	13.25%	1.64	3.81×10 ⁻⁴	0.168	11.76%	1.64	0.151	13.65%

*Calculated theoretically

Table 7-2. The shrinking core model parameters determined for C₃H₇I, C₆H₁₃I, C₈H₁₇I and C₁₂H₂₅I adsorptions on Ag⁰-Aerogel at 100, 150 and 200°C. (T1 and T2 represent different experimental trials)

The fitting result of $C_8H_{17}I$ -T1 adsorption is a good example to compare the three different methods. Shown in Figure 7-2, the full SCM method results in the closest fitting, but the D_p determined may not be reasonable (e.g., the ones in 10^{-5} or 10^5 cm^2/s) and the corresponding k_s 's at different conditions may not be comparable. To make the results determined comparable, the method of full SCM with estimated D_p was applied. It is suitable for some cases but may result in overfitting. For example, when applying this method in the $C_8H_{17}I$ adsorption, the k_s is much higher than the k_s 's determined using the other two methods (marked in red in Figure 7-2).

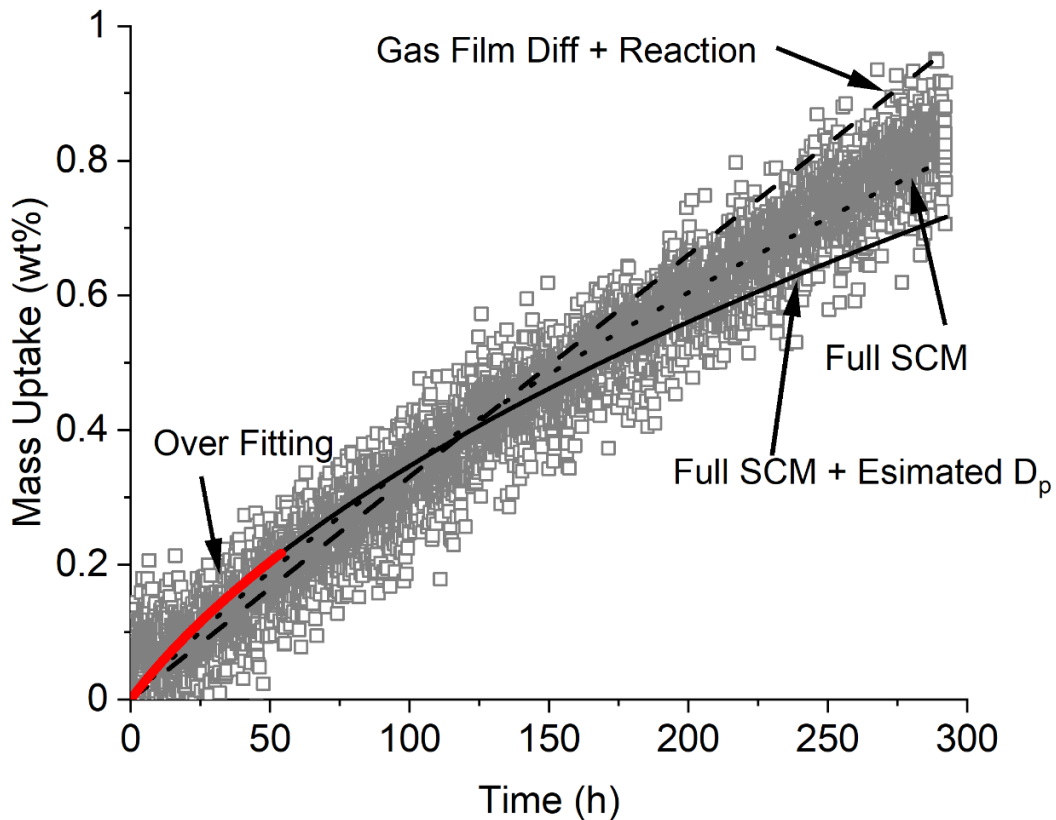


Figure 7-2. The $C_8H_{17}I$ -60 ppbv-T1 adsorption kinetics and the fitting results of the three methods.

Since the adsorption in the initial portion of the overall process is mainly controlled by the reaction term, using only gas film diffusion and reaction terms in the SCM is adequate to describe the data acquired. The results are reasonable, no over fitting occur, and more importantly, the parameters determined are comparable. Therefore, the SCM with only gas film diffusion term and the reaction term was selected to be the optimum method and the results are used in following analyses.

7.4 Concentration Dependence

Visualized in Figure 7-1 and Table 7-2, the adsorption rates are roughly independent of the adsorbate concentrations. Discussed in **Section 3.2**, the concentrations of $C_6H_{13}I$ and $C_{12}H_{25}I$ are much lower than their vapor pressures, indicating that the actual concentrations were not limited by the condensations of the organic iodides. In other words, the actual concentrations of $C_6H_{13}I$ and $C_{12}H_{25}I$ should be the same as the calculated concentrations (733 and 606 ppbv), since no condensations occurred.

Another possibility is that the rate limiting step changes in the $C_6H_{13}I$ and $C_{12}H_{25}I$ adsorptions. In **Section 5.7**, the reaction between CH_3I and Ag^0 -Aerogel was identified as the rate limiting step for the low-concentration CH_3I adsorption in a relatively short period and a potential reaction pathway was suggested in **Section 5.8**. Similar to Figure 5-10 but more generally, the reaction between organic iodides and Ag may be written as Figure 7-3.

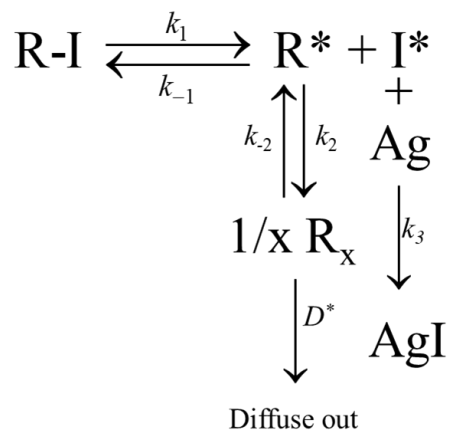


Figure 7-3. A general reaction pathway between iodoalkanes and Ag.

R-I denotes the organic iodide, R is the alkyl group and R_x is the potential product. For the $C_6H_{13}I$ and $C_{12}H_{25}I$ adsorptions, if the rate limiting step in the reaction becomes independent of the adsorbate concentration, the overall adsorption may become the same.

A hypothesis could be that the surface reaction of iodoalkane is the rate limiting step and the binding of the molecules to the sites is relatively fast. Therefore, the ‘concentration available for reaction’ is actually limited by the number of sites, and, in the macroscale, the reaction rate becomes independent of the bulk adsorbate concentration. This hypothesis is supported by the Langmuir adsorption model.^{174,175} The reaction rate may be expressed as,

$$r = k \frac{K_L C}{1 + K_L C} \tag{7-3}$$

where K_L is the Langmuir surface adsorption equilibrium constant and r , k and C are general reaction rate, reaction rate constant and concentration, respectively. When $K_L C \gg 1$, the reaction rate may become independent with the bulk adsorbate concentration.

7.5 Temperature Dependence

Unlike the CH_3I adsorptions, which the uptake rate increases orderly with the increasing temperature, the data collected for the $\text{C}_6\text{H}_{13}\text{I}$ and $\text{C}_{12}\text{H}_{25}\text{I}$ adsorptions do not obtain clear and constant tendencies. In Figure 7-1, it is observed that, for the $\text{C}_6\text{H}_{13}\text{I}$ -733 ppbv adsorption, the reaction rate increases with increasing temperature, and the dependency reverses for the $\text{C}_{12}\text{H}_{25}\text{I}$ -113 ppbv adsorption. As for the $\text{C}_6\text{H}_{13}\text{I}$ -101 ppbv and $\text{C}_{12}\text{H}_{25}\text{I}$ -606 ppbv adsorptions, it appears that the adsorption rates at both 100 and 200 °C are higher than that at 150 °C.

For the $\text{C}_6\text{H}_{13}\text{I}$ -733 ppbv and $\text{C}_{12}\text{H}_{25}\text{I}$ -113 ppbv adsorptions, the Arrhenius relationships were determined using Eq. 6-7 and the results are plotted in Figure 7-4. The activation energy ΔE 's are 9.44 kJ/mol and -12.56 kJ/mol and the pre-exponential factor k_s^0 's are 1.17 cm/s and 7.13×10^{-3} cm/s for $\text{C}_6\text{H}_{13}\text{I}$ -733 ppbv and $\text{C}_{12}\text{H}_{25}\text{I}$ -113 ppbv adsorptions respectively.

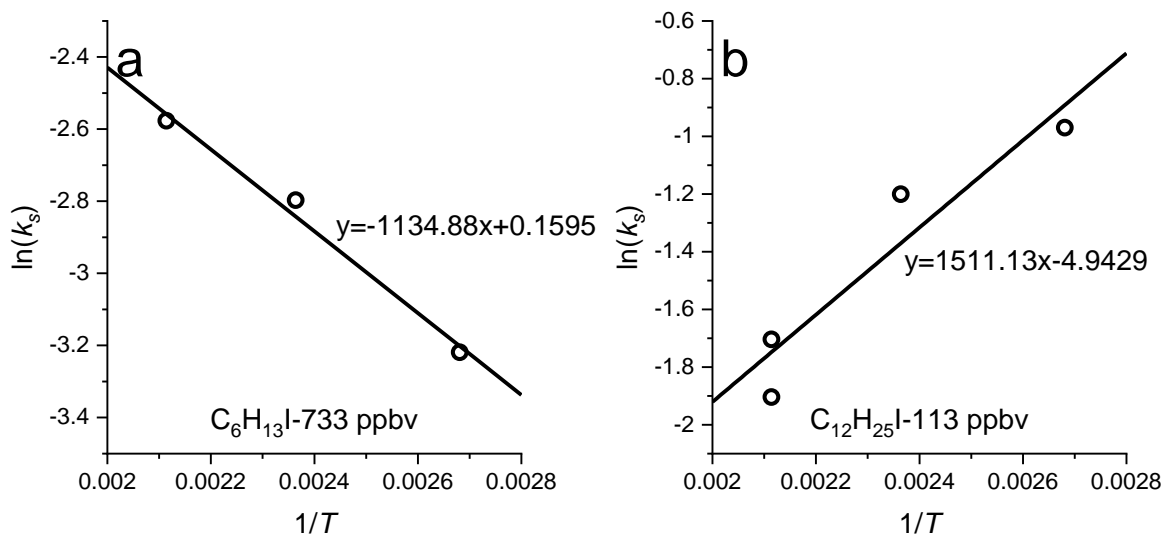


Figure 7-4. The Arrhenius plots of (a) $\text{C}_6\text{H}_{13}\text{I}$ -733 ppbv adsorption, and (b) $\text{C}_{12}\text{H}_{25}\text{I}$ -113 ppbv adsorption.

For the C₆H₁₃I-101 ppbv and C₁₂H₂₅I-606 ppbv adsorptions, applying the Arrhenius relationship may not be suitable since the minimum k_s 's appear to exist at 150 °C. The detailed relationship between reaction rates and the activation energies were discussed in **Section 6.7**. The existence of the minimum k_s in the temperature range, reversed dependency and the negative activation energy were predicted based on theoretical analyses and literature surveys.

To further analyze the temperature dependencies, performing the adsorption experiments with various combinations of temperatures and the organic iodides species may not be practicable because of the workload. At least tens of combinations need to be examined and numerous repeats are required, whereas each experiment may take weeks. Therefore, software-based computational simulations are suggested in future studies for determining the detailed temperature dependencies and the related energies of the organic iodides adsorptions.

7.6 Carbon Chain Length Dependence

The adsorption kinetics acquired at 150 °C and approximately 100 ppbv are used for determining the effect of the carbon chain length. The conditions include CH₃I-104 ppbv, C₃H₇I-96 ppbv, C₆H₁₃I-101 ppbv, C₈H₁₇I-60 ppbv, and C₁₂H₂₅I-113 ppbv. The adsorption kinetics are plotted in Figure 7-5.

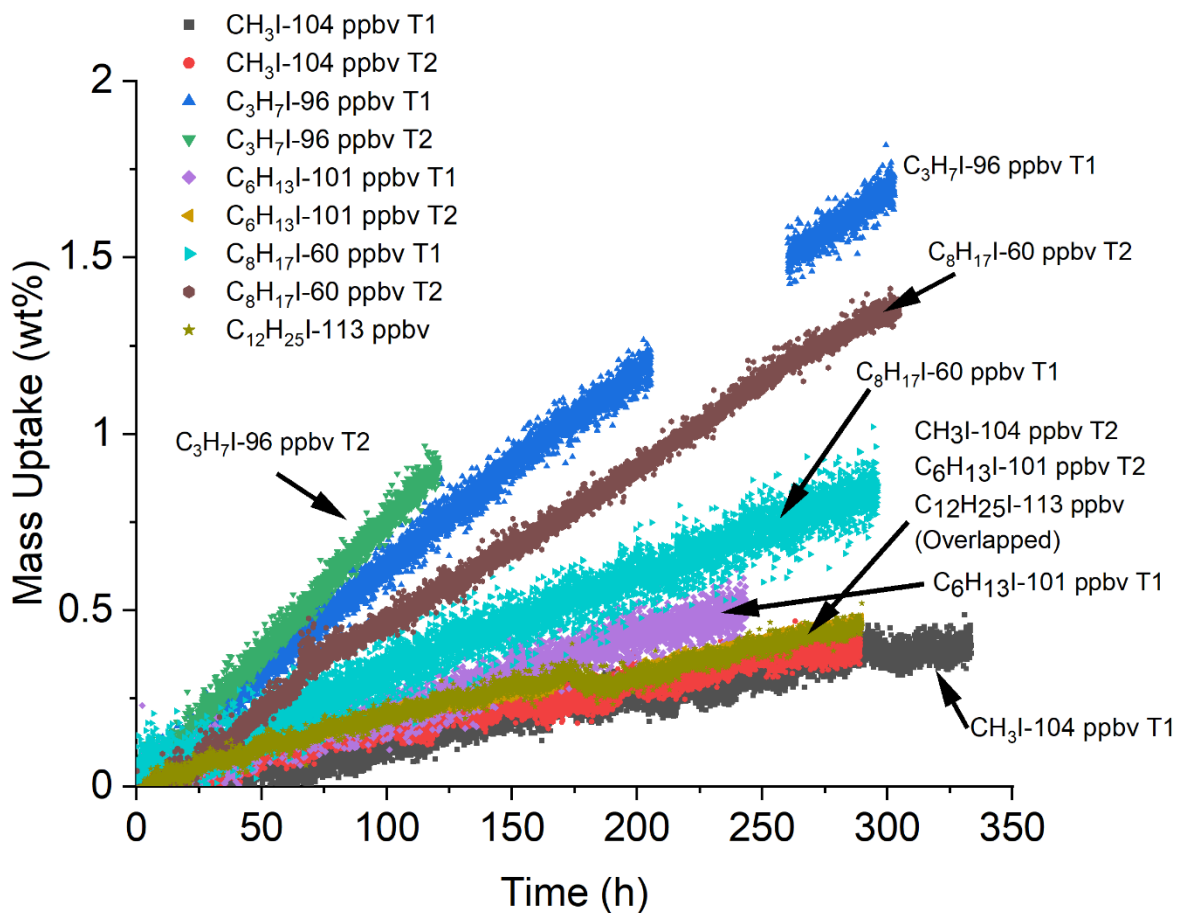


Figure 7-5. The adsorption kinetics of CH_3I -104 ppbv, $\text{C}_3\text{H}_7\text{I}$ -96 ppbv, $\text{C}_6\text{H}_{13}\text{I}$ -101 ppbv, $\text{C}_8\text{H}_{17}\text{I}$ -60 ppbv, and $\text{C}_{12}\text{H}_{25}\text{I}$ -113 ppbv at 150 °C. (T1 and T2 represent different experimental trials)

Visualized from the figure, the uptake rates of CH_3I , $\text{C}_6\text{H}_{13}\text{I}$ and $\text{C}_{12}\text{H}_{25}\text{I}$ are relatively similar, whereas those of $\text{C}_3\text{H}_7\text{I}$ and $\text{C}_8\text{H}_{17}\text{I}$ are higher. Similar behaviors are also revealed in the model fitting results, the $\text{C}_3\text{H}_7\text{I}$ and $\text{C}_8\text{H}_{17}\text{I}$ adsorptions obtain much higher reaction rate constants than others do. The model fitting procedure is the same as above (**Section 7.3**). To maintain the consistency of model fitting, the pore diffusion term in the SCM was neglected.

Concentration (ppbv)	Avg Ads Rate (wt%/h)	k_f^* (cm/s)	k_s (cm/s)	AARD (%)
CH₃I				
104 T1	1.39×10^{-3}	2.71	0.239	14.63%
104 T2	1.35×10^{-3}	2.71	0.184	10.66%
Average	1.37×10^{-3}		0.212	
C₃H₇I				
96 T1	5.65×10^{-3}	2.17	1.651	4.58%
96 T2	7.59×10^{-3}	2.17	2.474	12.37%
Average	6.62×10^{-3}		2.063	
C₆H₁₃I				
101 T1	1.51×10^{-3}	1.76	0.338	14.08%
101 T2	2.02×10^{-3}	1.76	0.437	17.54%
Average	1.77×10^{-3}		0.388	
C₈H₁₇I				
60 T1	2.80×10^{-3}	1.59	1.697	17.48%
60 T2	5.11×10^{-3}	1.59	3.563	14.04%
Average	3.96×10^{-3}		2.630	
C₁₂H₂₅I				
113	1.46×10^{-3}	1.37	0.301	4.44%

*Calculated theoretically

Table 7-3. The parameters and model fitting results of CH₃I-104 ppbv, C₃H₇I-96 ppbv, C₆H₁₃I-101 ppbv, C₈H₁₇I-60 ppbv, and C₁₂H₂₅I-113 ppbv at 150 °C. (T1 and T2 represent different experimental trials)

The uptake rates of the C₃H₇I and C₈H₁₇I adsorptions are higher than expected and repeats were

performed to verify the results. Furthermore, since the Ag^0 -Aerogel is a highly heterogeneous material, the sizes of pellets used in all trails were also examined and the consistency was confirmed. With similar concentrations, the average uptake rates and reaction rate constants of the $\text{C}_3\text{H}_7\text{I}$ and $\text{C}_8\text{H}_{17}\text{I}$ are unexpectedly high and the behaviors observed appear to be trustful. Based on the results, the dependency of the adsorption rate on the length of carbon chain is not conclusive. A qualified observation is that, at low concentrations (tens of, or up to approximately 100 ppbv), the adsorption rates of CH_3I , $\text{C}_6\text{H}_{13}\text{I}$ and $\text{C}_{12}\text{H}_{25}\text{I}$ are relatively similar, and those of $\text{C}_3\text{H}_7\text{I}$ and $\text{C}_8\text{H}_{17}\text{I}$ are much higher. Therefore, when designing the adsorption columns, the scientists should focus on satisfying the removal efficiencies of the CH_3I , $\text{C}_6\text{H}_{13}\text{I}$ and $\text{C}_{12}\text{H}_{25}\text{I}$, since the same column should clearly be adequate for the $\text{C}_3\text{H}_7\text{I}$ and $\text{C}_8\text{H}_{17}\text{I}$ removals.

7.7 Conclusions and Recommendations

In this chapter, the adsorptions of other organic iodides including $\text{C}_3\text{H}_7\text{I}$, $\text{C}_6\text{H}_{13}\text{I}$, $\text{C}_8\text{H}_{17}\text{I}$ and $\text{C}_{12}\text{H}_{25}\text{I}$ were performed. The results indicate that the adsorptions of $\text{C}_6\text{H}_{13}\text{I}$ and $\text{C}_{12}\text{H}_{25}\text{I}$ are likely to be zero-order, in which the adsorption rates are independent of the concentrations at the ranges studied. A hypothesis based on the Langmuir adsorption model was proposed, suggesting that the ‘effective concentration (concentration available for reaction)’ may be limited by the reaction sites. Therefore, for the industrial applications, $\text{C}_6\text{H}_{13}\text{I}$ and $\text{C}_{12}\text{H}_{25}\text{I}$ (at least but may not be limited to) of high concentrations (hundreds of ppbv) should be avoided. The reason and a simulation will be presented in **Section 8.5**.

Moreover, the concentration dependencies of the organic iodide adsorptions are not consistent.

Three patterns are observed, the reaction rate increases with temperature, the reaction rate decreases with temperature and a minimum reaction rate exists in the temperature range, which agrees with the prediction made in **Chapter 6**. As for the carbon chain length dependence, the tendency remains unresolved. The CH_3I , $\text{C}_6\text{H}_{13}\text{I}$ and $\text{C}_{12}\text{H}_{25}\text{I}$ adsorptions obtain similar reaction rate constants and the reaction rate constants of the $\text{C}_3\text{H}_7\text{I}$ and $\text{C}_8\text{H}_{17}\text{I}$ are much higher.

To further understand the organic iodides adsorption on Ag^0 -Aerogel, experimental methods may not be worthy due to the overwhelming workload comparing with the conclusions that may be revealed. Therefore, software-based computational simulations are suggested in solving the related questions.

Chapter 8. Column Adsorption Modeling

8.1 Shrinking Core Model Incorporated Column Adsorption Modeling

Since the reaction rates were determined, the column adsorption behavior of organic iodides can be estimated using the model suggested by Yang¹⁷⁶ and Ruthven.¹³⁶ Neglecting the axial dispersion of organic iodide and the temperature gradient due to reaction, the model can be written as,

$$\frac{\partial(uC)}{\partial z} + \frac{\partial C}{\partial t} + \rho_p \left(\frac{1 - \varepsilon_b}{\varepsilon_b} \right) \frac{\partial q}{\partial t} = 0 \quad 8-1$$

where u is the gas velocity (cm/s), z is the distance from the inlet (cm), ε_b is the bulk porosity of the bed and $\partial q/\partial t$ is the adsorption rate. Since the organic iodides in the fluid are at ppbv level, the drops of pressure and gas velocity through the adsorption column are neglected. For a shrinking core process adsorption, the $\partial q/\partial t$ can be approximated by,¹²⁷

$$\frac{q}{q_e} = 1 - \left(\frac{r_c}{R_a} \right)^3 \quad 8-2$$

and,

$$\frac{\partial q}{\partial t} = - \frac{3q_e r_c^2}{R_a^3} \frac{\partial r_c}{\partial t} \quad 8-3$$

where r_c is the radius (cm) of the unreacted core. Discussed in **Chapter 5**, the gas film diffusion in the shrinking core model is neglectable for the adsorption, therefore, the $\partial r_c/\partial t$ can be written as,¹²⁷

$$\frac{\partial r_c}{\partial t} = \frac{bC_b / q_e \rho_p}{\frac{(R_a - r_c)r_c}{R_a D_p} + \frac{1}{k_s}} \quad 8-4$$

8.2 40 ppbv CH₃I Column Adsorption, Literature Comparison

The study of CH₃I adsorption on Ag⁰-Aerogel performed by Bruffey et al.⁸⁷ can be used as a reference. In the study, 40 ppbv CH₃I flowed through three sections containing Ag⁰-Aerogel with lengths of 0.2, 11 and 0.5 cm, respectively. The temperature was 150 °C; the diameter of the column system was 3.45 cm and the gas velocity was 10 m/min. In 16 weeks (approximately 120 days), Bruffey et al.⁸⁷ measured an average adsorption rate of 6.9×10⁻⁴ wt%/h in section 1. By performing the neutron activation analysis (NAA), no iodine was observed in section 3. Since the detecting limit of NAA is 0.0045 mg I/g, Bruffey et al.⁸⁷ calculated a maximum CH₃I concentration exiting section 2 of 0.105 ppbv and the minimum decontamination factor (DF) of 382.

In the modeling, the full column length is set to be 11.2 cm (the length of column 1 plus column 2 in the study performed by Bruffey et al.⁸⁷). The concentration-compensated *pseudo* k_s of 0.19 cm/s at 40 ppbv was estimated by Eq. 5-17. Admittedly, the CH₃I concentrations through the adsorption column change with the distance from the inlet, but incorporating the real-time calculations of *pseudo* k_s increases the calculation workload significantly. The D_p of 6.7×10⁻⁴ cm²/s was calculated in **Chapter 5**, the bulk porosity ε_b was assumed to be 0.37,^{177,178} and the dry air aging effect was neglected. Eq. 8-1 can be solved by numerical integration and the results are shown in Figure 8-1.

The CH₃I concentration, the mass uptake of Ag⁰-Aerogel and the core shrinkage r_c/R_a through the column by time are plotted in Figure 8-1a, b and c respectively. In 120 days, the CH₃I outlet concentration maintains below 0.06 ppbv and the DF is greater than 650 (Figure 8-1d), which is constant with the maximum CH₃I outlet concentration of 0.105 ppbv proposed by Bruffey et al.⁸⁷ Since the concentration gradient in the first 0.2 cm (section 1) is roughly linear, the mass uptake in section 1 may be estimated by the mass uptake at $z = 0.1$ (Figure 8-1e). The mass uptake reaches 1.2 wt% in 120 days with an average mass uptake rate of 4.4×10^{-4} wt%/h, which are comparable with the experimental values of 2.0 wt% and 6.9×10^{-4} wt%/h.⁸⁷ Moreover, in Figure 8-1f, the mass uptake by distance at day 120, the mass uptake at 2 and 4 cm is approximately 0.45 and 0.15 wt%, which are close to the observation by Bruffey et al.⁸⁷ and the penetration depth of 5-8 cm is also comparable.

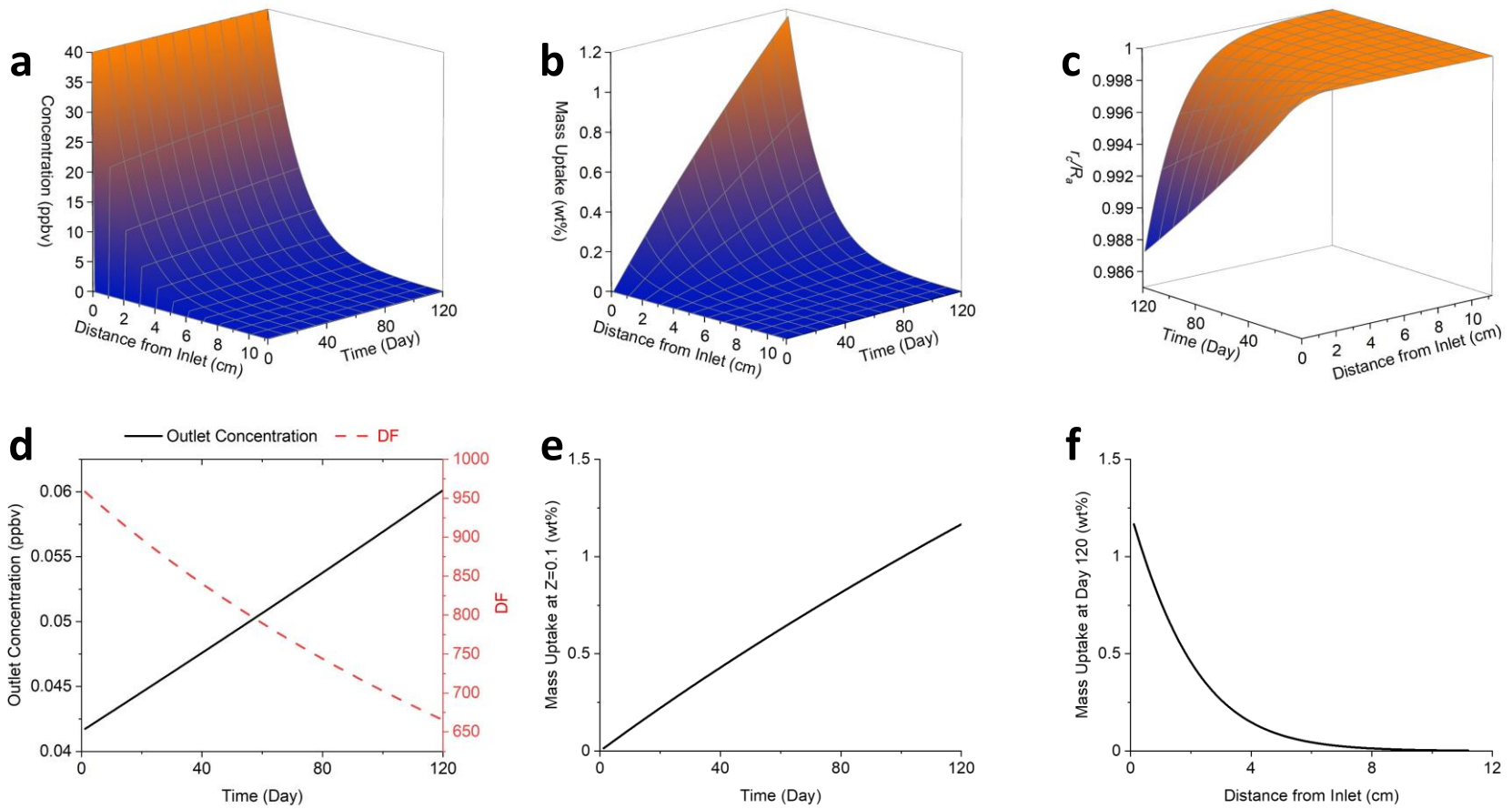


Figure 8-1. Fitting results of the 40 ppbv CH₃I column adsorption on Ag⁰-Aerogel in 120 days. (a) CH₃I concentration in the column by time, (b) mass uptake of Ag⁰-Aerogel in the column by time, (c), the core shrinkage r_c/R_a by time, (d) outlet concentration and the decontamination factor (DF), (e) mass uptake at the middle of section 1 ($z = 0.1$ cm), (f) mass uptake at Day 120 by distance.

8.3 Modeling Results, Column Breakthrough

The model can also be used to describe the breakthrough of the adsorption column. In this case, the dry air aging effect must be considered. The adsorption capacity q_e is set to 30.8 wt%, which is the capacity of Ag⁰-Aerogel after being aged for long enough (greater than approximately 170 days, discussed in **Section 5.3**). The other parameters are the same as **Section 8.2**.

The results are plotted in Figure 8-2. In 10000 days, the outlet concentration increases to 16 ppbv, whereas the DF decreases from approximately 1000 to 2 (Figure 8-2d), indicating the breakthrough of the column is in progress. By 10000 days, the mass uptake of the pellets at the column inlet reaches 20 wt% and that at the outlet is approximately 8 wt%.

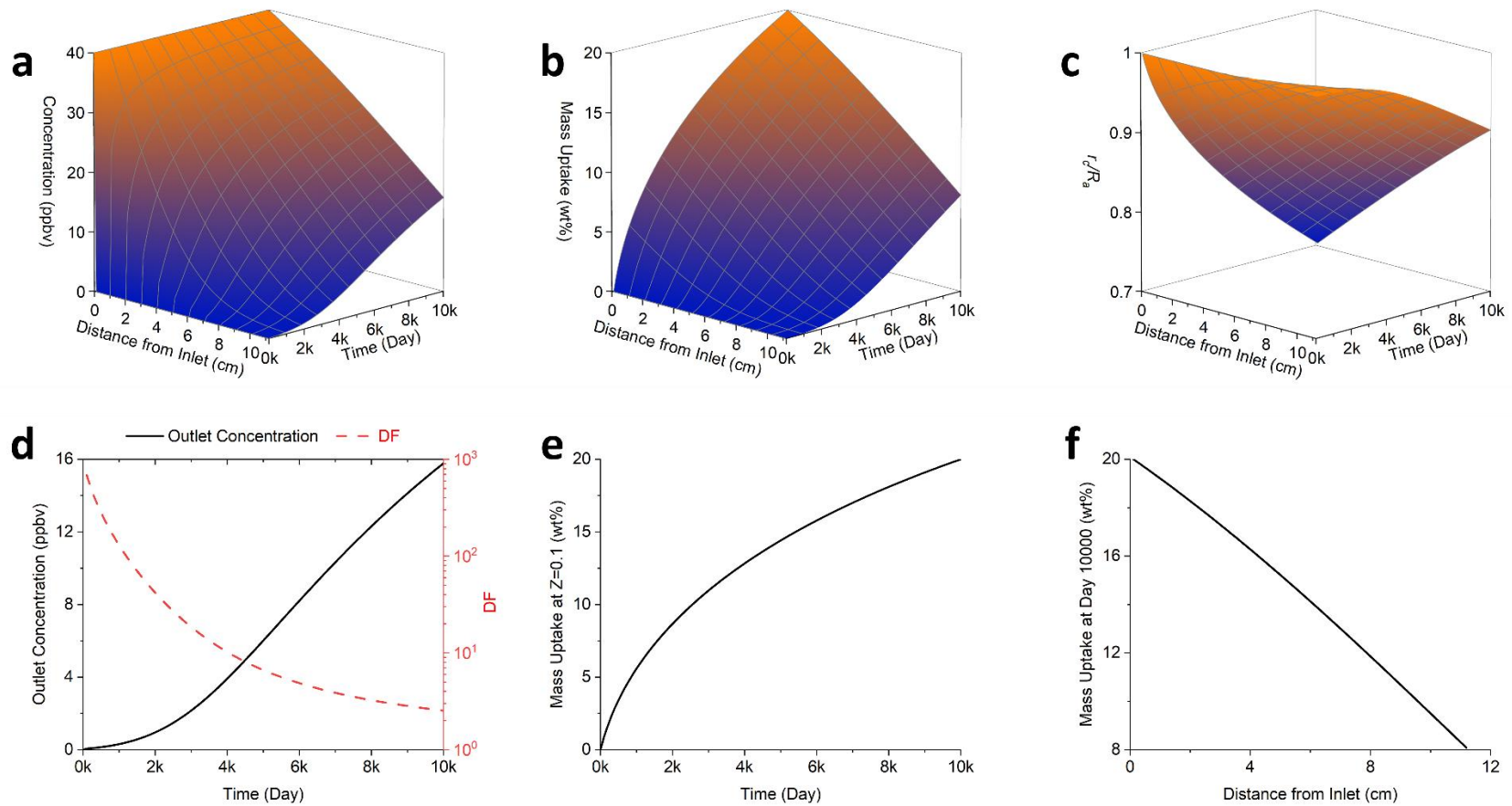


Figure 8-2. Estimation of the breakthrough for the 40 ppbv CH₃I column adsorption on Ag⁰-Aerogel. (a) CH₃I concentration in the column by time, (b) mass uptake of Ag⁰-Aerogel in the column by time, (c) the core shrinkage r/R_a by time, (d) outlet concentration and the decontamination factor (DF), (e) mass uptake at the middle of section 1 ($z = 0.1$ cm), (f) mass uptake at Day 10000 by distance.

8.4 Column Length and Breakthrough

To estimate the length required for the adsorption column, the modeling of 40 ppbv CH₃I adsorptions in columns with different lengths was performed. The emission iodine radioactivity is regulated by NRC and EPA, and the corresponding concentration has been calculated in **Section 2.1** to be 0.0406 ppbv. In the adsorption column modeling, the lengths of columns were set to 5 to 20 cm and all other parameters are identical. The results in Figure 8-3 indicate that an adsorption column of at least 12 cm is required and the outlet concentration is approximately 0.03 ppbv before the breakthrough. For the 12 cm adsorption column, the breakthrough starts in around 100 days, and the emission regulation is no longer satisfied after approximately 150 days.

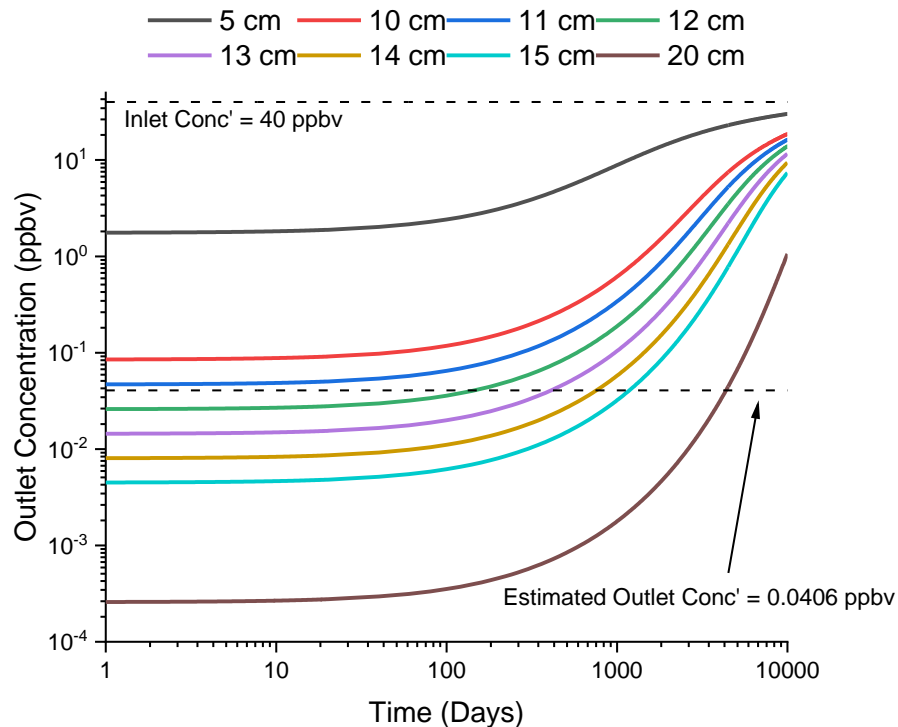


Figure 8-3. Estimating the effectiveness of 40 ppbv CH₃I removal using columns with different lengths (From the top to the bottom, the column lengths increase accordingly).

Increasing the column length extends the column lifetime and reduces the outlet CH₃I concentration significantly. For example, with a 20 cm column, the outlet CH₃I concentration may be reduced to sub-pptv (part per trillion by volume) level and the column lifetime may be greater than 10 years. Therefore, conservatively speaking, to satisfy the regulation and extend the lifetime, a column of at least 15-20 cm is required for the 40 ppbv CH₃I adsorption.

8.5 Simulations of C₁₂H₂₅I Column Adsorption

In **Section 7.4 and 7.7**, the C₆H₁₃I and C₁₂H₂₅I adsorptions was observed to be a zero-order process, the adsorption rates are independent of the adsorbate concentrations. Therefore, it is suggested that C₆H₁₃I and C₁₂H₂₅I of high concentrations should be avoided in the column adsorptions and the reasons are discussed in this section. The column modeling of 113 and 606 ppbv C₁₂H₂₅I adsorptions are compared. The ϵ_p , temperature, and gas velocity are the same as above. D_p was estimated to be 3.14×10^{-4} cm²/s, and k_s was 0.340 and 0.040 cm/s for 113 ppbv and 606 ppbv respectively (parameters acquired from **Section 7.3.2**)

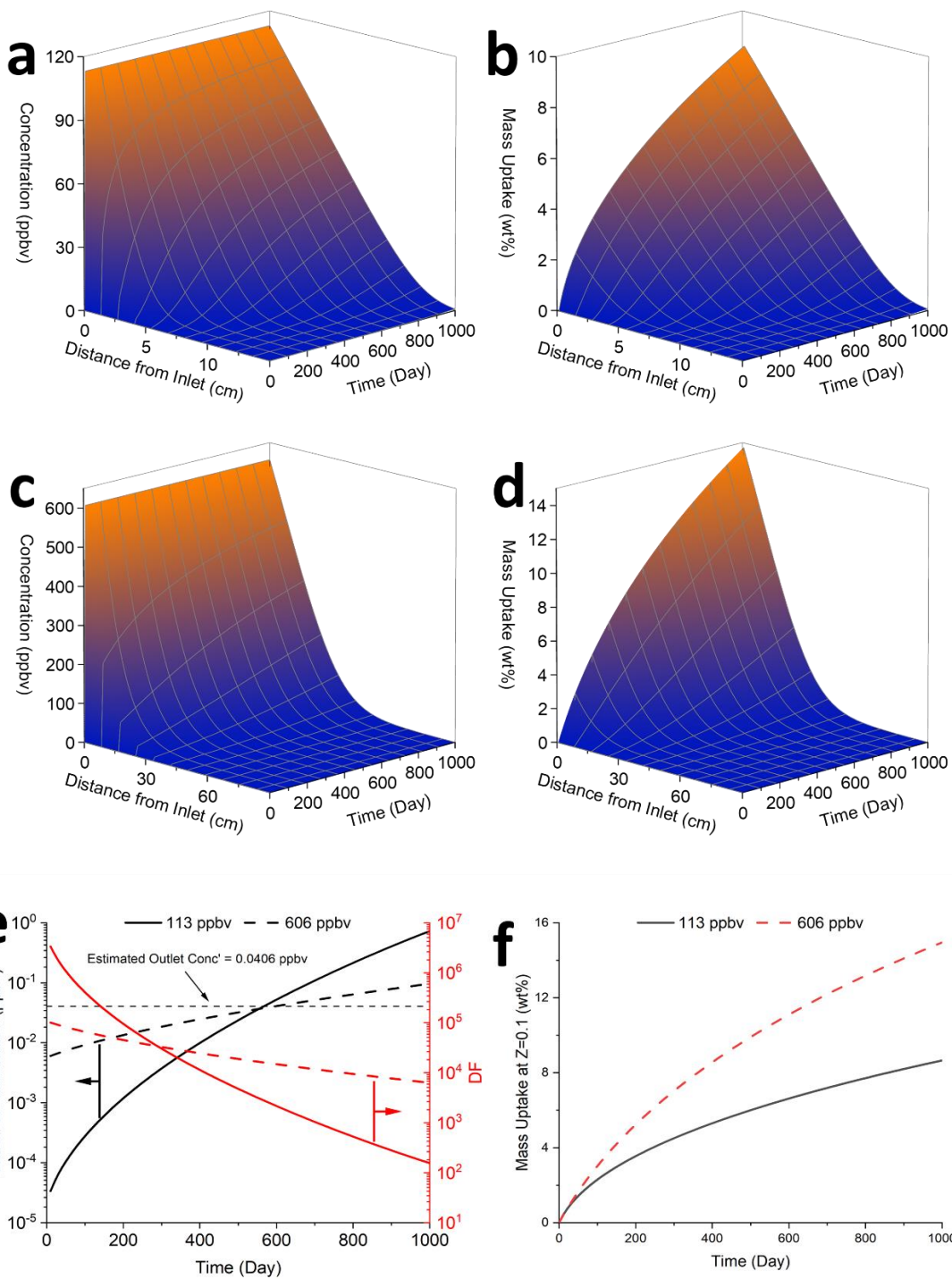


Figure 8-4. (a) $C_{12}H_{25}I$ concentration in the column by time (113 ppbv), (b) mass uptake of Ag^0 -Aerogel in the column (113 ppbv), (c) $C_{12}H_{25}I$ concentration in the column (606 ppbv), (d) mass uptake of Ag^0 -Aerogel in the column by time (606 ppbv), (e) $C_{12}H_{25}I$ outlet concentration and the decontamination factor (DF) of two adsorption columns, (f) the mass uptake at $Z=0.1$ cm of two adsorption columns. (Column lengths are 15 and 90 cm for 113 and 606 ppbv respectively)

The column modeling results are shown in Figure 8-4. A 15 cm column is adequate to remove the $C_{12}H_{25}I$ of 113 ppbv, and the outlet concentration remains below 10^{-2} ppbv in approximately 150 days. The lifetime of the column is more than 500 days. To achieve a similar lifetime, a 6-time longer column is required for removing the $C_{12}H_{25}I$ of 606 ppbv concentration since the $C_{12}H_{25}I$ adsorption is an approximately zero-order process. This zero-order can be further visualized in the mass transfer zone plot (Figure 8-5a). Since the adsorption is a zero-order process, the mass transfer zone almost increases proportionally to the concentration. The mass transfer zone for 113 ppbv adsorption is 6-7 cm in length and that of 606 ppbv is 40-50 cm. Similar behaviors are also revealed in Figure 8-5b, at the end of the adsorptions, 606 ppbv $C_{12}H_{25}I$ penetrates much deeper into the column than 113 ppbv $C_{12}H_{25}I$ does.

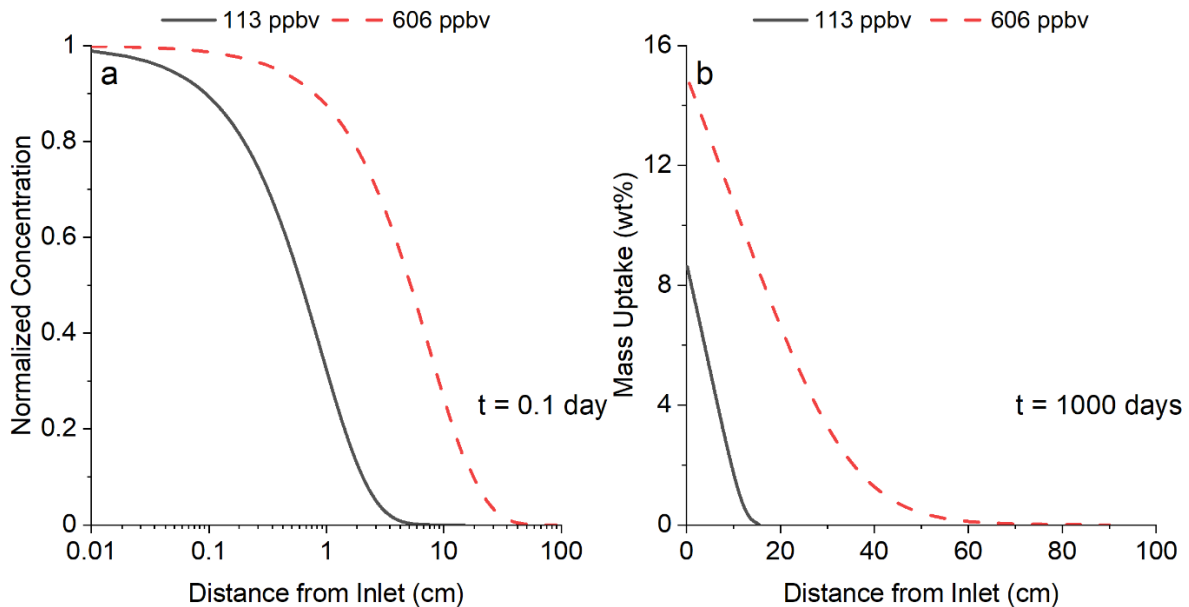


Figure 8-5. (a) The mass transfer zone of two columns at $t=0.1$ day, (b) the penetration of $C_{12}H_{25}I$ into two columns at the end of adsorptions.

The comparison of the 113 and 606 ppbv $C_{12}H_{25}I$ column adsorptions indicates that the mass transfer zone increases significantly as the concentration increases because of the zero-order reaction. Therefore, in industrial applications, the $C_6H_{13}I$ and $C_{12}H_{25}I$ of high concentrations should be avoided.

8.6 Recommendations and Conclusions

In this chapter, the shrinking core model was incorporated into the column adsorption modeling. By performing the numerical integration, the column adsorption behaviors were estimated, and the estimation results were comparable with the experiments performed by Bruffey et al.⁸⁷ For the tens of ppbv level adsorptions, to achieve a sufficient lifetime, the column of at least 15-20 cm is suggested. In the industrial application, the ppbv level of organic iodides are mixed with the ppmv level I_2 before the adsorption.^{14,36} Obviously, the I_2 breakthrough will happen much sooner than the organic iodide breakthrough, which implies that as long as the outlet organic iodides concentrations are lower than that of I_2 during the adsorption, the impact of organic iodides on the column adsorption may be neglected. Multiple column adsorptions of ppmv level I_2 using Ag^0 -Aerogel were performed, and the results indicated that the breakthroughs are generally within days or up to weeks.^{97,101} Therefore, the impacts of ppbv level organic iodides to the column adsorptions appear to be minor. However, since the adsorptions of $C_6H_{13}I$ and $C_{12}H_{25}I$ were observed to be zero-order processes, the $C_6H_{13}I$ and $C_{12}H_{25}I$ of high concentrations (hundreds of ppbv) should be avoided or pretreated in the column adsorption systems.

Chapter 9. Recommendations for Future Studies and Industrial Applications

9.1 Sulfur in Ag⁰-Aerogel and the Relationship to Aging and Reaction Mechanism

Observed in previous studies, the Ag⁰-Aerogel consists of Ag⁰ nanoparticles on SiO₂ support with -SH, R-S-Ag groups binding to Ag⁰.^{65,179} A rough schematic diagram is shown in Figure 9-1, the -SH and R-S-Ag groups form a protection layer around the Ag⁰, which the Ag⁰ nanoparticles on Ag⁰Z are exposed to the ambience.¹⁵

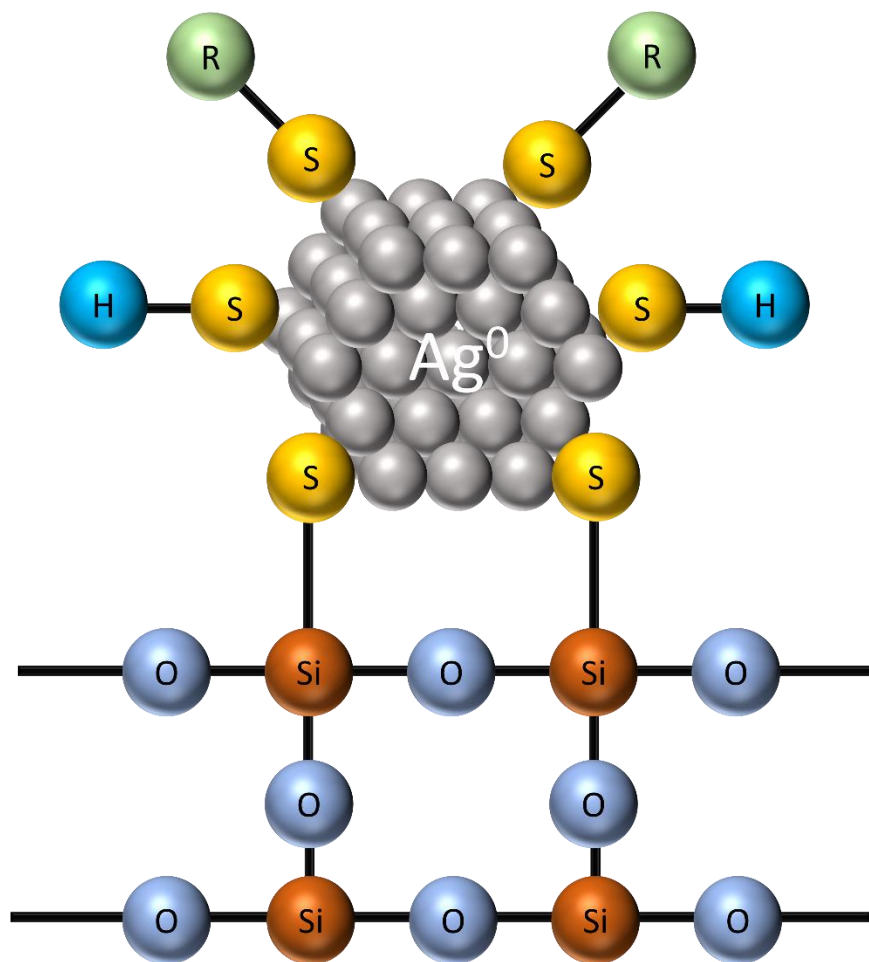


Figure 9-1. The schematic diagram of the chemical structure of Ag⁰-Aerogel.

The sulfuric compounds in the Ag⁰-Aerogel change the aging resistance and the mechanism.¹⁰⁵ Moreover, during the organic iodides adsorption on Ag⁰-Aerogel, the sulfuric compounds may interact with organic iodides, which similar reactions were proposed by Selker¹⁸⁰ and Markuszewski et al.¹⁸¹ To further understand the aging and adsorption behavior of Ag⁰-Aerogel, detailed studies on the sulfuric groups are suggested.

9.2 Long-Chain Iodoalkanes and Products

Due to the additional alkyl group, the reactions of CH₃I between Ag⁰-Aerogel are more complicated than that of I₂, and multiple organic products include alkanes, alcohols, ethers and nitro compounds were measured in the outlet gas.^{89,90} For the organic iodides with longer chains (e.g., C₆H₁₃I, C₁₂H₂₅I), the organic products would be even more sophisticated.

In a typical off-gas treatment system (Figure 1-1), a certain amount of ¹⁴C exists and a CO₂ capture vessel is attached right after the iodine capture vessel to remove the radioactive carbon.^{14,36} However, the methods used are typically designed for CO₂, which include caustic scrubbing, physisorption and chemisorption.¹⁴ With the presence of ¹⁴C, the organic products from the iodoalkanes-Ag⁰-Aerogel adsorptions could also be radioactive and the CO₂ capture methods may be inadequate for removing the radioactive organic compounds. Therefore, understanding the reactions between the alkyl groups and Ag⁰-Aerogel is beneficial for the design of the waste reprocessing system.

9.3 Suggestions for Next-Generation Materials and Adsorption systems

In the presented work, the organic iodides adsorptions on multiple silver-containing materials were examined and the Ag⁰-Aerogel appears to be the most efficient material among Ag⁰-Aerogel, Ag⁰Z and AgA. Towards the next generation materials, the following suggestions are made based on the results determined.

1. Higher pore diffusivity.

As the rate-limiting step of the overall adsorption process, increasing the pore diffusivity results in more rapid adsorptions and may increase the efficiency of the adsorption column significantly.

2. Uniform shape and higher mechanical stability.

Ag⁰-Aerogel is a highly heterogeneous material: the shape, size and silver coverage are uneven. Additionally, during the adsorption, the pellets crash into smaller particles. During the column adsorption, the ashes may be carried out of the column by the gas flow, resulting in the contamination of the following vessels. To resolve the issue, materials with higher mechanical stability are suggested.

3. Novel aging-protection techniques.

The thiol-functionalizing technique is applied in the Ag⁰-Aerogel manufacturing and the NO

aging resistance increases significantly. As for NO₂ aging, Ag⁰-Aerogel maintains the highest iodine adsorption capacity among the materials tested but the capacity loss (~80%) is still considerable. For the next generation materials, new aging-protection techniques are suggested. For example, some 'NO_x-active' functional groups could be the alternatives. Instead of passive defense, the functional groups react and decontaminate the NO_x actively, and the Ag⁰ nanoparticles may be protected from the aging agents.

For the next-generation adsorption system, two suggestions are also proposed.

1. NO_x pretreatment.

The NO_x reduces the iodine adsorption capacity of the material by oxidizing the Ag⁰. To prevent the aging effects radically, a NO_x pretreatment process is suggested in the next-generation adsorption system.

2. Radioactive organic compounds removal.

After the organic iodides adsorptions, the ¹⁴C may not only be presented as CO₂ but also organic compounds. To satisfy the ¹⁴C emission regulations, it may also be necessary to remove the radioactive organic compounds. Some oxidation methods such as metal catalytic oxidation or combustion vessel would be possible choices.

References

1. Hahn O, Strassmann F. Über den Nachweis und das Verhalten der bei der Bestrahlung des Urans mittels Neutronen entstehenden Erdalkalimetalle. *Naturwissenschaften*. 1939;27(1):11-15.
2. Gosling FG. *The Manhattan Project: Making the Atomic Bomb (DOE/MA-0001)*. Washington: History Division, Department of Energy. 1999.
3. Groves GLR. *Now it can be told: The story of the Manhattan Project*. Da Capo Press. 2009.
4. Office of Nuclear Energy. 9 Notable Facts About the World's First Nuclear Power Plant - EBR-I. 2019. Accessed Jan. 11, 2021.
5. Office of Nuclear Energy. Nuclear Power is the Most Reliable Energy Source and It's Not Even Close. 2021. Accessed May. 17, 2021.
6. U.S. Nuclear Regulatory Commission. Operating Nuclear Power Reactors (by Location or Name). 2021. Accessed May. 20, 2021.
7. U.S. Energy Information Administration. Monthly Energy Review. 2021. Accessed May. 20, 2021.
8. Lenzen M. Life cycle energy and greenhouse gas emissions of nuclear energy: A review. *Energy Conversion and Management*. 2008;49(8):2178-2199.
9. Wei M, Patadia S, Kammen DM. Putting renewables and energy efficiency to work: How many jobs can the clean energy industry generate in the US? *Energy Policy*.

- 2010;38(2):919-931.
10. Menyah K, Wolde-Rufael Y. CO₂ emissions, nuclear energy, renewable energy and economic growth in the US. *Energy Policy*. 2010;38(6):2911-2915.
 11. Haefner DR, Tranter TJ. Methods of Gas Phase Capture of Iodine from Fuel Reprocessing Off-Gas: A Literature Survey. Technical Report No. INL/EXT-07-12299. Idaho National Laboratory, Idaho Falls, ID. 2007.
 12. Purkayastha BC, Martin GR. The yields of ¹²⁹I in natural and in neutron-induced fission of uranium. *Canadian Journal of Chemistry*. 1956;34(3):293-300.
 13. Lamarsh JR, Baratta AJ. *Introduction to nuclear engineering*. Vol 3: Prentice hall Upper Saddle River, NJ. 2001.
 14. Jubin RT, DelCul GD, Patton BD, Owens RS, Ramey DW, Spencer BB. Advanced fuel cycle initiative coupled end-to-end research, development, and demonstration project: integrated off-gas treatment system design and initial performance. 2009
 15. Nan Y. *Adsorption of Iodine and Water on Silver-Exchanged Mordenite* [Dissertation], Syracuse University; 2017.
 16. NRC. NRC regulations title 10—code of federal regulations, Part 20—standards for protection against radiation. Technical Report., US Nuclear Regulatory Commission, Washington, DC. 2019.
 17. EPA. Environmental radiation protection standards for nuclear power operations (40 CFR Part 190). In. Washington, DC: US Environmental Protection Agency; 2010.

18. Snyder G, Aldahan A, Possnert G. Global distribution and long-term fate of anthropogenic ^{129}I in marine and surface water reservoirs. *Geochemistry, Geophysics, Geosystems*. 2010;11(4).
19. Suzuki T, Kitamura T, Kabuto S, Togawa O, Amano H. High sensitivity measurement of iodine-129/iodine-127 ratio by accelerator mass spectrometry. *Journal of Nuclear Science and Technology*. 2006;43(11):1431-1435.
20. Moran JE, Oktay S, Santschi PH, Schink DR. Atmospheric dispersal of ^{129}I from nuclear fuel reprocessing facilities. *Environmental science & technology*. 1999;33(15):2536-2542.
21. Moran JE, Oktay SD, Santschi PH. Sources of iodine and iodine 129 in rivers. *Water Resources Research*. 2002;38(8):24-21-24-10.
22. Suzuki T, Otosaka S, Kuwabara J, Kawamura H, Kobayashi T. Iodine-129 concentration in seawater near Fukushima before and after the accident at the Fukushima Daiichi Nuclear Power Plant. *Biogeosciences*. 2013;10(6):3839-3847.
23. Daraoui A, Michel R, Gorny M, et al. Iodine-129, Iodine-127 and Caesium-137 in the environment: soils from Germany and Chile. *Journal of Environmental Radioactivity*. 2012;112:8-22.
24. A. L. Nichols DLA, M. Verpelli *Handbook of Nuclear Data for Safeguards: Database Extensions*. Vienna, Austria: International Atomic Energy Agency. 2008.
25. Burkinshaw L. The Half-Life of Iodine-131. *Physics in Medicine and Biology*.

- 1958;2(3):255-257.
26. Alfimov V, Possnert G, Aldahan A. Anthropogenic iodine-129 in the Arctic Ocean and Nordic Seas: Numerical modeling and prognoses. *Marine Pollution Bulletin*. 2006;52(4):380-385.
 27. Álvarez F, Reich M, Snyder G, et al. Iodine budget in surface waters from Atacama: Natural and anthropogenic iodine sources revealed by halogen geochemistry and iodine-129 isotopes. *Applied Geochemistry*. 2016;68:53-63.
 28. Herod MN, Li T, Pellerin A, Kieser WE, Clark ID. The seasonal fluctuations and accumulation of iodine-129 in relation to the hydrogeochemistry of the Wolf Creek Research Basin, a discontinuous permafrost watershed. *Science of The Total Environment*. 2016;569-570:1212-1223.
 29. Muramatsu Y, Ohmomo Y. Iodine-129 and iodine-127 in environmental samples collected from Tokaimura/Ibaraki, Japan. *Science of The Total Environment*. 1986;48(1):33-43.
 30. Alfimov V, Aldahan A, Possnert G, Winsor P. Anthropogenic iodine-129 in seawater along a transect from the Norwegian coastal current to the North Pole. *Marine Pollution Bulletin*. 2004;49(11):1097-1104.
 31. Smith JN, McLaughlin FA, Smethie Jr WM, Moran SB, Lepore K. Iodine-129, ¹³⁷Cs, and CFC-11 tracer transit time distributions in the Arctic Ocean. *Journal of Geophysical Research: Oceans*. 2011;116(C4).
 32. Soldat JK, Brauer FP, Cline JF, et al. Radioecology of iodine-129: an interim report.

- Technical Report United States. 1973.
33. Fisher DA, Oddie TH. Thyroid Iodine Content and Turnover in Euthyroid Subjects: Validity of Estimation of Thyroid Iodine Accumulation from Short-Term Clearance Studies. *The Journal of Clinical Endocrinology & Metabolism*. 1969;29(5):721-727.
 34. Kitazono M, Robey R, Zhan Z, et al. Low Concentrations of the Histone Deacetylase Inhibitor, Depsipeptide (FR901228), Increase Expression of the Na⁺/I⁻ Symporter and Iodine Accumulation in Poorly Differentiated Thyroid Carcinoma Cells. *The Journal of Clinical Endocrinology & Metabolism*. 2001;86(7):3430-3435.
 35. Wyngaarden JB, Wright BM, Ways P. The Effect of Certain Anions upon the Accumulation and Retention of Iodide by the Thyroid Gland. *Endocrinology*. 1952;50(5):537-549.
 36. Jubin RT, Strachan D. Assessments and Options for Removal and Immobilization of Volatile Radionuclides from the Processing of Used Nuclear Fuel. Technical Report No. ORNL/SPR-2015/115. Oak Ridge National Laboratory (ORNL), Oak Ridge, TN. 2015.
 37. Bruffey SH, Jubin RT, Jordan JA. Capture of Elemental and Organic Iodine from Dilute Gas Streams by Silver-exchanged Mordenite. *Procedia Chemistry*. 2016;21:293-299.
 38. Bruffey SH, Spencer BB, Strachan DM, Jubin RT, Soelberg NR, Riley BJ. A literature survey to identify potentially problematic volatile iodine-bearing species present in off-gas streams. Technical Report No. ORNL-SPR-2015/290. Oak Ridge National Laboratory (ORNL), Oak Ridge, TN. 2015.

39. Jubin RT, Bruffey SH, Spencer BB. Performance of Silver-exchanged Mordenite for Iodine Capture under Vessel Off-gas Conditions. Technical Report No. DE-AC05-00OR22725. Oak Ridge National Lab (ORNL), Oak Ridge, TN 2015.
40. Henrich E, Schmieder H, Roesch W, Weirich F. Improved iodine and tritium control in reprocessing plants. Paper presented at: 16th DOE Nuclear Air Cleaning Conference. 1981; The Harvard Air Cleaning Laboratory, Cambridge, MA
41. Sakurai T, Komaki Y, Takahashi A, Izumo M. Applications of zeolites to remove iodine from dissolver off-gas, (III) Adsorption of methyl iodide (CH_3I^*) on zeolite 13X. *Journal of Nuclear Science and Technology*. 1983;20(12):1046-1047.
42. Nakamura K, Saeki M, Tachikawa E. Formation of Organic Iodides upon Heating Nitric Acid Solutions Containing Carrier-Free Iodine-131. *Journal of Nuclear Science and Technology*. 1973;10(6):367-373.
43. Thomson JJ, Aston FW, Soddy F, Merton TR, Lindemann FA. Discussion on Isotopes. *Proceedings of the Royal Society of London Series A, Containing Papers of a Mathematical and Physical Character*. 1921;99(697):87-104.
44. Yarbrow O, Mailen J, Groenier W. Iodine scrubbing from off-gas with concentrated nitric acid. Technical Report., Oak Ridge National Lab., Tenn.(USA). 1974.
45. Burger LL, Scheele RD. Status of radioiodine control for nuclear fuel reprocessing plants. Technical Report., Pacific Northwest Lab., Richland, WA (USA). 1983.
46. Stromatt RW. Removal of Radio-Iodine from Purex Off-Gas with Nitric Acid and with

- Nitric Acid-Mercuric Nitrate Solutions. Technical Report No. NSA-18-031654. United States. 1958.
47. Trevorrow LE, Vandegrift GF, Kolba VM, Steindler MJ. Compatibility of technologies with regulations in the waste management of H-3, I-129, C-14, and Kr-85. Part I. Initial information base. Technical Report No. ANL-83-57-Pt.1. United States. 1983.
 48. Collins ED, Benker DE. Iodex process tests in a transuranium element production campaign. Technical Report No. ORNL/TM-6182. Oak Ridge National Lab. 1979.
 49. Holladay DW. Literature survey: methods for the removal of iodine species from off-gases and liquid waste streams of nuclear power and nuclear fuel reprocessing plants, with emphasis on solid sorbents. Technical Report No. ORNL/TM--6350. Oak Ridge National Lab. 1979.
 50. Mailen JC, Horner DE. Removal of Radioiodine from Gas Streams by Electrolytic Scrubbing. *Nuclear Technology*. 1976;30(3):317-324.
 51. Jubin RT, Strachan DM, Soelberg NR. Iodine Pathways and Off-Gas Stream Characteristics for Aqueous Reprocessing Plants – A Literature Survey and Assessment. Technical Report Idaho National Laboratory (INL), ID. 2013.
 52. Herrmann FJ, Motoi V, Fies H, Stojanik B, Furrer J, Kaempffer R. Testing an iodine filter for the vessel off-gas of the German industrial-scale reprocessing plant. Technical Report No. NUREG/CP--0098-VOL.1. 1989.
 53. Scott SM, Hu T, Yao T, Xin G, Lian J. Graphene-based sorbents for iodine-129 capture

- and sequestration. *Carbon*. 2015;90:1-8.
54. Han S, Um W, Kim W-S. Development of bismuth-functionalized graphene oxide to remove radioactive iodine. *Dalton Transactions*. 2019;48(2):478-485.
 55. Liu B, Ren X, Chen L, et al. High efficient adsorption and storage of iodine on S, N co-doped graphene aerogel. *Journal of Hazardous Materials*. 2019;373:705-715.
 56. Kim H, Renault O, Tyurnina A, et al. Doping efficiency of single and randomly stacked bilayer graphene by iodine adsorption. *Applied Physics Letters*. 2014;105(1):011605.
 57. Juhola AJ. Iodine adsorption and structure of activated carbons. *Carbon*. 1975;13(5):437-442.
 58. Zhou J, Hao S, Gao L, Zhang Y. Study on adsorption performance of coal based activated carbon to radioactive iodine and stable iodine. *Annals of Nuclear Energy*. 2014;72:237-241.
 59. Riley BJ, Chun J, Ryan JV, et al. Chalcogen-based aerogels as a multifunctional platform for remediation of radioactive iodine. *Rsc Advances*. 2011;1(9):1704-1715.
 60. Riley BJ, Pierce DA, Lepry WC, et al. Consolidation of Tin Sulfide Chalcogels and Xerogels with and without Adsorbed Iodine. *Industrial & Engineering Chemistry Research*. 2015;54(45):11259-11267.
 61. Subrahmanyam KS, Sarma D, Malliakas CD, et al. Chalcogenide Aerogels as Sorbents for Radioactive Iodine. *Chemistry of Materials*. 2015;27(7):2619-2626.
 62. Subrahmanyam KS, Malliakas CD, Sarma D, Armatas GS, Wu J, Kanatzidis MG. Ion-

- Exchangeable Molybdenum Sulfide Porous Chalcoel: Gas Adsorption and Capture of Iodine and Mercury. *Journal of the American Chemical Society*. 2015;137(43):13943-13948.
63. Matyáš J, Canfield N, Sulaiman S, Zumhoff M. Silica-based waste form for immobilization of iodine from reprocessing plant off-gas streams. *Journal of Nuclear Materials*. 2016;476:255-261.
64. Matyáš J, Fryxell G, Busche B, Wallace K, Fifield L. Functionalised silica aerogels: Advanced materials to capture and immobilise radioactive iodine. Paper presented at: Ceramic Engineering and Science Proceedings. 2011
65. Matyáš J, Ilton ES, Kovařík L. Silver-functionalized silica aerogel: towards an understanding of aging on iodine sorption performance. *RSC advances*. 2018;8(56):31843-31852.
66. Jubin RT. Organic iodine removal from simulated dissolver off-gas systems utilizing silver-exchanged mordenite. Technical Report No. CONF-811108--14. Oak Ridge National Lab. 1981.
67. Jubin RT. Organic iodine removal from simulated dissolver off-gas streams using partially exchanged silver mordenite. Paper presented at: 17. DOE nuclear air cleaning conference. 1982-01-01, 1982; Denver, CO, USA,
68. Scheele RD, Burger LL, Matsuzaki CL. Methyl iodide sorption by reduced silver mordenite. Technical Report No. PNNL-4489. Pacific Northwest National Laboratory.

- 1983.
69. Tanabe H, Sakuragi T, Yamaguchi K, Sato T, Owada H. Development of new waste forms to immobilize iodine-129 released from a spent fuel reprocessing plant. *Advances in Science and Technology*. 2010;73:158-170.
 70. Funabashi K, Fukasawa T, Kikuchi M. Investigation of Silver-Impregnated Alumina for Removal of Radioactive Methyl Iodide. *Nuclear Technology*. 1995;109(3):366-372.
 71. Azambre B, Chebbi M, Hijazi A. Effects of the cation and Si/Al ratio on CH₃I adsorption by faujasite zeolites. *Chemical Engineering Journal*. 2020;379:122308.
 72. Chebbi M, Azambre B, Monsanglant-Louvet C, Marcillaud B, Roynette A, Cantrel L. Effects of water vapour and temperature on the retention of radiotoxic CH₃I by silver faujasite zeolites. *Journal of Hazardous Materials*. 2021;409:124947.
 73. Chebbi M, Azambre B, Cantrel L, Koch A. A Combined DRIFTS and DR-UV-Vis Spectroscopic In Situ Study on the Trapping of CH₃I by Silver-Exchanged Faujasite Zeolite. *The Journal of Physical Chemistry C*. 2016;120(33):18694-18706.
 74. Chebbi M, Chibani S, Paul J-F, Cantrel L, Badawi M. Evaluation of volatile iodine trapping in presence of contaminants: A periodic DFT study on cation exchanged-faujasite. *Microporous and Mesoporous Materials*. 2017;239:111-122.
 75. Thomas TR, Staples BA, Murphy LP. Development of Ag⁰Z for bulk ¹²⁹I removal from nuclear fuel reprocessing plants and PbX for ¹²⁹I storage. Paper presented at: 15. nuclear air cleaning conference. 1978-01-01, 1978; Boston, MA, USA

76. Chee T-S, Tian Z, Zhang X, Lei L, Xiao C. Efficient capture of radioactive iodine by a new bismuth-decorated electrospinning carbon nanofiber. *Journal of Nuclear Materials*. 2020;542:152526.
77. Zou H, Yi F, Song M, et al. Novel synthesis of Bi-Bi₂O₃-TiO₂-C composite for capturing iodine-129 in off-gas. *Journal of Hazardous Materials*. 2019;365:81-87.
78. Al-Mamoori A, Alsalbokh M, Lawson S, Rownaghi AA, Rezaei F. Development of bismuth-mordenite adsorbents for iodine capture from off-gas streams. *Chemical Engineering Journal*. 2020;391:123583.
79. Falaise C, Volkringer C, Facqueur J, Bousquet T, Gasnot L, Loiseau T. Capture of iodine in highly stable metal–organic frameworks: a systematic study. *Chemical Communications*. 2013;49(87):10320-10322.
80. He L, Chen L, Dong X, et al. A nitrogen-rich covalent organic framework for simultaneous dynamic capture of iodine and methyl iodide. *Chem*. 2020.
81. Sava DF, Chapman KW, Rodriguez MA, et al. Competitive I₂ Sorption by Cu-BTC from Humid Gas Streams. *Chemistry of Materials*. 2013;25(13):2591-2596.
82. Sava DF, Garino TJ, Nenoff TM. Iodine Confinement into Metal–Organic Frameworks (MOFs): Low-Temperature Sintering Glasses To Form Novel Glass Composite Material (GCM) Alternative Waste Forms. *Industrial & Engineering Chemistry Research*. 2012;51(2):614-620.
83. Riley BJ, Vienna JD, Strachan DM, McCloy JS, Jerden JL. Materials and processes for

- the effective capture and immobilization of radioiodine: A review. *Journal of Nuclear Materials*. 2016;470:307-326.
84. Jordan JA. *Investigation of Silver Nitrate–Impregnated Alumina as an Alternative Iodine Sorbent*, The University of Tennessee, Knoxville; 2018.
 85. Wiechert AI, Ladshaw AP, Moon J, et al. Capture of Iodine from Nuclear-Fuel-Repurposing Off-Gas: Influence of Aging on a Reduced Silver Mordenite Adsorbent after Exposure to NO/NO₂. *ACS Applied Materials & Interfaces*. 2020.
 86. Patton KK, Bruffey SH, Walker JF, Jubin RT. NO₂ Aging and Iodine Loading of Silver-Functionalized Aerogels. Technical Report No. ORNL/LTR-2014/271. Oak Ridge National Lab (ORNL), Oak Ridge, TN. 2014.
 87. Bruffey SH, Jordan JA, Jubin RT. Iodine Adsorption by Ag-Aerogel under Prototypical Vessel Off-Gas Conditions. Technical Report No. ORNL/TM-2016-417. Oak Ridge National Laboratory (ORNL), Oak Ridge, TN. 2016.
 88. Jordan JA, Bruffey SH. Preparation of NO₂-Aged Silver-Functionalized Silica-Aerogel and Silver Mordenite Samples. Technical Report No. FCRD-MRWFD-2016-000358. Oak Ridge National Laboratory (ORNL): Oak Ridge, TN United States. 2016.
 89. Soelberg N, Watson T. Phase 1 Methyl Iodide Deep-Bed Adsorption Tests. Technical Report No. INL/EXT-14-32917. Idaho National Laboratory, Idaho Falls, ID. 2014.
 90. Soelberg NR, Watson TL. FY-2015 Methyl Iodide Deep-Bed Adsorption Test Report. Technical Report No. INL/EXT-15-36817. Idaho National Laboratory, Idaho Falls, ID.

- 2015.
91. Soelberg NR, Watson TL. FY-2016 Methyl Iodide Higher NO_x Adsorption Test Report. Technical Report No. INL/EXT-16-40087. Idaho National Laboratory, Idaho Falls, ID. 2016.
92. Jubin RT. *The mass transfer dynamics of gaseous methyl-iodide adsorption by silver-exchanged sodium mordenite* [Dissertation]. Knoxville, The University of Tennessee; 1994.
93. Choi S, Nan Y, Tavlarides LL. Kinetics of aging process on reduced Ag exchanged mordenite in dry air and humid air. *AIChE Journal*. 2021:e17182.
94. Jubin RT. Airborne waste management technology applicable for use in reprocessing plants for control of iodine and other off-gas constituents. Technical Report No. ORNL/TM-10477. Oak Ridge National Lab., TN (USA). 1988.
95. Nan Y, Tavlarides LL, DePaoli DW. Adsorption of iodine on hydrogen-reduced silver-exchanged mordenite: Experiments and modeling. *AIChE Journal*. 2017;63(3):1024-1035.
96. Soelberg N, Watson T. Deep Bed Iodine Sorbent Testing FY 2011 Report. Technical Report No. INL/EXT-11-23191. United States. 2011.
97. Soelberg N, Watson T. Iodine Sorbent Performance in FY 2012 Deep Bed Tests. Technical Report No. INL/EXT-12-27075. Idaho National Laboratory, Idaho Falls, ID. 2012.

98. Bruffey SH, Jubin RT, Anderson KK, Walker Jr JF. Aging and Iodine Loading of Silver-Functionalized Aerogels. 2013-01-01, 2013
99. Bruffey SH, Jubin RT. Iodine Capture and Mechanical Stability of Modified Silver-Functionalized Silica Aerogel. Technical Report No. ORNL/SPR-2019/1206. Oak Ridge National Lab.(ORNL), Oak Ridge, TN. 2019.
100. Jubin RT, Bruffey SH, Jordan JA. Performance of Silver-Exchanged Mordenite and Silver-Functionalized Silica-Aerogel Under Vessel Off-gas Conditions. Technical Report No. ORNL/SR-2017/477. Oak Ridge National Lab (ORNL), Oak Ridge, TN. 2017.
101. Soelberg N, Watson T. Deep Bed Adsorption Testing using Silver-Functionalized Aerogel. Technical Report No. INL/EXT-12-26522. Idaho National Laboratory, Idaho Falls, ID. 2012.
102. Chen P, He X, Pang M, Dong X, Zhao S, Zhang W. Iodine Capture Using Zr-Based Metal–Organic Frameworks (Zr-MOFs): Adsorption Performance and Mechanism. *ACS Applied Materials & Interfaces*. 2020;12(18):20429-20439.
103. Li Z-J, Yue Z, Ju Y, et al. Ultrastable Thorium Metal–Organic Frameworks for Efficient Iodine Adsorption. *Inorganic Chemistry*. 2020;59(7):4435-4442.
104. Banerjee D, Chen X, Lobanov SS, et al. Iodine Adsorption in Metal Organic Frameworks in the Presence of Humidity. *ACS Applied Materials & Interfaces*. 2018;10(13):10622-10626.
105. Choi S, Nan Y, Wiechert A, et al. Aging Kinetics of Ag-Exchanged Mordenite and Ag-

Functionalized Silica Aerogel in the Presence of Off-Gas Streams. Paper presented at:
2019 AIChE Annual Meeting, 2019

106. Wiechert A. *Adsorption Processes in Nuclear Fuel Resource Recovery* [Dissertation], Georgia Institute of Technology; 2020.
107. National Institute for Occupational Safety and Health (NIOSH). 1988 OSHA PEL Project Documentation, METHYL IODIDE. In:1989.
108. Buckell M. The toxicity of methyl iodide: I. Preliminary survey. *Br J Ind Med*. 1950;7(3):122-124.
109. Hallier E, Deutschmann S, Reichel C, Bolt HM, Peter H. A comparative investigation of the metabolism of methyl bromide and methyl iodide in human erythrocytes. *International Archives of Occupational and Environmental Health*. 1990;62(3):221-225.
110. Reed CJ, Gaskell BA, Banger KK, Lock EA. Olfactory toxicity of methyl iodide in the rat. *Archives of Toxicology*. 1995;70(1):51-56.
111. Chamberlain MP, Lock EA, Reed CJ. Investigations of the pathways of toxicity of methyl iodide in the rat nasal cavity. *Toxicology*. 1998;129(2):169-181.
112. Gandy J, Millner GC, Bates HK, Casciano DA, Harbison RD. Effects of selected chemicals on the glutathione status in the male reproductive system of rats. *Journal of Toxicology and Environmental Health*. 1990;29(1):45-57.
113. EPA. Methyl Iodide, Distributed Structure-Searchable Toxicity (DSSTox) Database. In. <https://www.epa.gov/chemical-research/distributed-structure-searchable-toxicity-dsstox->

- [database](#): EPA.
114. EPA. Propane, iodo-, Distributed Structure-Searchable Toxicity (DSSTox) Database. In. <https://www.epa.gov/chemical-research/distributed-structure-searchable-toxicity-dsstox-database>: EPA.
115. EPA. 1-Iodohexane, Distributed Structure-Searchable Toxicity (DSSTox) Database. In. <https://www.epa.gov/chemical-research/distributed-structure-searchable-toxicity-dsstox-database>: EPA.
116. EPA. Octane, 1-iodo-, Distributed Structure-Searchable Toxicity (DSSTox) Database. In. <https://www.epa.gov/chemical-research/distributed-structure-searchable-toxicity-dsstox-database>: EPA.
117. EPA. 1-Iodododecane, Distributed Structure-Searchable Toxicity (DSSTox) Database. In. <https://www.epa.gov/chemical-research/distributed-structure-searchable-toxicity-dsstox-database>: EPA.
118. Strachan DM, Chun J, Matyas J, et al. Summary Report on the Volatile Radionuclide and Immobilization Research for FY2011 at PNNL. Technical Report No. PNNL-20807. Pacific Northwest National Laboratory. 2011.
119. Jordan JA, Jubin RT. Stability of Tritium and Iodine Sorbents under Tritium-Pretreatment Off-Gas Conditions. Technical Report No. ORNL/SR-2017/162. Oak Ridge National Lab (ORNL), Oak Ridge, TN. 2017.
120. Brunauer S, Emmett PH, Teller E. Adsorption of gases in multimolecular layers. *Journal*

- of the American chemical society*. 1938;60(2):309-319.
121. Harkins WD, Jura G. Surfaces of solids. XIII. A vapor adsorption method for the determination of the area of a solid without the assumption of a molecular area, and the areas occupied by nitrogen and other molecules on the surface of a solid. *Journal of the American Chemical Society*. 1944;66(8):1366-1373.
 122. Barrett EP, Joyner LG, Halenda PP. The determination of pore volume and area distributions in porous substances. I. Computations from nitrogen isotherms. *Journal of the American Chemical society*. 1951;73(1):373-380.
 123. Lastoskie C, Gubbins KE, Quirke N. Pore size distribution analysis of microporous carbons: a density functional theory approach. *The journal of physical chemistry*. 1993;97(18):4786-4796.
 124. Lin R, Liu J, Nan Y, DePaoli DW, Tavlarides LL. Kinetics of Water Vapor Adsorption on Single-Layer Molecular Sieve 3A: Experiments and Modeling. *Industrial & Engineering Chemistry Research*. 2014;53(41):16015-16024.
 125. Nan Y, Liu J, Tang S, Lin R, Tavlarides LL. Silver-Exchanged Mordenite for Capture of Water Vapor in Off-Gas Streams: A Study of Adsorption Kinetics. *Industrial & Engineering Chemistry Research*. 2018;57(3):1048-1058.
 126. Yagi S, Kunii D. Studies on combustion of carbon particles in flames and fluidized beds. *Symposium (International) on Combustion*. 1955;5(1):231-244.
 127. Levenspiel O. *Chemical Reaction Engineering*. New York: John Wiley & Sons. 1972.

128. Ranz WE, Marshall WR. Evaporation from drops. *Chem eng prog.* 1952;48(3):141-146.
129. Fuller EN, Ensley K, Giddings JC. Diffusion of halogenated hydrocarbons in helium. The effect of structure on collision cross sections. *The Journal of Physical Chemistry.* 1969;73(11):3679-3685.
130. Fuller EN, Giddings JC. A Comparison of Methods for Predicting Gaseous Diffusion Coefficients. *Journal of Chromatographic Science.* 1965;3(7):222-227.
131. Fuller EN, Schettler PD, Giddings JC. A New Method for Prediction of Binary Gas-Phase Diffusion Coefficients. *Industrial & Engineering Chemistry.* 1966;58(5):18-27.
132. Matsunaga N, Hori M, Nagashima A. Gaseous diffusion coefficients of methyl bromide and methyl iodide into air, nitrogen, and oxygen. *Heat Transfer-Asian Research.* 2009;38(6):361-369.
133. Ramachandran PA, Doraiswamy LK. Modeling of noncatalytic gas-solid reactions. *AIChE Journal.* 1982;28(6):881-900.
134. Ramachandran PA, Kulkarni BD. Approximate analytical solution to Gas-Solid noncatalytic reaction problems. *Industrial & Engineering Chemistry Process Design and Development.* 1980;19(4):717-719.
135. Glueckauf E, Coates JI. Theory of chromatography. Part IV. The influence of incomplete equilibrium on the front boundary of chromatograms and on the effectiveness of separation. *Journal of the Chemical Society.* 1947:1315-1321.
136. Ruthven DM. *Principles of adsorption and adsorption processes.* John Wiley & Sons.

- 1984.
137. Ruckenstein E, Vaidyanathan AS, Youngquist GR. Sorption by solids with bidisperse pore structures. *Chemical Engineering Science*. 1971;26(9):1305-1318.
138. Jenks CJ, Bent BE, Bernstein N, Zaera F. The Chemistry of Alkyl Iodides on Copper Surfaces. 1. Adsorption Geometry. *The Journal of Physical Chemistry B*. 2000;104(14):3008-3016.
139. Zhou XL, Solymosi F, Blass PM, Cannon KC, White JM. Interactions of methyl halides (Cl, Br and I) with Ag(111). *Surface Science*. 1989;219(1):294-316.
140. Tjandra S, Zaera F. Thermal Reactions of Alkyl Iodides on Ni (100) Single Crystal Surfaces. *Journal of the American Chemical Society*. 1995;117(38):9749-9755.
141. Yamauchi N, Miyoshi A, Kosaka K, Koshi M, Matsui H. Thermal Decomposition and Isomerization Processes of Alkyl Radicals. *The Journal of Physical Chemistry A*. 1999;103(15):2723-2733.
142. Bartsch RA, Pruss GM. Metal ion promoted dehydrohalogenation of secondary alkyl halides. *The Journal of Organic Chemistry*. 1972;37(3):458-462.
143. Zaera F, Tjandra S, Janssens TVW. Selectivity among Dehydrogenation Steps for Alkyl Groups on Metal Surfaces: Comparison between Nickel and Platinum. *Langmuir*. 1998;14(6):1320-1327.
144. Arrhenius S. Über die Dissociationswärme und den Einfluss der Temperatur auf den Dissociationsgrad der Elektrolyte. *Zeitschrift für physikalische Chemie*. 1889;4(1):96-

- 116.
145. Zhou XL, White JM. Thermal decomposition of C₂H₅I on Ag(111). *Catalysis Letters*. 1989;2(6):375-384.
146. Robb DA, Harriott P. The kinetics of methanol oxidation on a supported silver catalyst. *Journal of Catalysis*. 1974;35(2):176-183.
147. Fogler HS. *Elements of chemical reaction engineering*. Prentice Hall. 2016.
148. Tang S, Choi S, Nan Y, Tavlarides LL. Adsorption of Methyl Iodide on Reduced Silver-Functionalized Silica Aerogel: Kinetics and Modeling. *AIChE Journal*. 2020:e17137.
149. Matyáš J, Engler RK. Assessment of Methods to Consolidate Iodine-Loaded Silver-Functionalized Silica Aerogel. Technical Report No. PNNL-22874, AF5805000. Pacific Northwest National Lab. (PNNL), Richland, WA. 2013.
150. Talu O, Sun MS, Shah DB. Diffusivities of n-alkanes in silicalite by steady-state single-crystal membrane technique. *AIChE Journal*. 1998;44(3):681-694.
151. Soares JL, Moreira RFPM, José HJ, Grande CA, Rodrigues AE. Hydrotalcite Materials for Carbon Dioxide Adsorption at High Temperatures: Characterization and Diffusivity Measurements. *Separation Science and Technology*. 2005;39(9):1989-2010.
152. Balkis Ameen K, Rajasekar K, Rajasekharan T. Silver Nanoparticles in Mesoporous Aerogel Exhibiting Selective Catalytic Oxidation of Benzene in CO₂ Free Air. *Catalysis Letters*. 2007;119(3):289-295.
153. Currie JA. Gaseous diffusion in porous media. Part 3 - Wet granular materials. *British*

- Journal of Applied Physics*. 1961;12(6):275-281.
154. Park S, An H, Park MB, Lee J. Adsorption behavior of methyl iodide on a silver ion-exchanged ZSM-5. *Microporous and Mesoporous Materials*. 2020;294:109842.
 155. Lente G, Fábián I, Poë AJ. A common misconception about the Eyring equation. *New Journal of Chemistry*. 2005;29(6):759-760.
 156. Lesclaux R, Khê PV, Dezaudier P, Soullignac JC. Flash photolysis studies of the reaction of NH₂ radicals with NO. *Chemical Physics Letters*. 1975;35(4):493-497.
 157. Benson SW, Dobis O. Existence of Negative Activation Energies in Simple Bimolecular Metathesis Reactions and Some Observations on Too-Fast Reactions. *The Journal of Physical Chemistry A*. 1998;102(27):5175-5181.
 158. Kindel O, Hoeflich V, Herrmann FJ, Patzelt P. Removal of iodoorganic compounds from kerosene in nuclear fuel reprocessing. *Journal of Radioanalytical and Nuclear Chemistry*. 1993;176(3):251-259.
 159. Zhang W, Zhang L, Hui Z, Zhang X, Qian Y. Synthesis of nanocrystalline Ag₂S in aqueous solution. *Solid State Ionics*. 2000;130(1):111-114.
 160. Hota G, Idage SB, Khilar KC. Characterization of nano-sized CdS–Ag₂S core-shell nanoparticles using XPS technique. *Colloids and Surfaces A: Physicochemical and Engineering Aspects*. 2007;293(1):5-12.
 161. Tomaszewicz E, Kurzawa M. Use of XPS method in determination of chemical environment and oxidation state of sulfur and silver atoms in Ag₆S₃O₄ and Ag₈S₄O₄

- compounds. *Journal of materials science*. 2004;39(6):2183-2185.
162. Wolan JT, Hoflund GB. Surface characterization study of AgF and AgF₂ powders using XPS and ISS. *Applied Surface Science*. 1998;125(3):251-258.
163. Schön G, Tummavuori J, Lindström B, Enzell CR, Swahn CG. ESCA studies of Ag, Ag₂O and AgO. *Acta Chem Scand*. 1973;27(7):2623.
164. Hoflund GB, Weaver JF, Epling WS. Ag₂O XPS Spectra. *Surface Science Spectra*. 1994;3(2):157-162.
165. Briggs D, Seah MP. *Practical surface analysis: by Auger and X-ray photoelectron spectroscopy*. Wiley. 1983.
166. Morent R, De Geyter N, Leys C, Gengembre L, Payen E. Comparison between XPS- and FTIR-analysis of plasma-treated polypropylene film surfaces. *Surface and Interface Analysis*. 2008;40(3-4):597-600.
167. Onoue F, Tsuji K. X-Ray Elemental Imaging in Depth by Combination of FE-SEM-EDS and Glow Discharge Sputtering. *ISIJ International*. 2013;53(11):1939-1942.
168. Ma S, Lan Y, Perez GMJ, Moniri S, Kenis PJA. Silver Supported on Titania as an Active Catalyst for Electrochemical Carbon Dioxide Reduction. *ChemSusChem*. 2014;7(3):866-874.
169. Ishida T, Kikuchi S, Tsubo T, Yamada T. Silver-Catalyzed Incorporation of Carbon Dioxide into o-Alkynylaniline Derivatives. *Organic Letters*. 2013;15(4):848-851.
170. Dey S, Dhal GC. Applications of silver nanocatalysts for low-temperature oxidation of

- carbon monoxide. *Inorganic Chemistry Communications*. 2019;110:107614.
171. Ma M, Trzeźniewski BJ, Xie J, Smith WA. Selective and efficient reduction of carbon dioxide to carbon monoxide on oxide-derived nanostructured silver electrocatalysts. *Angewandte Chemie*. 2016;128(33):9900-9904.
172. Backx C, De Groot CPM, Biloen P, Sachtler WMH. Interaction of O₂, CO₂, CO, C₂H₄ and C₂H₄O with Ag(110). *Surface Science*. 1983;128(2):81-103.
173. Campbell CT, Paffett MT. The interactions of O₂, CO and CO₂ with Ag(110). *Surface Science*. 1984;143(2):517-535.
174. Langmuir I. The adsorption of gases on plane surfaces of glass, mica and platinum. *Journal of the American Chemical Society*. 1918;40(9):1361-1403.
175. Murzin DY. On Langmuir kinetics and zero order reactions. *Catalysis Communications*. 2008;9(9):1815-1816.
176. Yang RT. *Gas separation by adsorption processes*. Vol 1: World Scientific. 1997.
177. Ribeiro AM, Neto P, Pinho C. Mean porosity and pressure drop measurements in packed beds of monosized spheres: side wall effects. *International Review of Chemical Engineering*. 2010;2(1):40-46.
178. Zou RP, Yu AB. The packing of spheres in a cylindrical container: the thickness effect. *Chemical engineering science*. 1995;50(9):1504-1507.
179. Asmussen RM, Matyáš J, Qafoku NP, Kruger AA. Silver-functionalized silica aerogels and their application in the removal of iodine from aqueous environments. *Journal of*

- Hazardous Materials*. 2019;379:119364.
180. Selker ML. Reaction of Methyl Iodide with Sulfur Compounds. *Industrial & Engineering Chemistry*. 1948;40(8):1467-1470.
181. Markuszewski R, Wei CK, Wheelock TD. Oxydesulfurization of coal treated with methyl iodide—Implications for removal of organic sulfur. *Am Chem Soc Div FuelChem Prepr*. 1980;25(2):187-194.

Vita

NAME OF AUTHOR: Siqu Tang

PLACE OF BIRTH: Xiaogan, Hubei, China

UNDERGRADUATE SCHOOLS ATTENDED:

Bachelor of Science, 2018

Department of Biomedical and Chemical Engineering, Syracuse University

Syracuse, NY, USA

PROFESSIONAL EXPERIENCE:

Department of Biomedical and Chemical Engineering, Syracuse University

Teaching Assistant, 2018 – 2020

Research Assistant, 2020 – present